Modeling Nearshore Processes

by

Wenkai Qin and Ib A. Svendsen

RESEARCH REPORT NO. CACR-03-04
December, 2003

Center for Applied Coastal Research
Ocean Engineering Laboratory
University of Delaware
Newark, DE 19716

ACKNOWLEDGEMENTS

This work was sponsored by the Army Research Office under Grant No. DAAD19-00-1-0467 and by the Large-Scale Laboratory Investigation of Longshore Sediment Transport work unit of the U.S. Army Corps of Engineers (USACE), General Investigation Research and Development Program.

Mr. Bruce Ebersole, Ernest Smith, David Hamilton and William Hilford at the U .S. Army Engineering Research and Development Center are gratefully acknowledged for providing the LSTF data and constructive guidance for the modeling work.

TABLE OF CONTENTS

LIST OF FIGURES

LIST OF TABLES

ABSTRACT

This study is to investigate the nearshore processes involving wave transformations, wave-driven circulation, as well as the resulting sediment transport and beach evolution through numerical modeling. A nearshore sediment transport model and kinematic wave models were developed and incorporated with the SHORECIRC (SC) model. The coupled wave-current-sediment transport model was tested against comprehensive experimental data measured in the LSTF at the CHL and in other facilities. The comparisons indicate that the model is capable of well predicting nearshore wave properties, wave-induced hydrodynamics and sediment transport under both regular and irregular wave conditions.

The predicted wave properties and wave-induced hydrodynamics using the cnoidal-bore wave model that was developed in this study using non-sinusoidal wave phase motions, coupled with the SC show excellent agreement with measured data in the experiments with regular waves. The sinusoidal wave model, however, underpredicts the wave height increase towards breaking and the decay inside the surfzone, and it is incapable of predicting the increases in the wave peakedness (η_c/H) and in c^2/gh towards breaking and the decays afterwards. Consequently, the sinusoidal wave model over-estimates the wave volume flux but reasonably well predicts the radiation stress. Thus the SC with the sinusoidal wave model as driver over-estimates the undertow but well predicts the longshore currents and mean water level. Both the measurement and the model prediction demonstrate less significant cross-shore variations of wave properties and wave-induced currents under irregular waves. The

predicted wave-group averaged quantities and temporal variations of wave properties and wave-induced circulation using the irregular wave model coupled with the SC agree reasonably well with the experiment measurements under irregular waves in the LSTF.

The sediment transport model was developed to calculate the transport rates of bedload and suspended load as well as the resulting beach morphology change. The formula for the bedload transport rate was derived starting from the two-phase flow theory and appears to be an improved version of both the Bailard and Inman (1981a) formula and the Engelund and Fredsøe (1976) formula. Two approaches have been developed for suspended sediment transport: One is a modification of the Bailard (1981b) formula to include the effect of wave breaking, and the other is a detailed physics-based phase-resolving diffusion-convection model for sediment suspension.

The wave-current-sediment transport model was used to simulate the sediment transport on a plane beach under regular waves. The differences in the predicted sediment transport rates among different formulas were demonstrated, the effects of the wave phase motion, wave asymmetry, wave breaking, currents, sediment convection caused by the vertical flow velocity as well as bottom boundary conditions on sediment transport were investigated, and the resulting beach morphology changes such as formation of the breaker bar as well as the general beach erosion in the inner and middle surfzone were illustrated.

The wave-current-sediment transport model was tested against the measurements in a comprehensive hydrodynamic and sediment transport experiment under irregular wave environments in the LSTF. In addition to wave heights and wave-induced circulation, the predicted longshore sediment transport rates, vertical profiles of sediment concentrations and fluxes as well as the beach profiles show good agreement with experiment measurements.

Chapter 1

INTRODUCTION

The nearshore ocean, extending from the beach to water depths of about 10 meters, is of significant societal, economic and military importance. More than half the U.S. population lives within 50 miles of the shoreline. Beaches are a primary recreational destination for tourists, and are essential to commerce and national defense. It is crucial to increase our knowledge of nearshore processes resulting from the interactions among winds, waves, currents, tides, sediments and other phenomena in the nearshore region. Better understanding and accurate prediction of nearshore processes can improve coastal management and lead to substantial benefit for coastal communities.

The analysis and modeling of nearshore processes has been under continuing development over several decades and particularly during the last few years. The present study presents an effort to advance our knowledge about nearshore processes by using numerical modeling together with the large-scale laboratory experiments.

1.1 Observations of Nearshore Processes

An effective strategy for investigating nearshore processes is to combine numerical models with laboratory or field experiments. Observations are not only needed to reveal new and unexpected phenomena but also needed to test model predictions. Several comprehensive field investigations as well as numerous laboratory experiments have been performed mainly in the USA and Europe. Field experiments can be performed at a large geometric scale and under natural nearshore conditions,

but they are hard to control and significant uncertainties are still present in the data collected. Laboratory experiments, on the other hand, are relatively easier to control but are usually limited by the small geometric scale and the incapability of reproducing the complex nearshore processes observed in the field.

As one of the few large-scale facilities around the world, the Large-scale Sediment Transport Facility (LSTF) has been constructed at the U.S. Army Engineering Research and Development Center's (ERDC) Coastal and Hydraulics Laboratory (CHL), Vicksburg, Mississippi (Hamilton *et al.*, 2001; Hamilton and Ebersole, 2001). The intent for this facility is to accurately reproduce certain nearshore processes found on a long, straight, natural beach in a finite-length wave basin. The LSTF simulates nearshore hydrodynamics and sediment transport processes under both regular and irregular wave environments at a relatively large geometric scale.

Several hydrodynamic and sediment transport experiments have been performed in the LSTF, and comprehensive data sets including wave properties, wave-induced circulation and resulting sediment transport and beach profile evolution have been collected. These data were analyzed and used to test the coupled wave-current-sediment transport model developed in this study.

1.2 Review of Modeling Nearshore Wave and Circulation

Nearshore wave motion and circulation have been extensively studied since large-scale computations became possible, increasing from a modest beginning in the early 1970. Hence a rich literature is available on this subject. It is beyond the scope of the present study to give a complete review of this literature. Interested readers are referred to review papers such as Battjes (1988) or Svendsen and Putrevu (1995). In the following we limit the description to aspects relevant for the present study.

Comprehensive nearshore circulation models consist of two major components. The first is a model component that describes the wave motion and is also

capable of providing information about the wave averaged properties responsible for driving currents, which is the radiation stresses and the volume fluxes generated by waves. The second is a circulation part that calculates the currents from the wave-generated forcing. The wave component is also termed the **wave driver** for the circulation component. Both components have been subject to intensive studies in recent years and advanced versions have been developed by commercial institutions such as Danish Hydraulics Institute, Delft Hydraulics, and Hydraulics Research, Wallingford, UK to mention some. These models, however, are all proprietary and the source codes cannot be purchased. In the present investigation we use the quasi 3-D SHORECIRC model for the circulation part of the model computations. For a closer description see e.g. Van Dongeren and Svendsen (2000). This model has been tested extensively in the past, as e.g., Svendsen et al. (1997), Van Dongeren and Svendsen (2000), and Haas and Svendsen (2000).

An important aspect of the wave models used as drivers is that they need to be fast enough to avoid slowing down the computational performance of the entire model. The wave drivers are relatively simple wave models and several suitable models have been published and studied. The REF/DIF1 model developed by Kirby and Dalrymple (1994) has these capabilities, and has been used in all previous applications of the SC model (Dongeren *et al.* (1994), Haas and Svendsen (2000), Haas *et al.* (2000), Svendsen *et al.* (1997), Van Dongeren and Svendsen (2000), to mention some).

The wave model is also essential to modeling nearshore sediment transport and beach evolution. The wave motion is the source mechanism for sediment transport in the nearshore. It is not only because the nearshore current, a primary agent responsible for net sediment transport, is induced by waves, but also because the wave velocity combined with the current velocity is responsible for sediment entrainment from the bed and for sediment suspension in the water column. In addition, the

non-sinusoidal wave phase motion or wave asymmetry (skewness) tends to induce net sediment transport in the wave direction, which is important for the cross-shore sediment transport and resulting beach profile evolution.

REF/DIF1 uses the sinusoidal wave theory for the wave phase motion and assumes steady-state wave transformation. However, in reality waves are usually irregular and become non-sinusoidal in shape as they propagate into the nearshore region. Hence, REF/DIF1 may not be able to provide accurate forcing for wave-induced circulation or provide accurate wave velocities and phase motions which are essential for the nearshore sediment transport and beach evolution. Alternative wave models are developed in the present study. They include both the wave non-linearity and wave irregularity in the models but at the same time keep the model simplicity.

The wave models developed in this study are based on the kinematic wave theory which is quite effective for the wave propagation on the beaches with limited longshore variations considered here. In its general 2-D horizontal form the kinematic wave theory was first presented by Phillips (1969). This method remains popular and is attractive because of its relative simplicity. It essentially is capable of describing the wave transformation and refraction in areas with gently sloping topography. Phillips described the method for sinusoidal waves, but as illustrated in this study this approach is capable of describing slowly varying non-sinusoidal waves as well, if choosing appropriate theories for wave phase motions.

1.3 Review of Modeling Nearshore Sediment Transport

Numerous models have been proposed for coastal sediment transport, ranging from the simple CERC formula (USACE, 1984), quasi-steady models based on Bagnold's energetic principles to complex numerical models involving higher-order turbulence closure schemes or based on the two-phase flow theory. However, the

accurate prediction of coastal sediment transport still presents a major challenge to coastal researchers and progress has been relatively slower in this area.

Sediment transport is typically separated into the suspended load mode and the bedload mode, and different formulas or models are applied to each mode separately. Significant uncertainties are still present in quantitative modeling of sediment transport and resulting bed change, even for open channel flows. The mechanisms and parameterizations both for sediment entrainment from the bed and suspension in the water column remain poorly understood. The complex flow condition for combined wave and current flows make it more chanllenging to accurately predict the nearshore sediment transport and beach morphology change.

Sediment suspension and transport vary temporally and spatially in the nearshore region. Even the wave-averaged net sediment transport rates vary significantly not only in magnitudes but also in directions. A few numerical models for coastal sediment transport have been developed by commercial institutions such as Danish Hydraulics Institute, Delft Hydraulics, and Hydraulics Research, Wallingford, UK to mention some. Different assumptions were made in these models and the accuracy of the model predictions is still less satisfying (Davies *et al.*, 1997). A detailed physics-based model for coastal sediment transport and morphology change incorporated in a nearshore hydrodynamic model has not been developed in the United States, and this study is to present an effort in this area.

1.4 Motivation and Objectives

The purpose of this study is to investigate nearshore processes that involve transformation of surface gravity waves propagating across the continental shelf to the beach, the corresponding wave-induced circulation, and the resulting sediment transport and beach evolution by using numerical modeling and the large-scale laboratory experiments in the LSTF.

The main objectives of this study are to: (1) Incorporate a nearshore sediment transport model and wave models in the nearshore circulation model SHORECIRC and finally develop a realistic coupled wave-current-sediment transport model for nearshore processes that involve wave transformations, wave-driven circulation, and resulting sediment transport and beach evolution. (2) Compare the model predictions against the comprehensive experimental measurements carried out in the LSTF at the CHL. (3) Use the model to investigate some characteristics of nearshore hydrodynamics and sediment transport under both regular and irregular wave environments. And (4) illustrates the effects of different wave models on the predicted wave properties, wave-induced circulation and resulting sediment transport.

1.5 Outline of Present Work

The presentation is organized as follows.

Chapter 2 gives a brief overview of the LSTF facility layout, instrumentation, and the experiments performed in this facility. The data collected in the experiments include wave properties, 3-D wave-induced currents and sediment transport.

Chapter 3 discusses the theoretical background of the wave model developed based on the kinematic wave theory. After reviewing the basic equations for the general kinematic wave theory, the wave-averaged parameters used in the wave-averaged energy equation or used in the circulation model are formulated based on different theories for wave phase motions. This kinematic wave model is then further simplified for a parallel straight beach using the Snell's law. Analytical solutions are found for the parameters of regular waves propagating on the straight parallel beach and a numerical scheme is developed for the properties of irregular waves.

Chapter 4 presents extensive comparisons of wave properties and wave-induced circulation between the experimental measurements and model predictions. The comparisons include the entire range of nearshore parameters from wave heights, phase speeds, wave peakedness, mean water levels, to depth-averaged quantities

and depth variations of wave-induced currents. The comparisons against the regular wave experiments address the questions of how well a simple sinusoidal-wave based model perform in comparison to a model that better represents the actual wave phase motion and of how important the inaccuracies of a wave model are for reproducing the 3-D current patterns in the nearshore. The comparisons against the irregular wave experiment in the LSTF help illustrate the differences of wave characteristics and wave-induced currents between regular waves and irregular waves, and help test the performance of the kinematic model to represent the actual hydrodynamics induced by irregular waves.

Chapter 5 focuses on the theoretical background of the sediment transport and contains a detailed description of the sediment transport model developed in this study. A brief review of the two-phase flow theory is presented, followed by a re-derivation of the formula for the bedload transport rate starting from the two-phase flow theory. Two approaches are developed for suspend sediment transport. The simpler one is to modify the Bailard (1981b) formula to include the effect of wave breaking on suspended sediment transport rate. The other is to develop a detailed physics-based phase-resolving diffusion-convection model for sediment suspension. The boundary conditions and sediment diffusion coefficient are discussed in this chapter and are carefully implemented in the diffusion-convection model. A numerical scheme for solving the diffusion-convection equation is addressed.

Chapter 6 presents the simulation results of sediment transport using the coupled wave-current-sediment transport model for a presumed simple case, which is sediment transport on a plane beach under regular wave environments. The results were analyzed to test the behavior of the present models and to investigate the difference of various formulas in the predicted net transport rates, the contributions of waves and currents to sediment transport, and the effects of the wave asymmetry, convection due to the vertical flow velocity and different bottom boundary conditions

on sediment transport. The 3-D characteristics of nearshore sediment transport and the beach morphology change are also demonstrated.

Chapter 7 presents the comparisons of sediment transport under irregular wave environments between Test 1H in the LSTF and the predictions using the developed wave-current-sediment transport model. The comparisons include the time-averaged longshore sediment transport rates and the vertical profiles of the time-averaged sediment concentrations and fluxes.

Chapter 8 summarizes the work presented and provides the conclusions drawn from the study.

Chapter 2

OVERVIEW OF THE HYDRODYNAMIC AND SEDIMENT TRANSPORT EXPERIMENTS IN THE LSTF

The Large-scale Sediment Transport Facility (LSTF) was built at the U.S. Army Engineering Research and Development Center's (ERDC) Coastal and Hydraulics Laboratory (CHL), Vicksburg, Mississippi. The purpose for the facility is to reproduce certain nearshore processes found on a long, straight, natural beach in a finite-length wave basin. The LSTF is capable of simulating nearshore hydrodynamic and sediment transport at a relatively large geometric scale. A brief overview of the facility and experiments in the LSTF are described in this chapter, while the detailed information can be found in Hamilton *et al.* (2001) and in Hamilton and Ebersole (2001). [1]

2.1 Overview of the Laboratory Facility

2.1.1 General Facility Layout

The LSTF has dimensions of 30 m cross-shore by 50 m longshore by 1.4 m deep. The general layout of the LSTF is shown in Figure 2.1. A concrete beach, with approximately a longshore dimension of 31 m and a cross-shore dimension of

[1] Part of the material in this chapter is modified or quoted from the report by Hamilton *et al.* (2001).

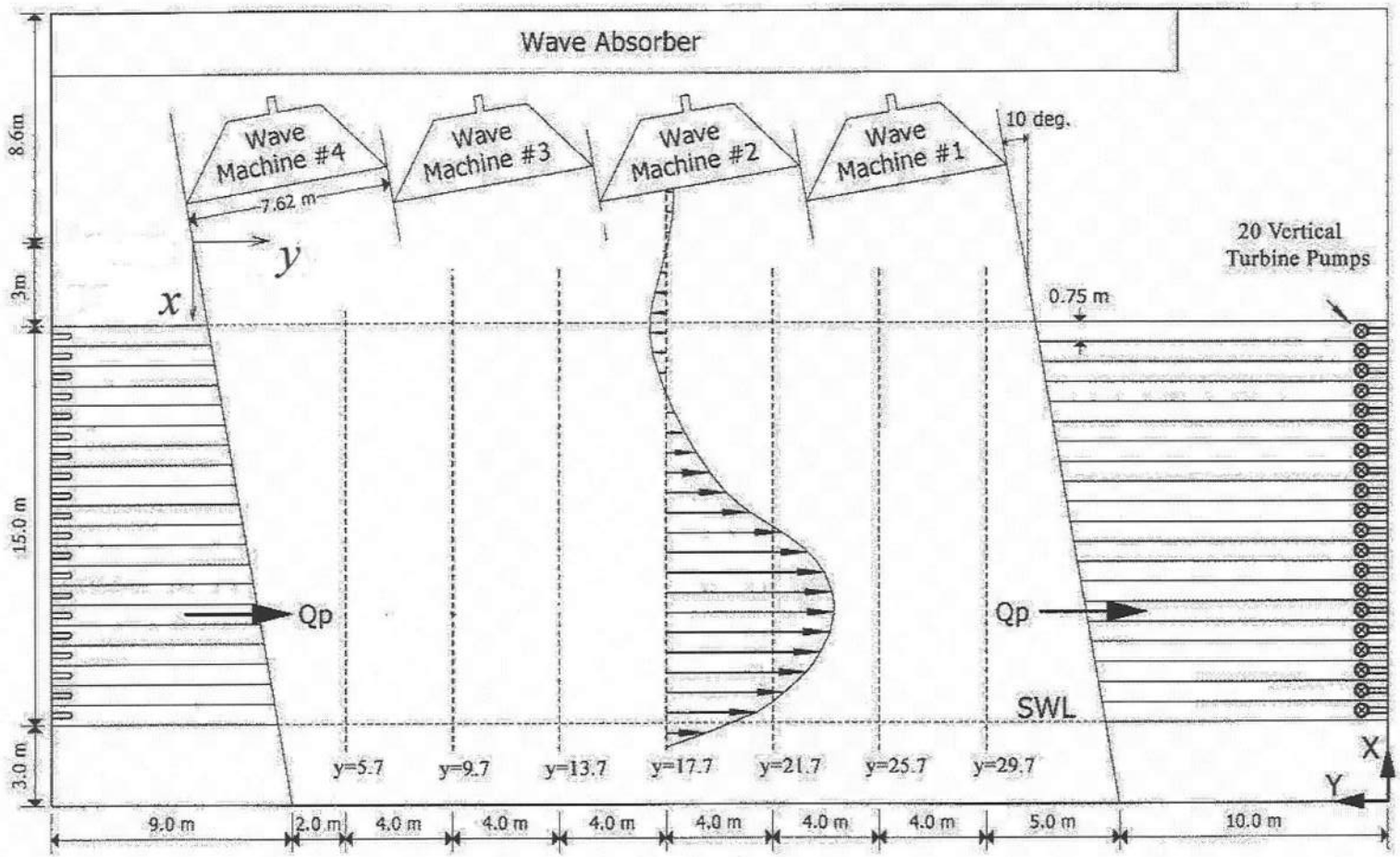

Figure 2.1: Plan view of the LSTF

21 m, is located in the central region of the facility, on top of which a sand beach was later constructed.

Four digitally controlled and servo-electric driven piston-type wave generators are located offshore to generate regular and irregular waves. Each of the wave boards is 7.62 m wide, and all the wave generators are synchronized to create a unidirectional long-crested wave front of 30.5 m in width. The wave generators can be oriented at various angles ranging from 0 to 20 degrees relative to shore normal, while the angle was set to 10 degrees in the experiments. A rubble mound wave absorber is located behind the wave generators to minimize wave reflections.

Twenty independent flow channels were built at the up- and down-stream boundaries of the facility. Each of the channel is 0.75 m wide except the one closest to the shoreline which is 3.75 m in width. Sediment-laden longshore currents flow toward the 20 downstream flow channels, each of which contains a low profile, gravity-feed sediment trap to measure the longshore sediment transport rate during experiments involving sediment transport. The longshore current is externally re-circulated from the downstream end back to the upstream of the facility through 20 independent pump-and-piping systems. The flow is then guided to the upstream end of the beach by the 20 upstream flow channels. The longshore current re-circulation system is essentially an active closed-loop system that continuously re-circulates the longshore current from the downstream boundary to the upstream of the beach while waves are being generated.

The discharge rates of the pumps are adjusted through an iterative process until a "desired" magnitude and cross-shore distribution of longshore currents for a given wave condition were achieved. The term "desired" is used to describe longshore currents with a high degree of longshore uniformity, which in reality is generated along an infinitely long straight beach.

Figure 2.2 sketches out the cross-shore profiles of the concrete and initial

sand beaches. The main section of the concrete beach has a constant slope of $1 : 30$ and the toe of the beach slopes down to the basin floor at a 1:18 slope. The moveable-bed beach was later constructed on top of the concrete beach using approximately 125 m^3 of very well sorted quartz sand with a median grain size of $D_{50} = 0.15\ mm$. The initial sand beach profile was determined based on results from the preliminary experiments and an analysis of the equilibrium beach profile for this grain size (Dean, 1977). The main section of the sand beach was graded to have a constant slope of approximately $1 : 27$, extending from the initial still-water shoreline to 16 m offshore. A sand berm was built behind the shoreline, with a front slope of $1 : 5.5$ and a height which exceeds the maximum excursion of wave runup in the swash zone.

The coordinate system used in the references for the LSTF experiments (as e.g., Hamilton *et al.* (2001) and Hamilton and Ebersole (2001)) was chosen so that the origin is at the downstream, shoreward end of the basin, the positive X-axis is directed offshore, the positive Y-axis is directed upstream, and the z-axis is measured positively upward relative to the still water level. However, the (x, y) coordinate system used in the present study was defined so that the origin is at the upstream, offshore end of the concrete beach, the positive x-axis is directed shoreward and the positive y-axis is downstream. These two coordinate systems, as illustrated in Figure 2.1, are related by

$$x = 21 - X \qquad\qquad y = 44.7 - Y \tag{2.1}$$

where (X,Y) is the coordinate system used in Hamilton *et al.* (2001) and Hamilton and Ebersole (2001).

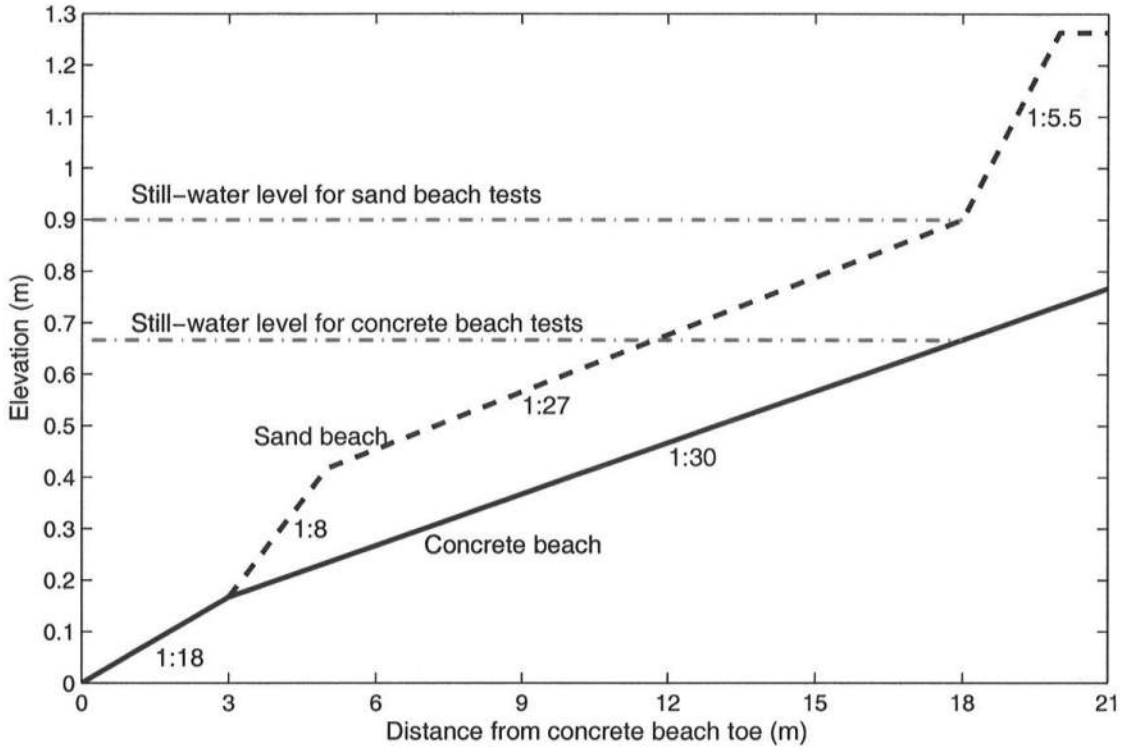

Figure 2.2: Cross-shore profiles of the concrete and initial sand beaches in the LSTF

2.1.2 Instrumentation

A semi-automated instrumentation bridge was used as a rigid platform for mounting wave gages, current meters, fib-optic backscatter sensors, and a fully automated bathymetric survey system. The bridge spans 21 m in the cross-shore direction and can traverse the entire length of the wave basin.

Fourteen single-wire capacitance wave gages were used to simultaneously measure the time series of water surface elevations. Ten of the wave gages were mounted along the bridge to measure wave transformations from the offshore zone, across the surfzone and into the swash zone. The other four gages are fixed in front of the four wave generators to measure offshore wave conditions. Only three of them actually functioned in the experiments.

Ten acoustic-doppler velocitimeters (ADV) were used to measure the instantaneous flow velocities. The ADVs were co-located with the wave gages along the bridge at about the same cross-shore location and were separated from the gages by approximately 0.4 m in the longshore direction. The ADVs were positioned so that the sampling volumes were located approximately one-third of the water depth above the bed in most tests, but their elevations were adjusted in some tests for the purpose of measuring vertical profiles of flow velocities.

Four vertical arrays of Fiber-Optic Backscatter Sensors (FOBS) were located along the bridge during the experiments involving sediment transport. Each array was co-located about midway in the longshore direction between the waves gage and the ADV and about the same cross-shore location. The FOBS simultaneously measured suspended sediment concentrations at 19 elevations in the water column.

Twenty Bottom Sediment Traps (BST) were located at the downstream end of the facility to measure the cross-shore distribution of longshore sediment transport rates. Eighteen sediment traps were positioned within 18 out of the 20 flow channels, one in each channel. Two shorter traps were located landward of the most-landward

Table 2.1: Instrumentation and sampling scheme in a sand beach experiment in the LSTF

Measurement	Instrument	Points in x	Sampling Rate	Sampling Duration	Vertical Profile
Surface Elevation	CWG	10	20 Hz	10 min	N/A
Currents	ADV	10	20 Hz	10 min	Yes
Sediment Concentration	FOBS	7	16 Hz	10 min	Yes
Sediment Flux	BST	20	4 Hz	Continuous	No
Beach Topography	ABSS	3660	Each Test	N/A	N/A

channel to quantify the sediment transport rate near the shoreline and in the upwash zone. The sand accumulated in the traps was dredged from the traps and discharged onto the upstream end of the beach after a significant amount of time.

A fully Automated 3-D Bathymetric Survey System (ABSS), consisting of a beach profile indicator and a x-y positioning system, was used to quantify spatial and temporal changes of beach bathymetry. The cross-shore profile was measured every 0.5 m along the beach for most tests, and the resolution is 0.005 m in the cross-shore direction for each transect.

A brief summary of the instrumentation and sampling scheme specific to a sand beach experiment is listed in Table 2.1.

2.2 Overview of Experimental Measurements

Several hydrodynamic and sediment transport experiments have been performed in the LSTF. Three of them, which are referred to as Test 6, Test 8 and Test 1 by Hamilton *et al.* (2001) and Hamilton and Ebersole (2001) were used in the comparisons in this study, and the experimental conditions are summarized in Table 2.2. In this table H_s stands for the significant wave height, T_p for the peak spectral period, α for the wave angle of incidence relative to shore normal and h_0 for the still water depth.

Table 2.2: Summary of experimental conditions

Test	Test 6	Test 8	Test1
Beach Type	Fixed-bed	Fixed-bed	Moveable-bed
Wave Type	Regular waves	Irregular waves	Irregular waves
Incident H_s (m)	0.18	0.23	0.25
Incident T_p $(sec.)$	2.5	2.5	1.5
Incident α $(deg.)$	10	10	10
Incident h_0 (m)	0.667	0.667	0.9

2.2.1 Hydrodynamic Experiments: Test 6 and Test 8

Both Test 6 and Test 8 are hydrodynamic experiments conducted on the concrete beach, one using regular waves and the other using irregular waves. Regular waves were generated in Test 6 with a wave height of 0.18 m, period of 2.5 seconds and incident angle of 10 degrees at the wave generators. Irregular waves were generated in Test 8 using a TMA spectrum. The incident significant wave height is 0.23 m, the peak spectral period is 2.5 seconds and the incident wave angle is 10 degrees. The significant wave height in Test 8 was selected so that the root-mean-square wave height H_{rms} was comparable to the wave height for the regular wave experiment (Test 6). The length of the driving signal was 500 seconds, 200 times the peak wave period.

A number of preliminary tests were carried out in each experiment before the formal test, in which the desired longshore uniform currents were produced and comprehensive measurements were conducted. The purpose of the preliminary tests is to find the proper magnitude and cross-shore distribution of the pumped flow rates to be used in the formal test. The tests were identified in Hamilton *et al.* (2001) and in Hamilton and Ebersole (2001) as Test 6A to Test 6N for the regular wave experiment and Test 8A to 8E for the irregular wave experiment.

During the formal tests, i.e., Test 6N and Test 8E, measurements were made

using wave gages and ADVs mounted on the instrumentation bridge at eight transects along the beach at the following alongshore coordinates of $y = 5.7$, 9.7, 13.7, 17.7, 21.7, 25.7, 29.7, 30.7 m. Along each of the eight transects, instant water surface elevations were measured at ten cross-shore locations and in front of three wave generators, and velocity components were measured at the elevation approximately one third of the local water depth above the bed at nine cross-shore locations. In addition, the instantaneous flow velocities were also measured along the transect of $y = 17.7\,m$ at various elevations. The cross-shore variations of wave heights, mean water levels and currents at eight transects as well as the vertical profiles of currents along the transect of $y = 17.7\,m$ were deduced afterwards.

2.2.2 Sediment Transport Experiment: Test 1

Test 1 in the LSTF is a comprehensive hydrodynamic and sediment transport experiment conducted on the sand beach. Irregular waves were generated in this test and the incident wave conditions are significant wave height of 0.25 m, peak spectral period of 2.5 seconds and wave angle of 10 degrees.

Numerous test segments, identified as Test 1A to Test 1H in Hamilton and Ebersole (2001), were conducted in this experiment. In addition to the purpose of establishing a proper pumping setting, another goal of the preliminary tests is to let the beach reach a near-equilibrium beach condition before the formal test (Test 1H) in which comprehensive measurements of hydrodynamics and sediment transport were performed. The hydrodynamic measurements in Test 1H were similar to those in Test 6N and Test 8E. The measurements involving sediment transport, which is the main purpose of Test 1H, include the instant longshore sediment transport rates measured by downstream sediment traps and the vertical profiles of instant sediment concentrations measured by the FOBS along the transect of $y = 22.7\,m$.

The comprehensive measurements of hydrodynamics and sediment transport in the LSTF were used in the present study to compare the model predictions against, which will be illustrated in chapters 4 and 7.

Chapter 3

THE KINEMATIC WAVE DRIVER MODELS

3.1 Basic Equations for the General Kinematic Wave Model

3.1.1 The General Governing Equations

The wave models used in the present study are based on the kinematic wave model which describes the shoaling and refraction of waves that can be described by a slowly varying amplitude or wave height H and a phase function θ. [1] Following Phillips (1969) this implies that the wave number (tensor) k_α (α denotes the direction of x_α, and $x_\alpha(\alpha = 1, 2)$ correspond to x and y in the Cartesian coordinate system) is given by

$$k_\alpha = \frac{\partial \theta}{\partial x_\alpha} \tag{3.1}$$

and it follows that the wave number vector is irrotational so that

$$\frac{\partial k_2}{\partial x_1} - \frac{\partial k_1}{\partial x_2} = 0 \tag{3.2}$$

and the spatial and temporal changes in ω and k_α are linked by the equation

$$\frac{\partial k_\alpha}{\partial t} + \frac{\partial \omega_a}{\partial x_\alpha} = 0 \tag{3.3}$$

where t denotes time.

[1] The material in this section was originally presented in the paper by Svendsen *et al.* (2003).

This equation states that any temporal variation in the wave number vector must be balanced by spatial changes in the absolute wave angular frequency ωa. In addition ωa is related to k_α, the local water depth h and current velocity V_α by

$$\omega_a = \omega_r + k_\alpha V_\alpha \tag{3.4}$$

where the relative frequency ω_r is given as a function of the numerical value k of k_α ($k = \sqrt{k_\alpha k_\alpha}$) by the dispersion relation for the wave motion

$$\omega_r = f(k, H, h) \tag{3.5}$$

The solution for k_α (and ω_a) corresponds to establishing the propagation pattern for the waves. The wave heights $H(x_\alpha, t)$ are then determined from the wave-averaged energy equation given by (Phillips, 1969)

$$\frac{\partial}{\partial t}(E - \frac{1}{2}\rho\frac{Q_{w\alpha}^2}{h}) + \frac{\partial}{\partial x_\alpha}\{E_{f\alpha} + V_\alpha E - \frac{1}{2}\rho Q_\alpha(\frac{Q_{w\alpha}}{h})^2\} = -S_{\alpha\beta}\frac{\partial V_\beta}{\partial x_\alpha} + \mathcal{D} - V_\alpha\overline{\tau_{b,\alpha}} \tag{3.6}$$

Here Q_α is the total volume flux in the wave-averaged motion, and V_α is the depth-averaged current velocity in that motion, E is the wave energy density, $Q_{w\alpha}$ is the wave volume flux, $E_{f\alpha}$ is the wave energy flux, $S_{\alpha\beta}$ is the radiation stress, $\mathcal{D}$ is the energy dissipation of wave breaking which is defined so that $\mathcal{D} < 0$ for energy loss and $\overline{\tau_{b,\alpha}}$ is the averaged bottom friction. The wave-averaged parameters E, $Q_{w\alpha}$, $E_{f\alpha}$ and $S_{\alpha\beta}$ are dependent on wave height H and phase variation. Hence, in order to determine the H from (3.6), all these parameters need to be linked to the wave height as described in the following.

It may be noticed that no limitation is placed on the phase function, which therefore does not have to be sinusoidal. On the other hand the seemingly simpler version of the kinematic model based on the concept of wave action E/ω rather than the wave energy E used here is only valid for the sinusoidal phase variation and the associated dispersion relation.

3.1.2 Dimensionless Wave-Averaged Parameters

To facilitate the solution of (3.6) we extract the H-variation from the wave-averaged quantities (i.e., the quantities averaged over the time scale of wave period). It is useful to define a dimensionless parameter for each of the quantities. These dimensionless parameters essentially represent the generalized shape of the wave (in the sense of surface profile, velocity and pressure field, etc). This approach will also greatly facilitate the parameterization of empirical data to be used inside the surfzone.

We write for the energy flux $E_{f,\alpha}$

$$E_{f,\alpha} \equiv \overline{\int_{-h_0}^{\zeta} [p_D + \frac{1}{2}\rho u^2] u_\alpha dz} = \rho g H^2 c_\alpha B \tag{3.7}$$

where ζ is the instantaneous water surface elevation relative to the still water level, h_0 is the still water depth, u is the total horizontal wave particle velocity, u_α is the $x-$ and $y-$ components of the wave particle velocity, c_α is the phase velocity vector defined from the wave speed c by the relation $c_\alpha = c\, k_\alpha / k$ and B is the dimensionless parameter for the energy flux.

For the energy density E the dimensionless parameter is B_E:

$$E \equiv \overline{\int_{-h_0}^{\zeta} \{\rho g z + \frac{1}{2}\rho u^2\} dz} - \int_{-h_0}^{\overline{\zeta}} \rho g z dz = \frac{1}{2}\rho g \overline{\eta^2} + \overline{\int_{-h_0}^{\zeta} \frac{1}{2}\rho u^2 dz} = \rho g H^2 B_E \tag{3.8}$$

where $\overline{\zeta}$ is the mean water level (MWL) and η is the water surface elevation relative to the MWL.

For the radiations stress $S_{\alpha\beta}$

$$S_{\alpha\beta} \equiv S_m\, e_{\alpha\beta} + S_p \delta_{\alpha\beta} = \rho g H^2 P_{\alpha\beta} \tag{3.9}$$

where $e_{\alpha\beta} = (k_\alpha\ k_\beta)/k^2$, the Kronecker delta $\delta_{\alpha\beta} = 1$ if $\alpha = \beta$ and $\delta_{\alpha\beta} = 0$ if $\alpha \neq \beta$,

$$S_m \equiv \overline{\int_{-h_0}^{\zeta} \rho u^2 dz} = \rho g H^2 P_m \tag{3.10}$$

$$S_p \equiv -\overline{\int_{-h_0}^{\zeta} \rho w^2 dz} + \frac{1}{2}\rho g \overline{\eta^2} = \rho g H^2 P_p \tag{3.11}$$

where w is the vertical wave particle velocity in the local vertical plane of wave propagation. Hence, $P_{\alpha\beta}$ is given by

$$P_{\alpha\beta} = P_m\, e_{\alpha\beta} + P_p \delta_{\alpha\beta} \tag{3.12}$$

For the wave volume flux $Q_{w\alpha}$ the dimensionless parameter B_Q is defined by:

$$Q_{w\alpha} \equiv \overline{\int_{-h_0}^{\zeta} u_{w\alpha}\, dz} = \frac{gH^2}{c}\frac{k_\alpha}{k} B_Q \tag{3.13}$$

The energy dissipation $\mathcal{D}$ for the breaking waves can be rewritten as

$$\mathcal{D} = \frac{\rho g H^3}{4hT} D \tag{3.14}$$

where D is the dimensionless parameter.

It is noted that (3.7), (3.8), (3.9) (with (3.10) and (3.11)) and (3.13) are the exact definitions for those quantities.

Specifying the phase variation will result in values for the dimensionless parameters B, B_E, $P_{\alpha\beta}$, B_Q and D. If exact expressions for the phase variation of the velocity, pressure field and surface elevation in the wave motion were inserted into the integrals the results for those parameters would also be exact. Solving (3.6) then gives the wave height variation. With wave heights H and phase speeds c known we can then determine in particular the volume flux $Q_{w\alpha}$ and the radiation stress $S_{\alpha\beta}$ which represent the major forcing parameters for circulation models.

3.1.3 Expressions for the Dimensionless Parameters Based on Different Wave Theories

Different representations of the wave phase motion by different wave theories result in different approximations of the dimensionless wave-averaged parameters and thus the derived wave properties such as wave height, phase speed and the wave-averaged dimensional parameters. In this study both the sinusoidal and non-sinusoidal wave theories were used to represent the wave phase motion, and the

resulting wave models are referred as sinusoidal and non-sinusoidal (cnoidal-bore) wave driver models, respectively.

The Sinusoidal Wave Theory

The sinusoidal (or linear) wave theory is the simplest approximation for the wave phase motion. In the present sinusoidal wave model the phase motion is described by the usual sine wave theory both inside and outside the surfzone. However, the effect of a roller is added to the wave-averaged parameters inside the surfzone.

For the phase speed c we use the general intermediate depth value of

$$c = \sqrt{\frac{g}{k} tanh\ kh} \tag{3.15}$$

where h is the water depth from the bottom to the mean water level. As the figures will show for the conditions of the experiments considered in this study this does not differ noticeably from the shallow water value of $\sqrt{gh}$.

Outside the surfzone we therefore have for the dimensionless parameters B and B_E, $P_{\alpha\beta}$ and B_Q

$$B = (1 + G)/16 \tag{3.16}$$

$$B_E = 1/8 \tag{3.17}$$

$$P_{\alpha\beta} = \frac{1+G}{16}\, e_{\alpha\beta} + \frac{G}{16}\delta_{\alpha\beta} \tag{3.18}$$

with

$$G = 2kh/\sinh 2kh \tag{3.19}$$

and

$$B_Q = 1/8 \tag{3.20}$$

For the computations with sinusoidal waves without a roller these expression also apply for surfzone waves. However, it is for simplicity assumed in the calculation of the wave-averaged parameters that the surfzone waves are in shallow water,

though this is of course no real limitation. With the shallow water wave assumption and the effect of the roller added we then get

$$B = B_E = \frac{1}{8} + \frac{1}{2}\frac{A}{H^2}\frac{h}{L}\frac{c^2}{gh} \tag{3.21}$$

$$P_{\alpha\beta} = \left(\frac{1}{8} + \frac{A}{H^2}\frac{h}{L}\right)\frac{c^2}{gh}e_{\alpha\beta} + \frac{1}{16}\delta_{\alpha\beta} \tag{3.22}$$

$$B_Q = \left(\frac{1}{8} + \frac{A}{H^2}\frac{h}{L}\right)\frac{c^2}{gh} \tag{3.23}$$

The roller area A in this sinusoidal and the following non-sinusoidal wave models are both determined using the results of Svendsen (1984) which suggested that

$$\frac{A}{H^2} = 0.9 \tag{3.24}$$

At this point it is also possible to use Okayasu *et al.* (1988)'s suggestion of $A/HL = 0.06$ but the above was found to give slightly better results in this study.

It is noted that waves no longer have sinusoidal shape when propagating to the nearshore and the sinusoidal wave theory may not be accurate enough for the description of the phase motions of nearshore waves, especially for waves close to breaking and inside the surfzone. Hence, an alternative non-sinusoidal wave theory is further used in this study to describe the wave phase motion: The cnoidal wave theory is used for waves outside the surfzone and non-sinusoidal long wave theory is used for surfzone waves.

The Cnoidal Wave Theory for Waves outside the Surfzone

The cnoidal wave theory is equivalent to assuming that waves are weakly nonlinear Boussinesq waves that are changing so slowly that their local shape corresponds to the constant depth solution on that location. The waves therefore follow the rules of shoaling and refraction of waves on a gently sloping bottom. As compared to sinusoidal waves, cnoidal waves are asymmetric about the horizontal axis,

with larger forward motion with shorter duration and small backward motion with longer duration.

The local cnoidal wave parameters are given by the local Ursell number defined by

$$U_r \equiv \frac{HL^2}{h^3} \tag{3.25}$$

and the wave shape is determined by the parameter m which is the solution to the equation

$$U_r = \frac{16}{3} m K^2 \tag{3.26}$$

where K is the complete elliptic integral of the first kind that is function of m.

This equation needs to be solved for each H and L at each depth h. This is done iteratively using standard algorithms for the elliptic integral K (see e.g. Press *et al.* (1986)). To follow the wave transformation from one point to another we therefore need to determine the evolution of the Ursell number as waves propagate.

For the energy flux $E_{f,\alpha}$ the dimensionless parameter B is given by (see e.g. Svendsen (1974))

$$B = B_0 \equiv \frac{\overline{\eta^2}}{H^2} \tag{3.27}$$

which can be evaluated as

$$B_0 = \frac{1}{3m^2} \left[\left(1 - 2\frac{E}{K} \right) \left(m - 1 + 2\frac{E}{K} \right) + \left(\frac{E}{K} \right)^2 \right] \tag{3.28}$$

where $E(m)$ is the complete elliptic integral of the second kind.

The phase speed c is given by

$$\frac{c^2}{gh} = 1 + A_c \frac{H}{h} \tag{3.29}$$

in which

$$A_c = \frac{2}{m} - 1 - \frac{3\,E}{m\,K} \tag{3.30}$$

We also have

$$B_E = B_0 \tag{3.31}$$

$$P_{\alpha\beta} = B_0\, e_{\alpha\beta} + \frac{B_0}{2}\,\delta_{\alpha\beta} \tag{3.32}$$

and

$$B_Q = B_0 \tag{3.33}$$

The Non-Sinusoidal Long Wave Theory for Surfzone Waves

Inside the surfzone the broken waves are very different from any simple wave shape we know such as linear waves, Stokes waves, stream function waves, cnoidal waves, and etc. Hence the conventional wave theories are no longer appropriate for the description of the surfzone waves. As a result, the dimensionless wave parameters are determined empirically for this region in the present study. For the inner surfzone waves, rollers are fully developed and a rather slow change in wave shape resembles periodic bores. On the other hand, immediately after wave breaking, rapid transitions of wave shapes occur and the rollers are very unstable (here termed the transition region and will be discussed in a separate section later).

Inside the surfzone we assume a hydrostatic pressure and a depth uniform particle velocity distribution in the wave motion. The wave-averaged effect of the wave shape is then again described by B_0. In addition, however, we also include the effect of the surface roller created by wave breaking. In this respect the model is equivalent to the model developed by Svendsen (1984), but in contrast, we use a nonlinear bore model to determine the phase speed c of breaking waves. This turns out to be important for some of the results. Hence we find for the dimensionless wave parameters inside the surfzone

$$B = B_E = B_0 + \frac{1}{2}\frac{A}{H^2}\frac{h}{L}\frac{c^2}{gh} \tag{3.34}$$

$$P_{\alpha\beta} = \left(B_0 + \frac{A}{HL}\frac{h}{H}\right)\frac{c^2}{gh}\, e_{\alpha\beta} + \frac{B_0}{2}\,\delta_{\alpha\beta} \tag{3.35}$$

$$B_Q = \left(B_0 + \frac{A}{HL}\frac{h}{H}\right)\frac{c^2}{gh} \tag{3.36}$$

The wave shape parameter B_0 is, however, evaluated using the empirical results for the (non-sinusoidal) waves inside the surfzone obtained by Hansen (1990) instead of using the value of 1/8 for sinusoidal waves.

$$B_0 = B_{0B}\ \{1 - a(b - h/h_B)(1 - h/h_B)\} \tag{3.37}$$

where B_{0B} is the value at the breaking point which can be determined with the cnoidal wave theory outside the surfzone. For a and b Hansen gave

$$a = (15\xi_{00})^{-1} \qquad\qquad b = 1.3 - 10(\xi_0 - \xi_{00}) \tag{3.38}$$

where ξ_0 and ξ_{00} were given by

$$\xi_0 = h_x/(H_0/L_0)^{1/2}; \qquad\qquad \xi_{00} = h_x/0.142^{1/2} \tag{3.39}$$

in which h_x is the spatial gradient of the water depth h in the x direction.

Energy Dissipation Inside the Surfzone

The energy dissipation $\mathcal{D}$ in breaking waves is due to wave energy being transformed to turbulent energy, and then to heat. The same method for calculating $\mathcal{D}$ is used in both sinusoidal and non-sinusoidal wave models.

The breaking process is often considered analogous to the situation in a hydraulic jump or a moving bore. A closer analysis shows that there is far more truth behind the intuitive concept than one should expect, but also shows a number of points where the two processes differ. Derivations for $\mathcal{D}$ and c were discussed by Svendsen *et al.* (1978).

From the derivation of Svendsen *et al.* (1978), the bore-equivalent of the wave speed was given by

$$\frac{c^2}{gh} = 1 + (-\frac{3}{2} + 3\frac{\eta_c}{H})\frac{H}{h} + (\frac{1}{2} - 3\frac{\eta_c}{H} + 3\frac{\eta_c^2}{H^2})(\frac{H}{h})^2 + (\frac{1}{2}\frac{\eta_c}{H} - \frac{3}{2}\frac{\eta_c^2}{H^2} + \frac{\eta_c^3}{H^3})(\frac{H}{h})^3 \tag{3.40}$$

where η_c is the crest elevation of the breaking wave.

The dimensionless energy dissipation can be written in terms of η_c as

$$D = -\frac{1}{\left(1 + \frac{\eta_c}{H}\ \frac{H}{h}\right)\left(1 + \frac{H}{h}\left(\frac{\eta_c}{H} - 1\right)\right)} \tag{3.41}$$

Therefore, inside the surfzone the wave crest elevation η_c/H, which is a measure of wave peakedness, is an important parameter for which Hansen (1990) found

$$\eta_c/H = 0.5 + \{(\eta_c/H)_B - 0.5\}\ (h/h_B)^2 \tag{3.42}$$

The Transition Region of the Surfzone

The model equations described above involve two non-physical peculiarities: For both wave models the roller area goes from zero to a finite value at the beginning of the surfzone; For the non-sinusoidal wave model the wave phase speed also has a discontinuity at the start of breaking. This causes singularities, in particular in the gradient of the radiation stress and the volume flux which act as forcing for the wave-induced currents, which is numerically unacceptable.

The roller, however, does not change discontinuously in reality. In fact in spilling breakers it takes some distance before the roller motion is fully developed and even in more violently breaking waves such as moderately plunging breakers the breaking process takes a distance to develop after the initial turnover of the wave.

Similarly, immediately after breaking the wave speed increases. Physically this is observed as a collapse of the wave front that looks like the wave tumbles forward. Mathematically it is represented by the fact that at the breaking point (3.40) gives higher wave speeds than (3.29).

These two criteria were used to smoothly link the wave properties of the roller area A and the phase speed c between the values at breaking and the values inside the surfzone. Cubic spline were used to describe the transitions which were assumed to take place over a distance of $L_t = rh_b$. The value of r would typically be 5-8 and in the present applications we used $r = 8$. This transition is similar to the

rules used in Boussinesq models for the variation of the roller area at the initiation of breaking (see e.g., (Schäffer *et al.*, 1993))

The general cubic spline function used for the transition is

$$Y_1 = a_3\, s^3 + a_2\, s^2 + a_1\, s + a_0 \qquad 0 < s < 1 \tag{3.43}$$

where Y_1 is the final result of the parameter (in the transition region) after applying the cubic spline, s is the distance from the breaking relative to the total width of the transition region

$$s = \frac{x - x_B}{L_t} \qquad x_B < x < x_B + L_t \tag{3.44}$$

and the coefficients

$$a_3 = 2Y_{0B} - 2Y_{0L} + L_t Y'_{0B} + L_t Y'_{0L} \tag{3.45}$$

$$a_2 = -3Y_{0B} + 3Y_{0L} - 2L_t Y'_{0B} - L_t Y'_{0L} \tag{3.46}$$

$$a_1 = L_t Y'_{0B} \tag{3.47}$$

$$a_0 = Y_{0B} \tag{3.48}$$

with Y_{0B} and Y_{0L} are the (known) values of the parameter at the ends of the transition region (i.e., at $x = x_B$ and at $x = x_B + L_t$), and Y'_{0B} and Y'_{0L} are the $x-$derivatives of the parameter. The coefficients a_3, a_2, a_1 and a_0 are evaluated so that the results of the parameter in the transition region (after using the cubic spline curve) can be smoothly linked to those outside the transition region. In another words, both the values and the x-derivatives of the parameter are continuous at the ends of the transition region.

3.2 Simplified Wave Model for Regular Waves on the Straight Beach

Many beaches have nearly straight and parallel contours, and the alongshore variation of wave parameters are negligible. This situation also applies for the beach

constructed in the LSTF. Thus, the wave models have been developed in this study especially for the wave propagation on a parallel straight beach.

We first consider regular waves, as in Test 6N in the LSTF. For regular waves propagating on a parallel straight beach, $\partial\ /\partial t = 0$ and $\partial\ /\partial y = 0$. Hence Equation (3.2) for the conservation of waves reduces to the Snell's law

$$\sin\alpha_w/c = (\sin\alpha_w/c)_i \ \equiv \ R_i \tag{3.49}$$

Here, α_w denotes the wave angle relative to the shore normal and subscript i represents the incident point where the wave parameters are known. After neglecting higher order terms, the wave-averaged energy equation (3.6) reduces to

$$\partial E_{fx}/\partial x = \mathcal{D} \tag{3.50}$$

Equations (3.49) and (3.50) are the well-known equations governing the shoaling and refraction of waves propagating on a parallel straight beach.

3.2.1 Waves outside the Surfzone

For waves outside the surfzone $\mathcal{D} = 0$ and the energy equation becomes

$$E_{fx} = E_{fx,i} \tag{3.51}$$

After plugging (3.7) for E_{fx} we have

$$H^2 Bc\cos\alpha_w = (H^2 Bc\cos\alpha_w)_i \tag{3.52}$$

Based on the Sinusoidal Wave Theory

Substituting (3.16) for B we get

$$H = H_i\, K_s\, K_r \tag{3.53}$$

where K_s is the shoaling coefficient

$$K_s = \sqrt{c_{g,i}/c_g} \tag{3.54}$$

in which c_g is the group velocity and $c_g/c = (1+G)/16$, and K_r is the refraction coefficient

$$K_r = \sqrt{\cos\alpha_{wi}/\cos\alpha_w} \tag{3.55}$$

Based on the Cnoidal Wave Theory

Plugging (3.27) for B yields

$$H^2 B_0 c\cos\alpha_w = (H^2 B_0 c\cos\alpha_w)_i \equiv F_i \tag{3.56}$$

which can be written as

$$H^2 Bc\sqrt{1-R_i^2 c^2} = F_i \tag{3.57}$$

after expressing $\cos\alpha_w = \sqrt{1-R_i^2c^2}$ based on the Snell's law (3.49).

Furthermore, (3.25) can be written as

$$U_r = \frac{T^2c^2H}{h^3} \tag{3.58}$$

We now have a complete system of three non-linear equations (3.57), (3.58) and (3.29), with one independent variable h and three unknowns U_r, H and c. This set of governing equations is similar to that used by Skovgaard and Petersen (1977). However, we took a further step herein to de-couple the equation systems to get analytical solutions.

Using (3.58) to eliminate c^2 in (3.57) and rearranging terms yields

$$H^3 - \beta_1 H^2 = \beta_2 \tag{3.59}$$

where

$$\beta_1 = R_i^2\frac{U_r h^3}{T^2} \tag{3.60}$$

$$\beta_2 = \frac{F_i^2 T^2}{B_0 U_r h^3} \tag{3.61}$$

Solving for H we get

$$\frac{H}{h} = \frac{1}{3}\left(\beta_1 + \frac{\beta_2^2}{3\beta_3} + \beta_3\right) \tag{3.62}$$

where

$$\beta_3 = \left(\frac{2{\beta_1}^3 + 27\beta_2 + 3\sqrt{12{\beta_1}^3\beta_2 + 81{\beta_2}^2}}{2} \right)^{\frac{1}{3}} \tag{3.63}$$

In addition, using (3.58) to eliminate c^2 in (3.29) and rearranging terms yields the shoaling-refraction equation for the cnoidal wave

$$U_r \left(\frac{H}{h}\right)^{-1} \frac{h}{gT^2} - A\frac{H}{h} = 1 \tag{3.64}$$

Numerical iterations are required to solve the equations (3.62) and (3.58) for the wave height H and the Ursell number U_r. The other wave parameters such as c, shape parameter B_0 and peakedness η_c/H can then be explicitly determined afterwards.

For normally incident waves, no wave refraction occurs. The shoaling-refraction equation for the cnoidal wave reduces to the shoaling equation obtained by Svendsen (1974)

$$\frac{(H_r B_r c_r T)^{\frac{2}{3}}}{h^2}(-U_r^{-\frac{1}{3}} B^{-\frac{2}{3}} A) + (\frac{h^2}{(H_r^2 B_r c_r T)^{\frac{2}{3}}}\frac{h}{gT^2})(U_r^{\frac{4}{3}} B^{\frac{2}{3}}) = 1 \tag{3.65}$$

3.2.2 Waves inside the Surfzone

Plugging (3.14) for the energy dissipation due to wave breaking into (3.50) and integrating from the breaking point we have

$$H/H_b = K_s K_R K_d \tag{3.66}$$

in which

$$K_s = \sqrt{c_b B_b / cB} \tag{3.67}$$

$$K_R = \sqrt{\cos\alpha_{wb} / \cos\alpha_w} \tag{3.68}$$

$$K_d = \{1 - \frac{H_b}{8c_b B_b T} \int_{x_b}^{x} \frac{D K_s^3 K_r^3}{h} dx\}^{-1} \tag{3.69}$$

where the subscript b again stands for the breaking point and the parameters at breaking are known based on the theories (models) for waves outside the surfzone.

It is noted that both c and D are dependent on wave height H based on the bore theory and thus iterations are required in order to solve for H. However, further investigations on (3.40) and (3.41) show that c^2/gh and D are sensitive to η_c/H but insensitive to H/h. Therefore, only a few iterations are required in order to obtain the final solution of H.

3.3 Simplified Wave Model for Irregular Waves on the Straight Beach

Waves in the field are usually irregular waves. Both wave height and wave period vary temporally instead of remaining constant. However, it still represents a big challenge to simulate the propagation of irregular waves. In this study the kinematic approach is applied in this study to simulating irregular wave propagation on a parallel straight beach. The basic assumption applied here is that the irregular waves are slowly varying waves, i.e., the temporal variations of wave heights and wave periods are on the time scale of wave groups. As a result, the transformation of irregular waves can still be described by (3.3) to (3.6).

3.3.1 Simplified Governing Equations

Although no spatial variation of beach topography exists in the longshore (y) direction for a parallel straight beach, irregular waves propagating on the beach still have spatial variations in y direction, as illustrated by (3.3). However, the spatial variation of irregular waves in the longshore direction is expected to be much smaller than that in the cross-shore direction, considering the fact that the cross-shore variation of beach bathymetry is the major mechanism of the neashore wave transformation. If we are particularly interested in the variations of the properties of slowly varying irregular waves with small incident angles on a parallel straight beach, the spatial variation of waves in the longshore direction can be neglected for simplicity, as we do in the present study.

After neglecting the longshore variation of wave properties, $\partial/\partial y$ in (3.3) and (3.6) becomes zero. Furthermore, after inserting (3.4) for ω_a and $w_r = kc$ into (3.3) we have

$$\frac{\partial k\cos\alpha_w}{\partial t} = -\frac{\partial}{\partial x}\{\ k(c + U\cos\alpha_w + V\sin\alpha_w)\ \} \tag{3.70}$$

where U and V are the depth-averaged current velocities in the x and y directions, respectively. This equation can also be rewritten in terms of kh as

$$\frac{\partial(kh\cos\alpha_w)}{\partial t} = -\frac{\partial}{\partial x}\{\ kh(c+U\cos\alpha_w+V\sin\alpha_w)\ \} + k(c+U\cos\alpha_w+V\sin\alpha_w)\frac{\partial h}{\partial x} \tag{3.71}$$

Neglecting high order terms in (3.6) gives

$$\frac{\partial E}{\partial t} = -\frac{\partial}{\partial x}\{E_f\cos\alpha_w + UE\} + \mathcal{D} - \left(\ S_{xx}\frac{\partial U}{\partial x} + S_{xy}\frac{\partial V}{\partial y}\ \right) - U\overline{\tau_{bx}} \tag{3.72}$$

Expressing E_f in terms of E yields

$$\frac{\partial E}{\partial t} = -\frac{\partial}{\partial x}\{E(nc\cos\alpha_w + U)\} + \mathcal{D} - \left(\ S_{xx}\frac{\partial U}{\partial x} + S_{xy}\frac{\partial V}{\partial y}\ \right) - U\overline{\tau_{bx}} \tag{3.73}$$

where $n = B/B_E$. As discussed in section 3.1.2, $n = 1$ for cnoidal waves outside the surfzone and long waves inside the surfzone, while $n = (1+G)/2$ for sinusoidal waves outside the surfzone and can be approximated by 1 for shallow water waves.

3.3.2 Numerical Solution

It is noted that both (3.71) and (3.73) are convection-type equations. Therefore, the same numerical scheme is used to solve (3.71) and (3.73) for $kh\cos\alpha_w$ and E, respectively. The predictor-corrector scheme is used for the time difference, as done in SHORECIRC. The Adams-Bashforth scheme is used for the predictor, and the Adams-Moulton scheme is used for the corrector. The second order upwind difference scheme is used for the convection terms, i.e., $\frac{\partial}{\partial x}\{\ kh(c+U\cos\alpha_w+V\sin\alpha_w)\ \}$ in (3.71) and $\frac{\partial}{\partial x}\{E(nc\cos\alpha_w + U)\}$ in (3.73). The second order upwind scheme is

selected to avoid the wiggle problem and numerical diffusion problem. The same numerical scheme is also used later to solve the diffusion-convection equation for suspended sediment concentration, as detailed in section 5.4.6.

After $kh\cos\alpha_w$ and E are obtained in a predictor or corrector step, wave parameters can be determined as follows:

1. Given $kh\cos\alpha_w$, k and α_w are determined using Snell's law (3.49).

2. Determine H and c for waves outside the surfzone.

   (a) For sinusoidal waves, c is determined using the dispersion relation (3.15) in which k is known; and H is derived from (3.8) in which E is known and $B_E = 1/8$.

   (b) For cnoidal waves, $B_E = B_0$ which is dependent on the Ursell number U and thus on H. Substituting (3.25) for H in (3.8) and rearranging terms give

   $$U^2 B_0 = \frac{E}{\rho g}\frac{16\pi^4}{k^4 h^6} \tag{3.74}$$

   where B_0 is a function of U. Therefore, U can determined numerically from this equation for a given E. After U is known, dimensionless parameters for cnoidal waves such as B_0 and A_c can be found. Finally, H is explicitly derived from (3.8) provided E and $B_E = B_0$, and c is determined using (3.29).

3. Determine H and c for waves inside the surfzone. As illustrated in (3.34), B_E is a function of c^2/gh which is dependent on H/h as shown in (3.40). However, a further analysis shows that c^2/gh is insensitive to H/h, and thus a few iterations are required to solve for H for a given E. After H is known, c is determined using (3.40).

While several relations have been proposed for determining the location of wave breaking in terms of H, H/h or kh, the criterion of wave breaking still remains uncertain, particularly for irregular waves. Here the breaking criterion described in Svendsen (1987) for regular waves is used to determine the breaking location of the individual wave within the irregular wave group. The breaking criterion proposed by Svendsen (1987) is

$$(kh)_B = \frac{2\pi}{2.30} \left(\frac{H_0}{L_0}\right)^{-1/2} \tag{3.75}$$

where H_0 and L_0 are the deep-water wave height and wavelength, respectively.

The boundary conditions used in the irregular wave model include the time series of wave heights, wave periods and wave angles in the offshore reference.

Chapter 4

COMPARISONS OF NEARSHORE HYDRODYNAMICS BETWEEN MODEL PREDICTIONS AND MEASUREMENTS

This chapter is to present the comparisons of wave properties and wave-induced circulation between the measurements, particularly in Test 6N and Test 8E in the LSTF, and the results predicted by the wave models, as described in Chapter 3, coupled with the SHORECIRC.

4.1 Comparisons of Nearshore Hydrodynamics under Regular Waves

The main objective of the comparisons of the nearshore hydrodynamics under regular wave environments is to investigate the accuracy of the two wave models used for driving nearshore circulation, and how the inevitable inaccuracies in the predictions of wave quantities influence the current predictions. [1]

In addition to the measurements in Test 6N in the LSTF by Hamilton and Ebersole (2001) (H&E) other experimental data used in the comparisons include the experiments by Hansen and Svendsen (1979) (H&S), by Cox *et al.* (1995) and Cox and Kobayashi (1997) (CK&O), by Ting and Kirby (1994) (T&K), and by Svendsen and Veeramony (2001) (S&V).

[1] The material in this section was originally presented in the paper by Svendsen *et al.* (2003).

Table 4.1 lists the incident wave conditions and bottom slopes in the experiments used in the comparisons. In the table subscript i refers to the values of wave parameters as generated. In most cases the bathymetry corresponded to a section with a horizontal bottom followed by a plane beach with the slope indicated in the last column. It is also noticed that the waves generated in these experiments are close to shallow water waves from the incident point.

Test	$h_i(m)$	$T(sec)$	$H_i(m)$	U_i	h_i/L_i	bottom slope
H&E	0.667	2.50	0.18	21.3	0.113	1:18 ((x<3.m), 1:30 (x>3.m)
H&S (H)	0.36	1.67	0.10	17.5	0.127	1:34.26 (x>14.78m)
H&S (K)	0.36	1.67	0.08	14.0	0.128	1:34.26 (x>14.78m)
H&S (N)	0.36	2.00	0.07	18.7	0.102	1:34.26 (x>14.78m)
H&S (P)	0.36	2.50	0.07	30.6	0.078	1:34.26 (x>14.78m)
H&S (Q)	0.36	2.50	0.04	17.5	0.079	1:34.26 (x>14.78m)
CK&O	0.40	2.20	0.125	35.4	0.094	1:35 (x>11.85m)
T&K	0.40	2.00	0.125	37.9	0.106	1:35 (x>11.85m)
S&V	0.40	1.50	0.06	6.4	0.153	1:35 (x>11.85m)

Table 4.1: Incident wave parameters in the experiments used in the comparisons. For the measurements by H&S, H, K, N, P and Q refer to individual experiments, H&E stands for Test 6N in Hamilton and Ebersole (2001b), H&S for Hansen and Svendsen (1979), CK&O for Cox et al. (1995, 1997), T&K for Ting and Kirby (1994) and S&V for Svendsen and Veeramony (2001).

4.1.1 Wave Properties

The short wave properties used in the comparisons include the wave height, wave peakedness, phase speed, wave-averaged parameters such as the radiation stress and wave volume flux.

Variation of Wave Heights

We first analyze the development of the wave height, which is the quantity most frequently measured and which has the greatest influence on all the wave parameters including the velocity field.

Comparisons of predicted wave heights with measurements at 8 transects in Test 6N in the LSTF are presented in Fig. 4.1. The y-value refers to the longshore location in our coordinates for each transect (see Fig. 2.1).

For completeness Fig. 4.2 shows the comparisons with the 1-D measurements by H&S, T&K, CK&O, and S&V. We see that the results are very similar to the comparisons in Fig. 4.1. Similar comparisons have been shown in the literatures before though sometimes with slightly different versions of the cnoidal wave theory (Svendsen and Brink-Kjær (1972), Skovgaard and Petersen (1977) to mention a few). It is therefore as expected that in all cases the cnoidal-bore model gives a much more accurate prediction of the wave height than the sine wave theory, particularly in the region close to breaking.

Wave Peakedness η_c/H

Figure 4.3 presents the comparisons of the wave peakedness η_c/H between the measurements from Ting and Kirby (1994) and Cox et al. (1995, 1997) and the model predictions. The experimental data shows that waves become more and more peaked as propagating to breaking at which η_c/H reaches the maximum value. However, inside the surfzone waves become less and less peaked as they propagate towards the shoreline. The comparisons show that while η_c/H is assumed to be a constant of 0.5 based on the sine wave model, it is predicted quite well by the cnoidal-bore wave model.

Phase Speed

Measurements of the phase speed are only available from a few of the published experiments. The most extensive set of results (Fig. 4.4) were measured by H&S and a few can be extracted from the measurements by S&V. [2] No phase speed

[2] The S&V experiments were actually conducted with wave groups but the results shown in Fig. 4.4 are for the smallest groupness of only 10% variation in wave height.

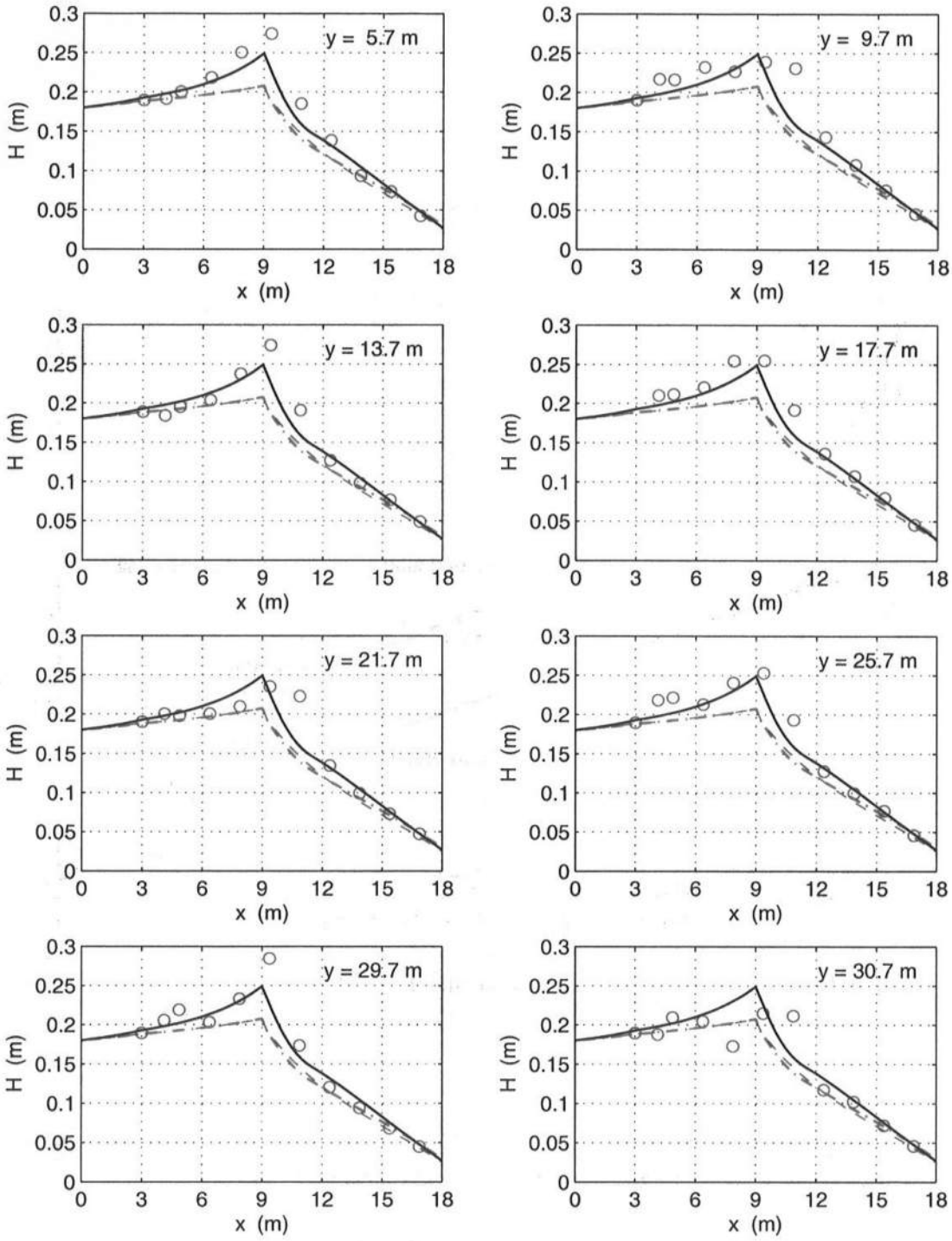

Figure 4.1: Comparisons of wave heights (H) between the experimental data ($\circ$) in Test 6N from Hamilton and Ebersole (2001) and the predictions using the cnoidal-bore model (—), the sine wave model with a roller ($-\cdot$) and that without a roller ($--$)

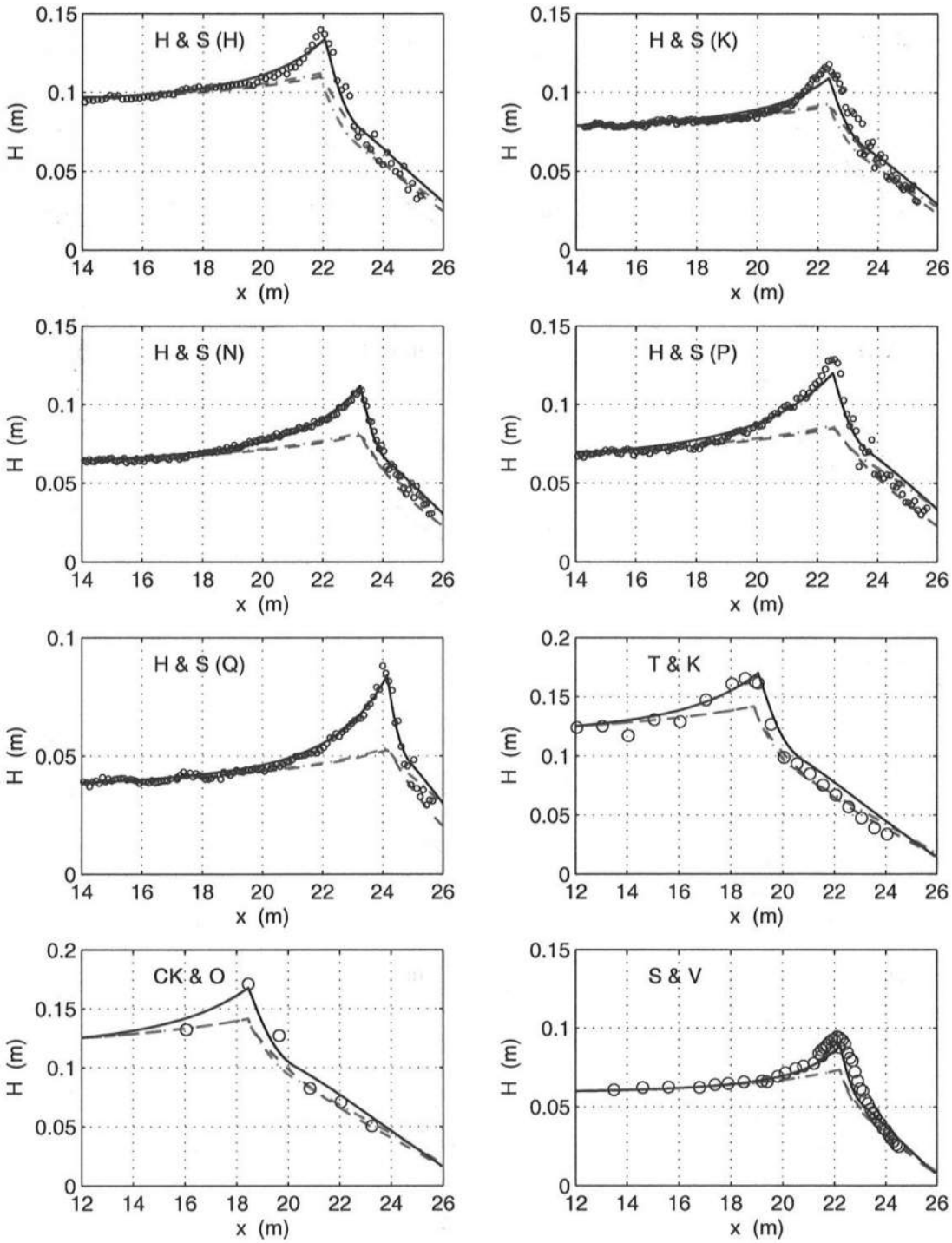

Figure 4.2: Comparisons of wave heights (H) between the experimental data ($\circ$) from Hansen and Svendsen (1979), Ting and Kirby (1994), Cox et al. (1995, 1997) and Svendsen and Veeramony (2001) and the predictions using the cnoidal-bore model (—), the sine wave model with a roller ($-\cdot$) and that without a roller ($--$)

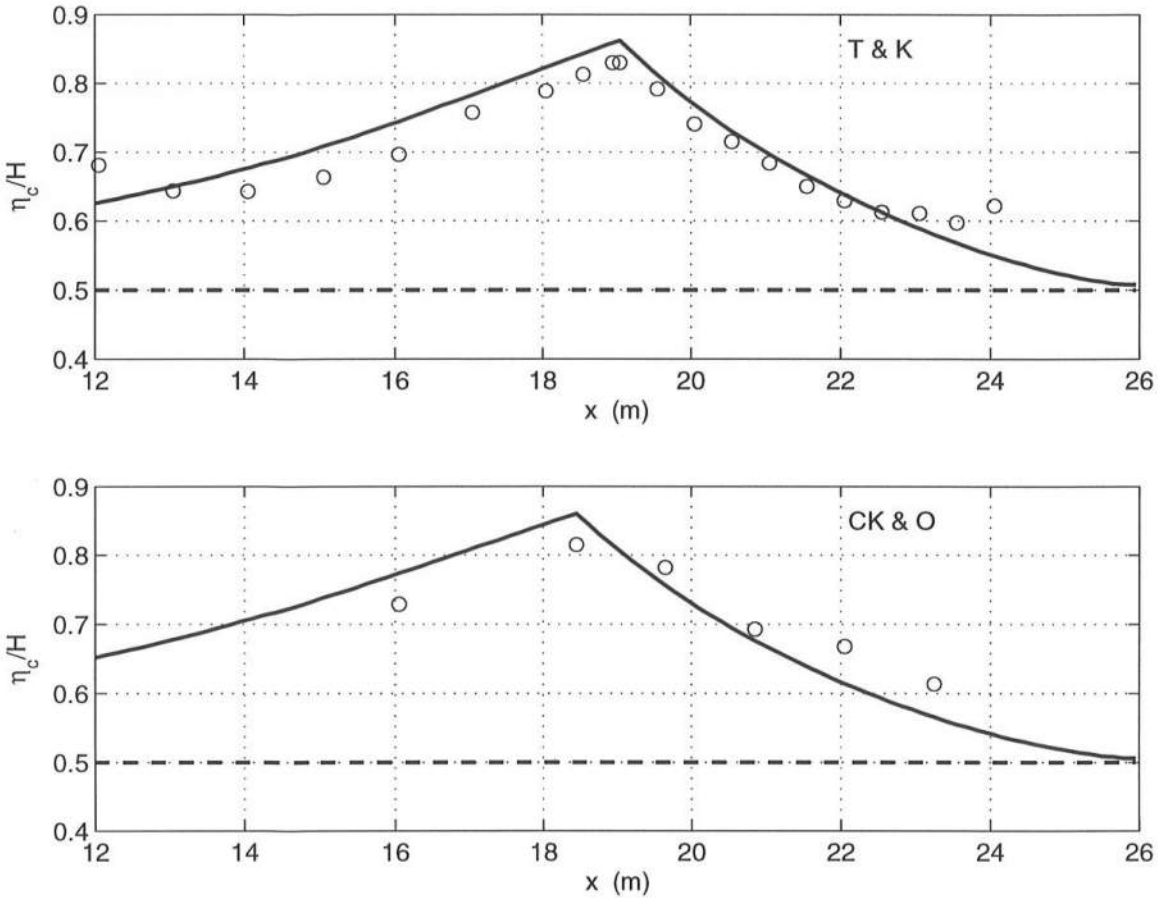

Figure 4.3: Comparisons of the wave peakedness η_c/H between the experimental data ($\circ$) from Ting and Kirby (1994) and Cox et al. (1995, 1997) and the predictions using the cnoidal-bore model (—) and the sine wave model (– –)

measurements were obtained from the LSTF experiments.

The phase speeds measured in the experiments are absolute speeds c_a^m relative to a fixed point, where index m stands for measured. However, a weak return current U occurs in a 1-D laboratory wave flume or a longshore uniform beach. In average, over the depth U has the value of

$$U = -\frac{Q_w}{h} \tag{4.1}$$

In a 1-D or a longshore uniform case this compensates for the forward volume flux

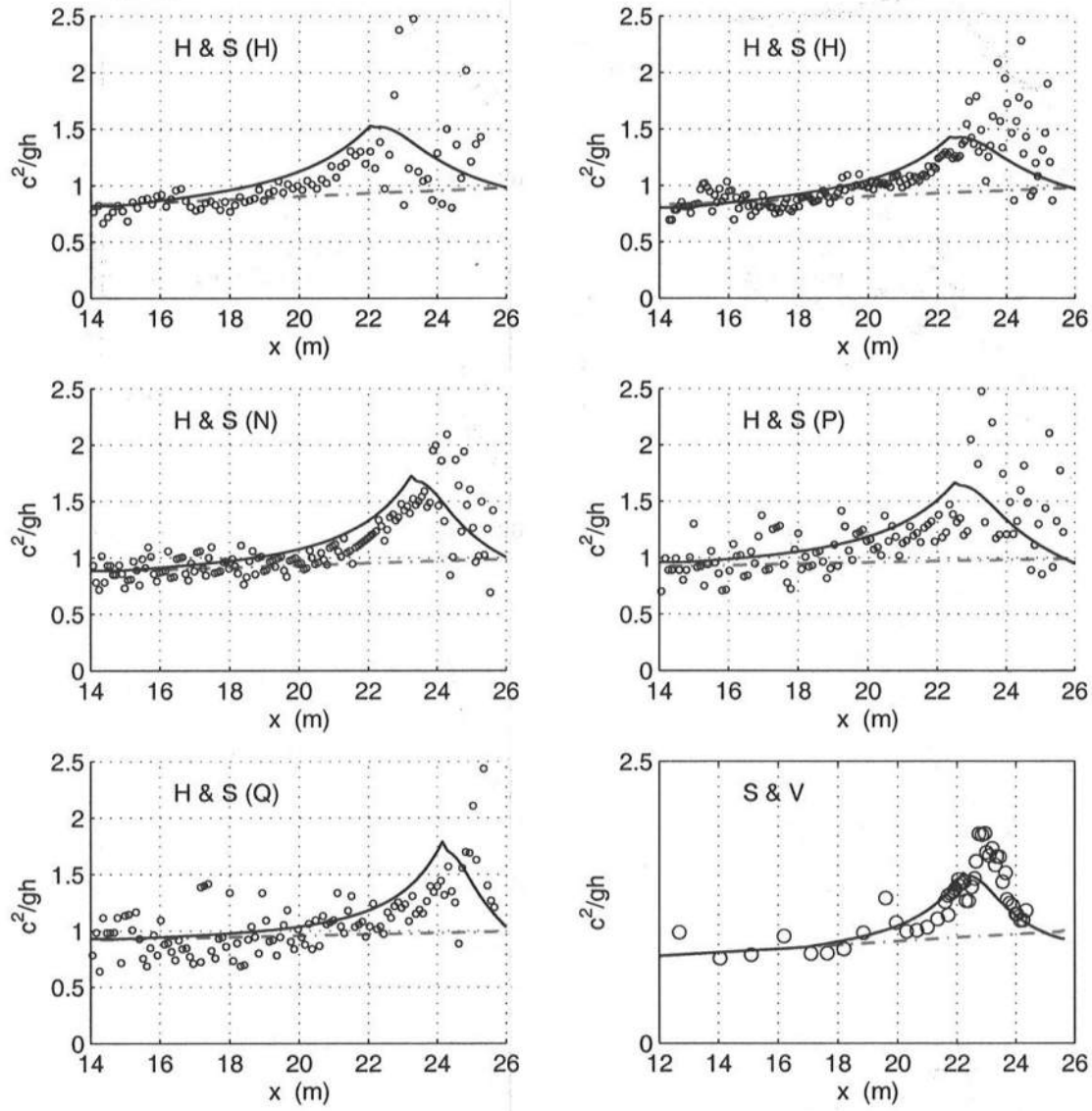

Figure 4.4: Comparisons of c^2/gh between the experimental data ($\circ$) from Hansen and Svendsen (1979) and Svendsen and Veeramony (2001) and the predictions using the cnoidal-bore model (—) and the sine wave model (–·)

Q_w created by the waves, since there can be no net cross-shore volume flux under those conditions.

The dispersion relationship provided by wave theories represents the relative (or "intrinsic") phase speed c_r (that is the phase speed relative to the water). Hence the relationship between c_a^m and c_r is

$$c_a^m = c_r + U \;=\; c_r - Q_w/h \tag{4.2}$$

or

$$c_r = c_a^m + \frac{Q_w}{h} \tag{4.3}$$

Since Q_w/h is typically $5-8\%$ of c, the actual c_r is $\sim$ 1.05–1.08 times the measured c_a^m.

As Fig. 4.4 shows, a significant scatter of c^2/gh were clearly observed in the measured data, in particular after breaking. However, the trend is clear: as waves approach breaking the values of c^2/gh increase to values of $1.2-2.0$. The cnoidal wave model picks up this trend very well while for sine wave models the values of c^2/gh are nearly constant (because the waves in the experiments are nearly shallow water waves throughout).

Perhaps more surprisingly the values of c^2/gh decrease dramatically inside the surfzone. Though this may be a little difficult to discern from Fig. 4.4, it becomes more evident if a moving average is performed for the measured results. This is again very clearly depicted by the bore model for c^2/gh used here.

Considering the role of c in the expressions for the energy flux E_f in (3.13) and the volume flux Q_w in (3.7), it is not surprising that this substantial variation in the phase speed and the accurate representation by the model is one of the most important factors for improving the accuracy of the predictions of the wave-averaged parameters.

Wave-Averaged Parameters: Radiation Stress and Setup

One of the major problems in the verification of wave models used as wave drivers is that the radiation stress $S_{\alpha\beta}$ cannot be measured directly with any of the existing measuring techniques. However, the setdown/setup variation of the mean water level has been measured in all the experiments used here. Since the radiation stress in the 1-D or the longshore uniform case can be linked to the mean water level by the simple equation (after neglecting the small bottom shear stress)

$$\frac{\partial S_{xx}}{\partial x} = -\rho g h \frac{\partial \overline{\zeta}}{\partial x} \tag{4.4}$$

we can get direct information about the variation of radiation stress by examining the variation of mean water level. As this equation shows, an increase in radiation stress will cause a decrease in mean water level and vice versa. Figs. 4.5 and 4.6 show that the present model represents the variations of mean water levels accurately. However, so does the sine wave model with a roller, which seems surprising since the sine wave theory does not predict wave heights very well.

The reason is that the radiation stress is a product of the square of wave height and the shape parameter $P_{\alpha\beta}$ (see (3.9)). As waves approach breaking wave heights increase. The sine wave theory does not pick that up well and hence we would expect it to underestimate the increase in radiation stress near breaking. This is not the case because at the same time the actual waves become more and more peaked as approaching breaking: crests shorter and more peaked, troughs longer and flatter. The result is a decrease in $P_{\alpha\beta}$ for the real waves as approaching breaking, which will counteract the increase in wave heights. The sine wave theory does not pick that up either. Hence, the relatively good performance of the sine wave theory in predicting the variation of mean water levels before breaking is fortuitously due to two counteracting errors: the under-predicted wave height and the over-predicted shape parameter $P_{\alpha\beta}$. On the other hand, the cnoidal wave theory represents both effects quite well and hence also predicts the $S_{\alpha\beta}$ and setup variations correctly.

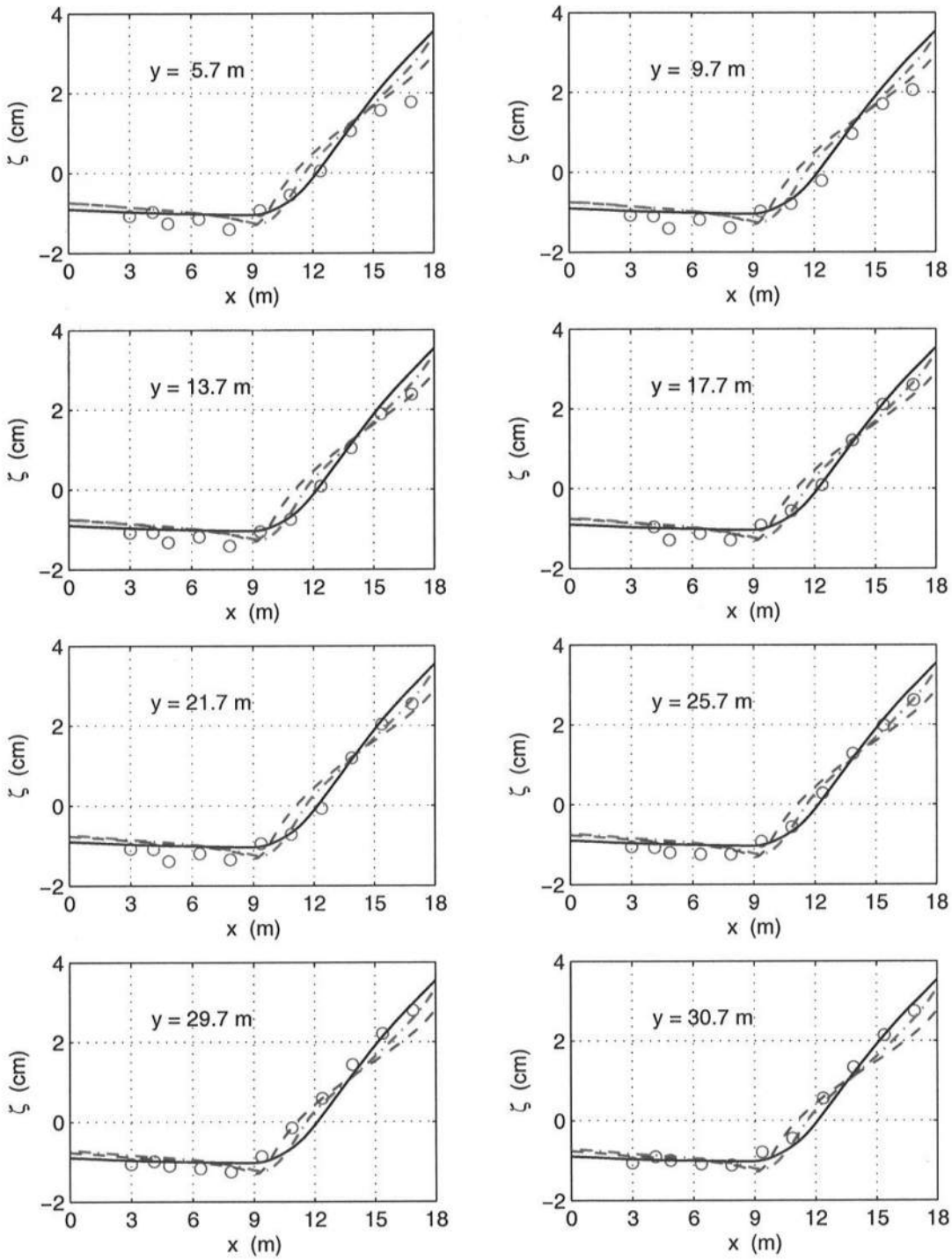

Figure 4.5: Comparisons of mean water levels ($\bar{\zeta}$) between the experimental data ($\circ$) in Test 6N from Hamilton and Ebersole (2001) and the predictions using the SC with the cnoidal-bore wave driver (—), with the sine wave driver with a roller ($-\cdot$) and with the sine wave driver without a roller ($--$)

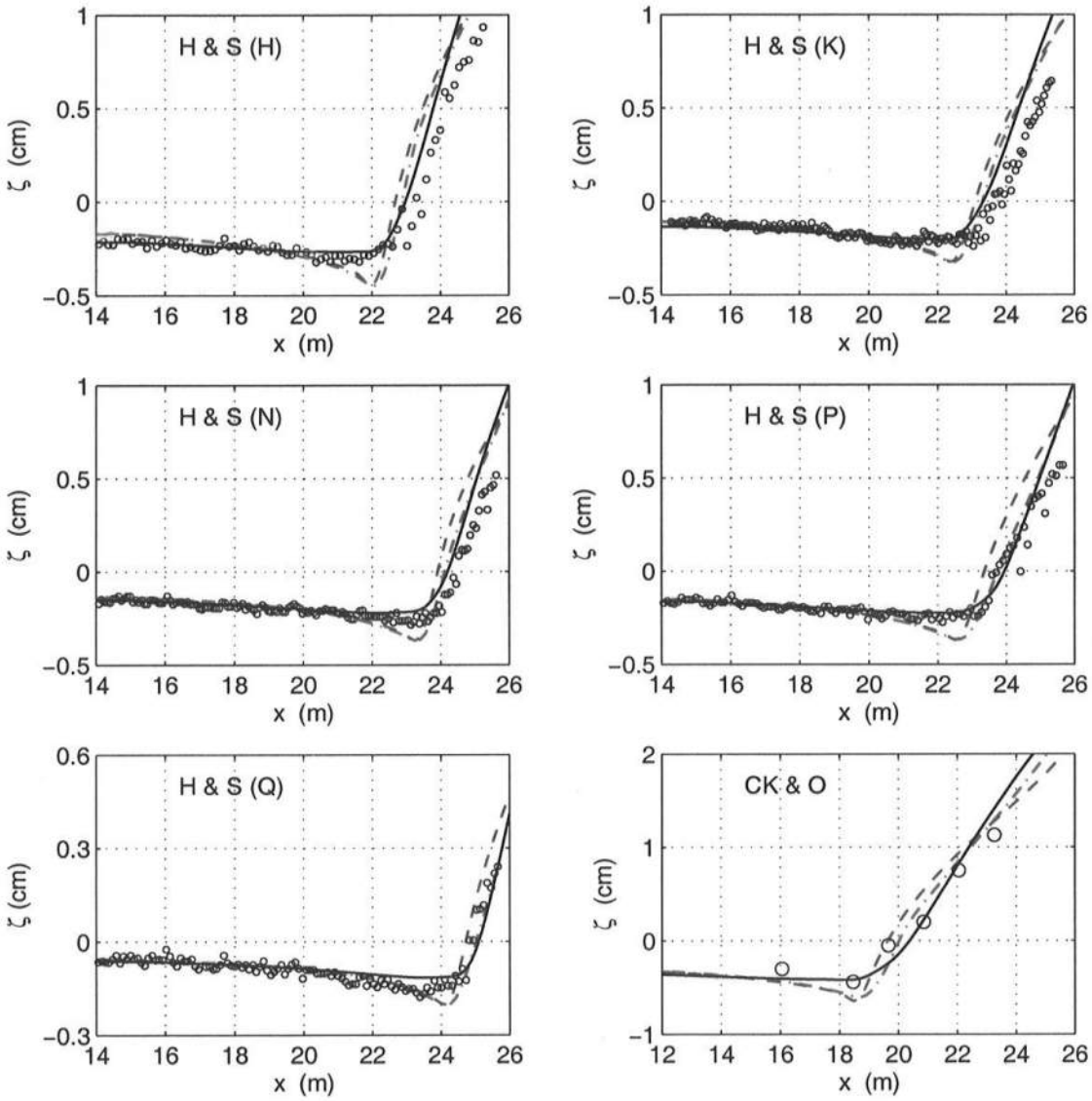

Figure 4.6: Comparisons of mean water levels ($\bar{\zeta}$) between the experimental data ($\circ$) from Hansen and Svendsen (1979) and Cox et al. (1995, 1997) and the predictions using the SC with the cnoidal-bore wave driver (—), with the sine wave driver with a roller ($-\cdot$) and with the sine wave driver without a roller ($--$)

Inside the surfzone the situation is reversed. Immediately after breaking starts wave heights decrease rapidly, but at the same time waves become less peaked so $P_{\alpha\beta}$ increases as discussed by Putrevu and Svendsen (1993). The result is at first a very small change in mean water levels right after breaking corresponding to an almost constant radiation stress (Svendsen, 1984). Further shoreward, however, the decrease in wave heights dominates with the well-known setup as a consequence.

Again, while the bore theory with the empirical B_0 used in the surf zone picks up these counteracting trends quite well, the sine wave driver (with the roller included) also provides remarkably accurate prediction of the mean water level variation, and hence the radiation stress, simply by ignoring these two counteracting trends.

Wave-Averaged Parameters: Volume Flux and Undertow

The lack of direct measurements of the important wave-averaged parameters also applies to the short wave volume flux, $Q_{w\alpha}$, which originates from the nonlinear effects between the trough and crest of the wave. Most measuring techniques have difficulties covering this region. In a longshore uniform wave tank and a 1-D wave flume, however, the volume flux can be obtained from the measurement of the undertow. By integrating the undertow velocity profiles (which are relatively easy to measure) over depth and using the overall continuity equation we get the wave volume flux

$$Q_w = -\frac{1}{\cos \alpha_w} \int_{-h_0}^{\bar{\zeta}} U(z) dz \tag{4.5}$$

in which the wave angle $\alpha_w = 0$ for 1-D flume experiments. To perform the integration the measured values of the undertow velocity profiles can be approximated by a least-square-fit of a second order polynomial. This also makes it possible to carry the integration to the mean water surface $\bar{\zeta}$. This is the approach used here for obtaining measured values of Q_w. This can be done for all the experiments where

the undertow velocity profiles were measured, essentially the experiments by H&E, T&K and CK&O.

Figure 4.7 presents the comparisons of the volume fluxes in the same setting as before. The figure is similar as for the other quantities though the documentation clearly is much weaker due to the limited number of measurements available. It is seen that the cnoidal-bore model predicts the volume flux through the whole nearshore region quite well. While the sine wave driver (with a roller) also shows good accuracy for the inner surfzone, it over-predicts the volume flux before breaking and in the outer surfzone.

Figure 4.8 shows the equivalent values of the shape parameter B_Q derived from the volume fluxes. Waves outside the surfzone become more and more peaked as approaching breaking (see Fig. 4.3), resulting in a decrease in B_Q. While the sine wave theory gives a constant of 0.125 for B_Q, the cnoidal wave model can well represent the decrease in B_Q. For surfzone waves B_Q first increases then decreases as waves propagate towards the shoreline due to the combined effects of rollers and wave shape variations. The cnoidal-bore model predicts the increase in B_Q for the outer surfzone very well while the sine wave driver is much less accurate in that region. Despite the fact that the measurements in the inner surfzone are insufficient, the bore model seems to generally pick up the decrease in B_Q for the inner surfzone. It is worthy to mention that the under-estimation by the sine wave driver of the wave height and the over-estimation of the shape parameter does not again add up to an accurately balanced prediction of the wave volume flux as was the case for the radiation stress.

4.1.2 Wave-Induced Currents

The comparisons and analyses above have shown the importance of balancing all the wave properties. The next step is to use the wave models as the drivers in the SC model for comparisons with the measurements of 3-D currents induced by

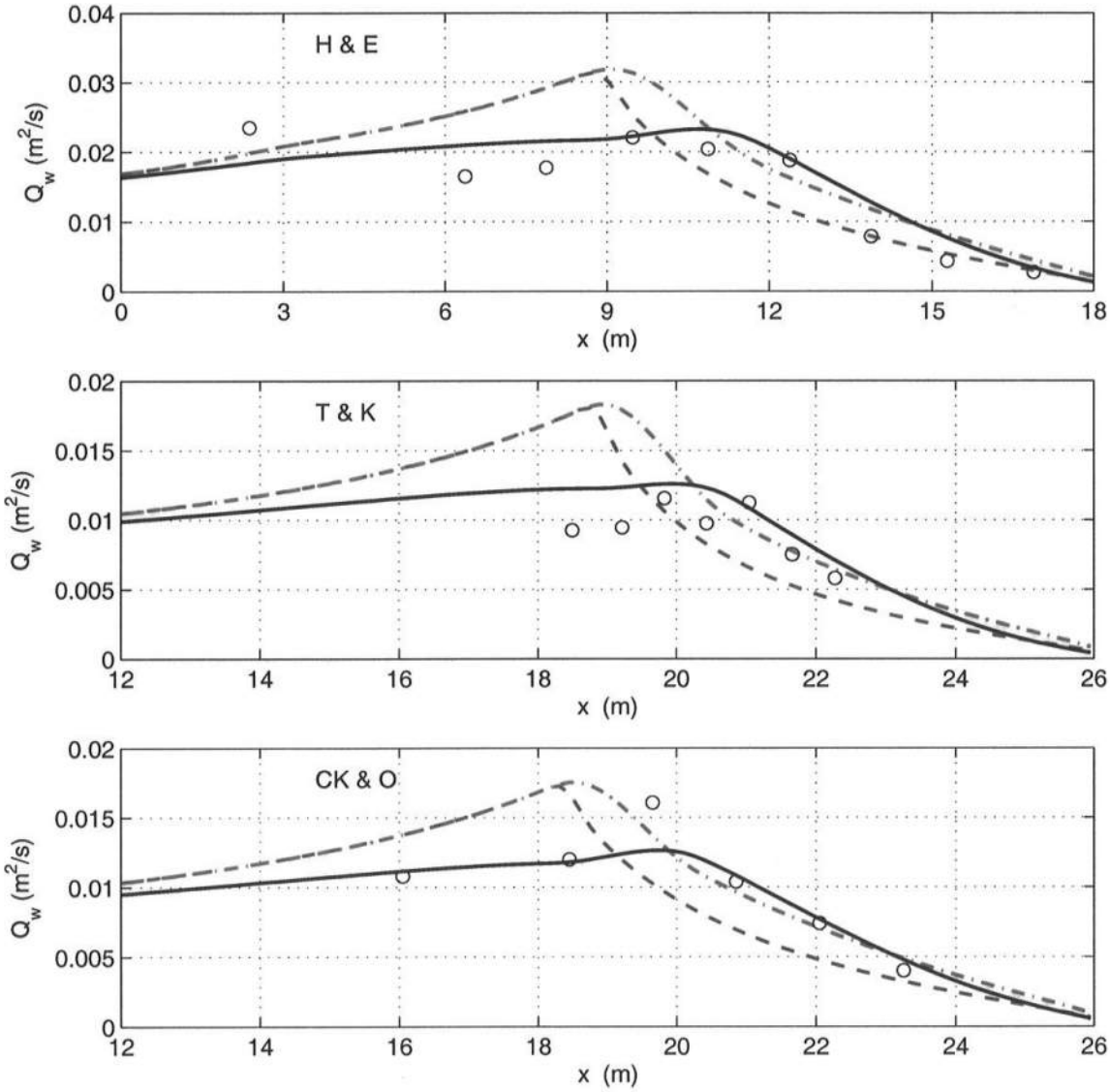

Figure 4.7: Comparisons of the wave volume flux Q_w between the experimental data ($\circ$) from Hamilton and Ebersole (2001), Ting and Kirby (1994), and Cox et al. (1995, 1997) and the predictions using the cnoidal-bore model (—), the sine wave model with a roller ($-\cdot$) and that without a roller($--$)

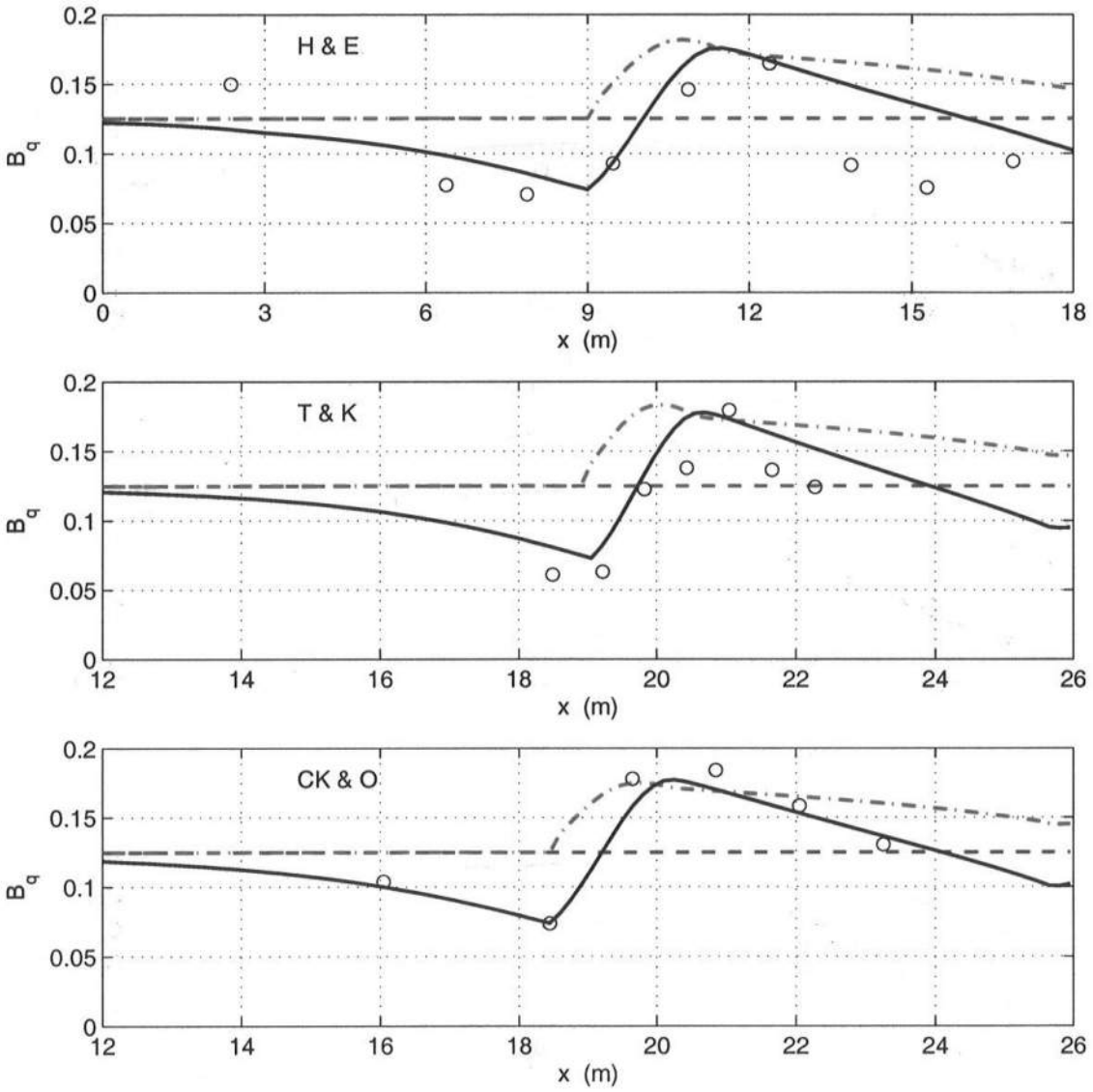

Figure 4.8: Comparisons of B_q between the experimental data ($\circ$) from Hamilton and Ebersole (2001), Ting and Kirby (1994), and Cox et al. (1995, 1997) and the predictions using the cnoidal-bore model (—), the sine wave model with a roller ($-\cdot$) and that without a roller($--$)

regular waves in Test 6N in the LSTF.

Longshore Currents

Figure 4.9 presents the comparisons with the LSTF measurements of the cross-shore variations of depth-averaged longshore currents at seven transects. Again, y-values refer to the longshore locations for transects in our coordinate system. The currents are positive to the left and breaking occurs around $x = 9\,m$. The currents were actually measured in the experiment at elevations approximately one third of the water depth above the bed. However, as shown later in Fig 4.11, the vertical profile of longshore currents is almost uniform over the water depth. Thus it is reasonable to compare the measured longshore currents to the computed depth-averaged values. From the measurements it is seen that a reasonable longshore uniformity was achieved except for the areas close to the lateral boundaries. The SC with the two wave driver models predict longshore currents reasonably well except for the area close to upstream boundary ($y \sim 0$) where very small or even negative longshore currents were measured close to shoreline.

As might be expected from the relatively equal prediction of the radiation stress, the two wave drivers incorporated in the SC predict similar results for the longshore currents with perhaps a slight advantage to the cnoidal-bore model, especially for the inner surf zone.

Figure 4.10 shows the comparisons of the current vectors at elevations one third of the water depth above the bed. Only results for the cnoidal-bore wave driver are presented. The agreement between the model predictions and the measurements are very good, both in directions and in magnitudes, except for the area close to the upstream boundary where flow patterns are complex. For most areas the wave-induced currents flow towards the downstream and seaward direction.

One of the important features of the SC model is that it also predicts the vertical variation of currents and the dispersive lateral mixing associated with this.

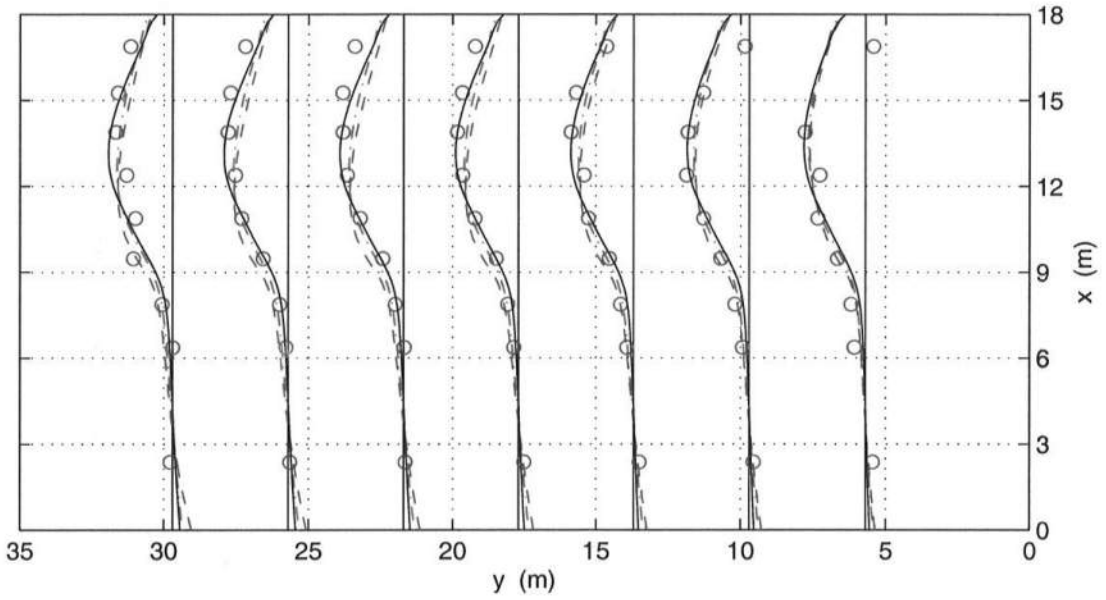

Figure 4.9: Comparisons of longshore currents (V) between the experimental data ($\circ$) in Test 6N from Hamilton and Ebersole (2001) and the predictions using the SC with the cnoidal-bore wave driver (—), with the sine wave driver with a roller($-\cdot$) and with the sine wave driver without a roller($--$)

Comparisons of the vertical profiles of longshore currents between model predictions and measurements are demonstrated in Figure 4.11 for the transect of $y = 17.7\,m$ which is around the middle of the facility. The x-values refer to the cross-shore positions of the sensors and ξ is the vertical location above the bed. The vertical profiles of longshore currents are nearly depth-uniform, as illustrated both by the simulated results and by the measurements. Using the values at the elevation one third of the water depth above the bed to represent the depth-averaged longshore currents gives a reasonable approximation.

However, there is a trend of slight changes in the vertical profile of longshore currents with the distance from the shore. Inside the surfzone the longshore currents increase slightly from the seabed towards the surface, and outside the surfzone this tendency is reversed so that the maximum value of $V(z)$ appears near the bottom.

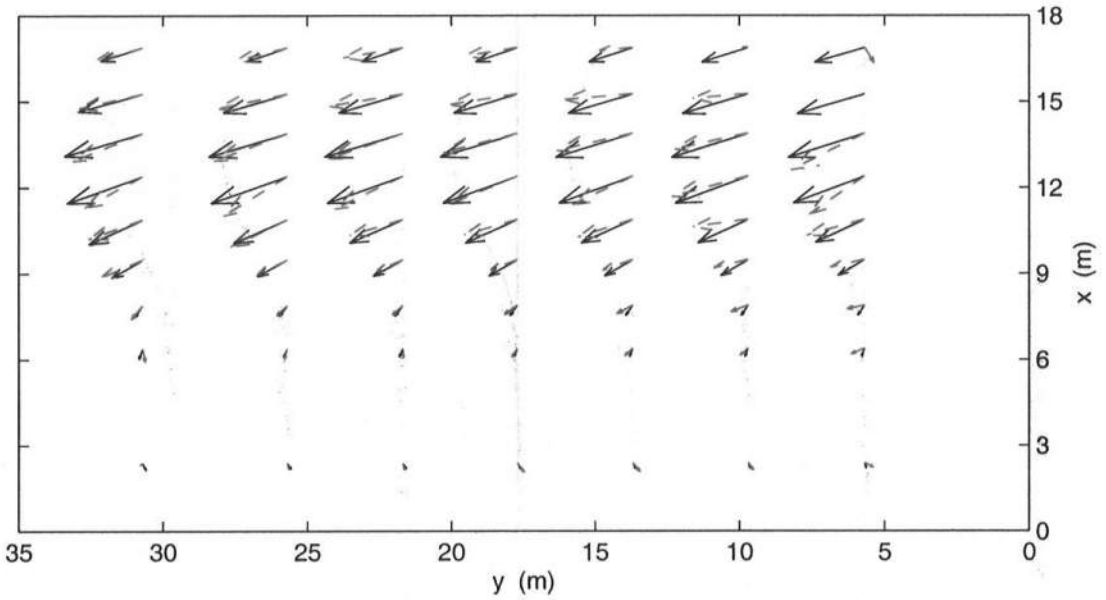

Figure 4.10: Comparisons of currents at 1/3h above the bed between the experimental data ($- \rightarrow$) in test 6N from Hamilton and Ebersole (2001) and the prediction using the SC with the cnoidal-bore wave driver ($\longrightarrow$)

As shown in Fig. 4.11 this trend is clearly the same in both the LSTF measurements and the modeling results. A similar trend was found in the measurements by Visser (1984) and was confirmed theoretically by Putrevu and Svendsen (1994). They showed that this is an essential feature associated with the mechanism of the convective cross-shore momentum transfer which constitutes the dispersive lateral mixing. It is therefore valuable to see it confirmed again.

Cross-Shore Currents

Similarly Figure 4.12 compares the measured and computed vertical profiles of cross-shore currents for the transect of $y = 17.7\,m$. In contrast to longshore currents, the undertow profiles show strong variations with the water depth. As always, inside the surfzone the cross-shore velocities have the seaward-oriented maximum close to the bottom and decrease to small values near the surface. Outside the

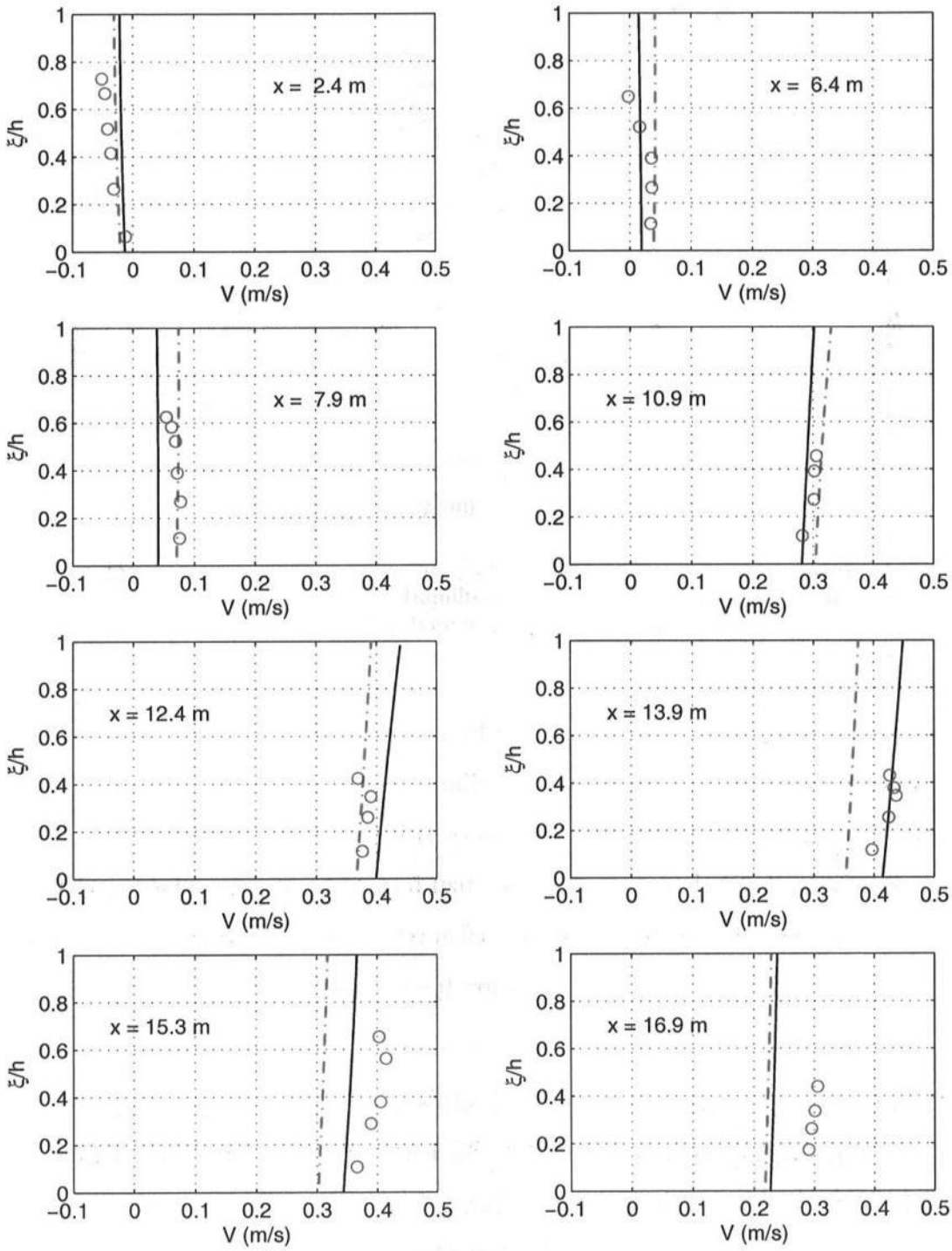

Figure 4.11: Vertical profiles of longshore currents from the experimental data (∘) in Test 6N (Hamilton and Ebersole, 2001) compared with the predictions using the SC with the cnoidal-bore wave driver(—) and the SC with the sine wave driver with a roller(−·)

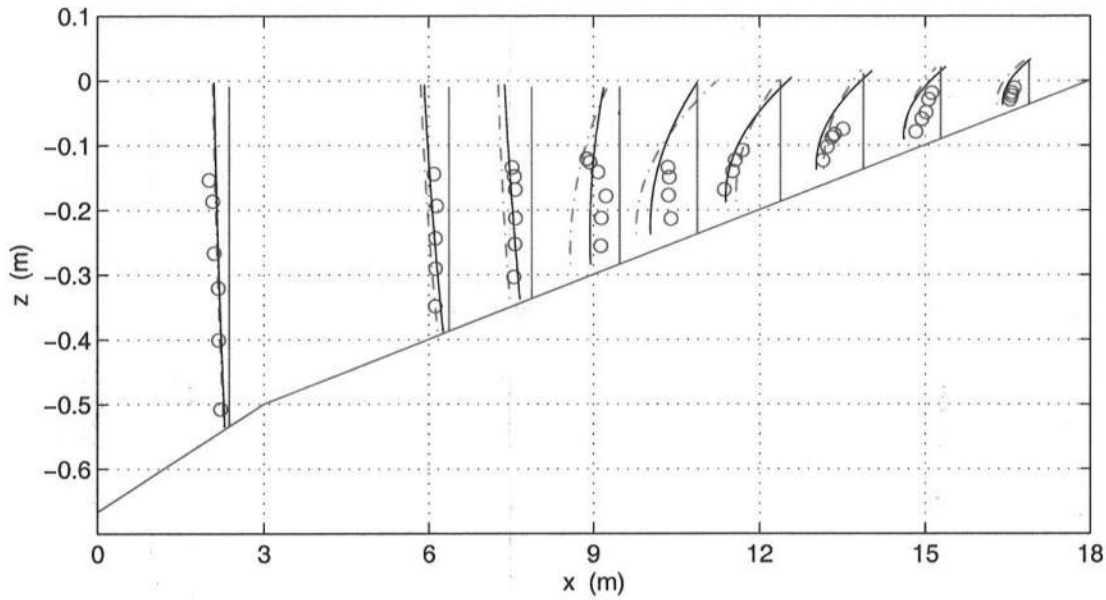

Figure 4.12: Vertical profiles of cross-shore currents from the experimental data (∘) in Test 6N (Hamilton and Ebersole, 2001) compared with the predictions using the SC with the cnoidal-bore wave driver(—) and the SC with the sine wave driver with a roller(−·)

surfzone the bottom values of the velocities are smaller and the velocities increase slightly toward the surface. This trend is the same in both the modeling results and the measurements as shown in Fig. 4.12. The vertical shapes of the undertow profiles are reasonably well predicted by the SC with either the cnoidal-bore wave driver or the sine wave driver with a roller. However, the SC with the cnoidal-bore wave driver generally shows much better accuracy in predicting magnitudes of undertows. Since the volume fluxes Q_w for the measurements were derived from the undertow measurements it is clear that the trends in the comparisons of Q_w in Fig. 4.7 will be mirrored to the comparisons of undertows here.

3-D Current Profiles

The vertical profiles of currents are summarized in Figure 4.13 which shows a 3-D plot of the measured and the computed vertical profiles of current vectors for

the transect of $y = 17.7\,m$. The figure illustrates that the currents vary over depth not only in magnitudes, but also in directions. This is in agreement with many earlier model simulations (as e.g., Haas and Svendsen, 2000; Haas *et al.*, 2000), but it is believed to be the first time that it is has been demonstrated in extensive 3-D laboratory experiments.[3]

4.1.3 Analysis of Model Skills

A crude assessment of the model capability can be obtained by considering the root-mean-square errors of the simulation results relative to the measurements, as listed in Table 4.2. The results include wave heights H, dimensionless phase speeds c^2/gh, mean water levels $\bar{\zeta}$, volume fluxes Q_w and longshore currents V. In the table, σ_1 denotes the rms errors if the sine wave driver with a roller is used, and σ_2 denotes the rms error if the cnoidal-bore wave driver is used.

The rms values for the cross-shore averaged errors essentially confirm the general impression of the more detailed comparisons presented in the figures. However, it is also obvious that such simple, one-figure measures of accuracy fall short of illustrating the variations of the errors. For example the fact that the relatively large errors for phase speeds in both theories mainly stem from the fact that the measurements show very large scattering inside the surfzone and particularly immediately after breaking.

They also do not reveal that in spite of the seemingly equally small errors for both theories in predicting the setup/setdown the cnoidal/bore theory may, as Figs. 4.5 and 4.6 indicate, be somewhat better at predicting the setup inside the surfzone where the gradient of $\bar{\zeta}$ (and thereby the forcing) is largest.

---

[3] Similar results can be inferred from field data if the longshore and cross-shore profiles in the two papers Garcez-Faria *et al.* (1998) and Garcez-Faria *et al.* (2000) are combined.

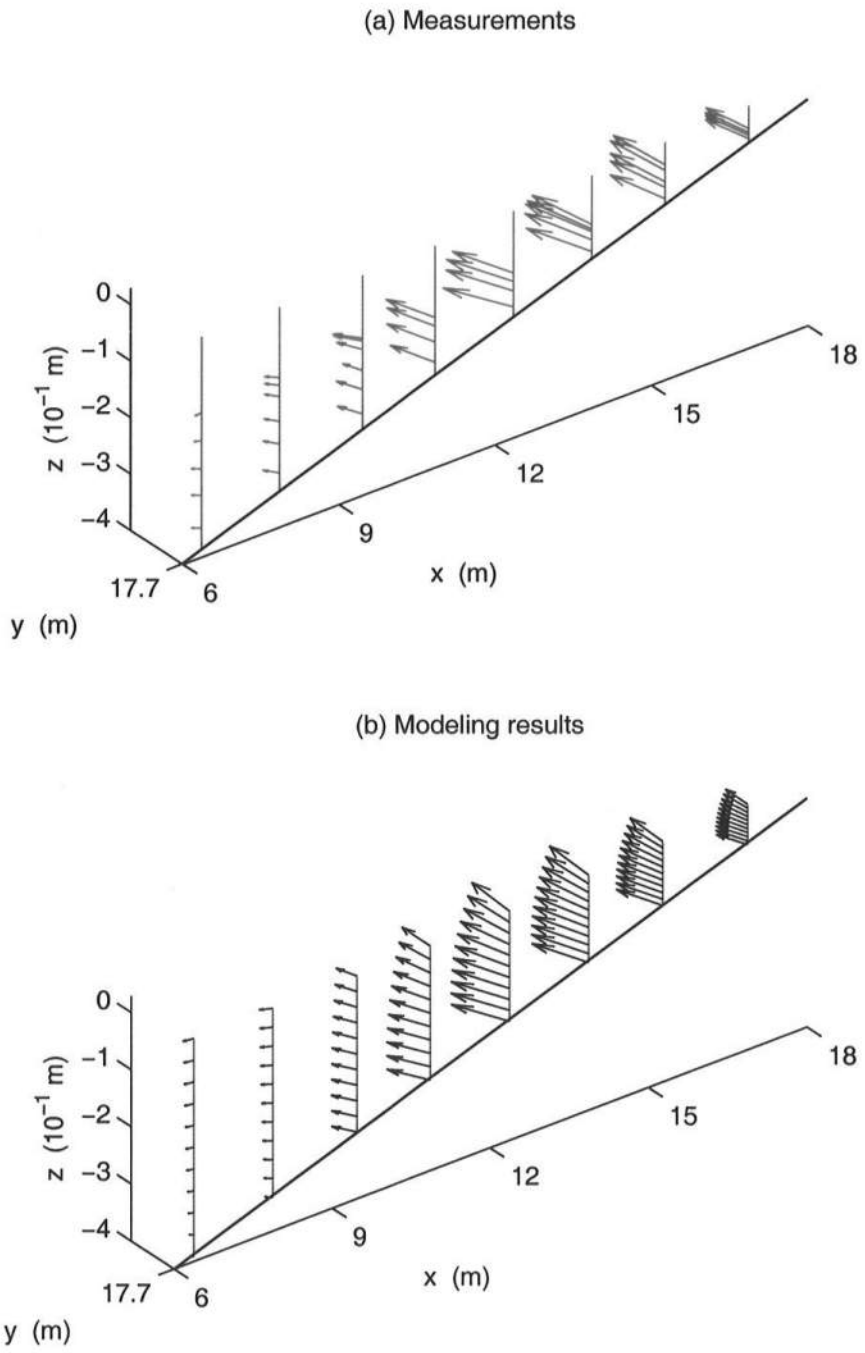

Figure 4.13: Vertical profiles of current vectors: (a) from experimental data in Test 6N (Hamilton and Ebersole, 2001), and (b) predicted by the SC with the cnoidal-bore wave driver

Test	H&E	H&S(H)	H&S(K)	H&S(N)	H&S(P)	H&S(Q)	T&K	CK&O	V&S
$\sigma_1(H)(m)$	0.032	0.011	0.010	0.009	0.014	0.009	0.013	0.016	0.013
$\sigma_2(H)(m)$	0.020	0.005	0.005	0.003	0.006	0.002	0.009	0.009	0.007
$\sigma_1(c^2/gh)$	–	0.317	0.396	0.345	0.576	0.342	–	–	0.446
$\sigma_2(c^2/gh)$	–	0.253	0.299	0.217	0.464	0.275	–	–	0.195
$\sigma_1(\zeta)(cm)$	0.270	0.140	0.112	0.090	0.076	0.025	–	0.164	–
$\sigma_2(\bar{\zeta})(cm)$	0.256	0.139	0.110	0.084	0.064	0.028	–	0.150	–
$\sigma_1(Q_w)(m^2/s)$	0.006	–	–	–	–	–	0.005	0.003	–
$\sigma_2(Q_w)(m^2/s)$	0.003	–	–	–	–	–	0.002	0.001	–
$\sigma_1(V)(m/s)$	0.062	–	–	–	–	–	–	–	–
$\sigma_2(V)(m/s)$:	0.059	–	–	–	–	–	–	–	–

Table 4.2: Root-mean-square errors of the model predictions of wave heights H, c^2/gh, mean water levels $\bar{\zeta}$, volume fluxes Q_w and longshore currents V for the experiments used in the comparisons. σ_1 is the rms error if using the sine wave driver with a roller and σ_2 is the rms error if using the cnoidal-bore wave driver.

4.2 Comparisons of Nearshore Hydrodynamics under Irregular Waves

Test 8 was carried out in the LSTF to investigate hydrodynamics induced by irregular waves (Hamilton and Ebersole, 2001). The measurements in Test 8E were used to compare with the present irregular wave model incorporated in the SC. The quantities used in the comparisons include wave heights, mean water levels and wave-induced currents. Both the values averaged over the entire wave-train cycle (**wave-train-averaged** values) and the temporal variations of the **wave-averaged** values (low frequency oscillations) are compared in this study. The wave-train-averaged values used here are the values averaged over the wave-train cycle of 500 seconds. The wave-averaged values (low frequency oscillations) are generated by the averaging procedure described as folows.

4.2.1 Data Processing

The data directly collected in Test 8E were the time series of the instantaneous surface elevations and flow velocity components. The sample rate in the measurement is 20 Hz. These data are then processed in the present study to derive

the wave parameters such as wave heights and wave periods as well as the mean water levels and currents averaged over the wave-train cycle and over wave period.

While the wave-train-averaged values were derived by averaging the measured data over the wave-train cycle of 500 seconds, the Fourier transform technique was used in this study to assist in deriving wave-averaged values from the measurements. The Fourier transform was used to transform the time series of measured data such as water surface elevations and flow velocities into spectra in the frequency domain. A cutoff frequency of 0.1 Hz, corresponding to 10 seconds in period which is 4 times of the peak period of irregular waves, was used to separate the low frequency oscillation from the instantaneous motion. The low frequency components were treated as the wave-averaged components, from which the time series of wave-averaged parameters were derived by using the inverse Fourier transform.

As an example, Figure 4.14 (a) shows the time series of the instantaneous surface elevations measured by the wave gage located at $x = 13.9\,m$ and $y = 13.7\,m$, and the derived time series of wave-averaged mean water levels. While the derived wave-train-averaged mean water level at this location is $0.005\,m$, the wave-averaged mean water levels vary from $-0.019\,m$ to $0.036\,m$. The spectral density of the surface elevations is shown in Fig. 4.14 (b). Although the peak frequency is 0.4 Hz (period of 2.5 seconds), noticeable energy still exists for lower frequency components, implying the existence of the low frequency oscillation of the water levels.

Figure 4.15 presents the time series of the longshore flow velocities measured by the ADV located at $x = 13.9\,m$ and $y = 13.7\,m$ and the derived time series of wave-averaged longshore currents, as well as the spectral density of longshore velocities. The wave-train-averaged longshore current at this location is $0.346\,m/s$, while the wave-averaged longshore currents vary from $0.278\,m/s$ to $0.40\,m/s$. It is noted that the energy for low frequency components is actually larger than that for the peak wave frequency of 0.4 Hz. This is because that the wave particle velocity

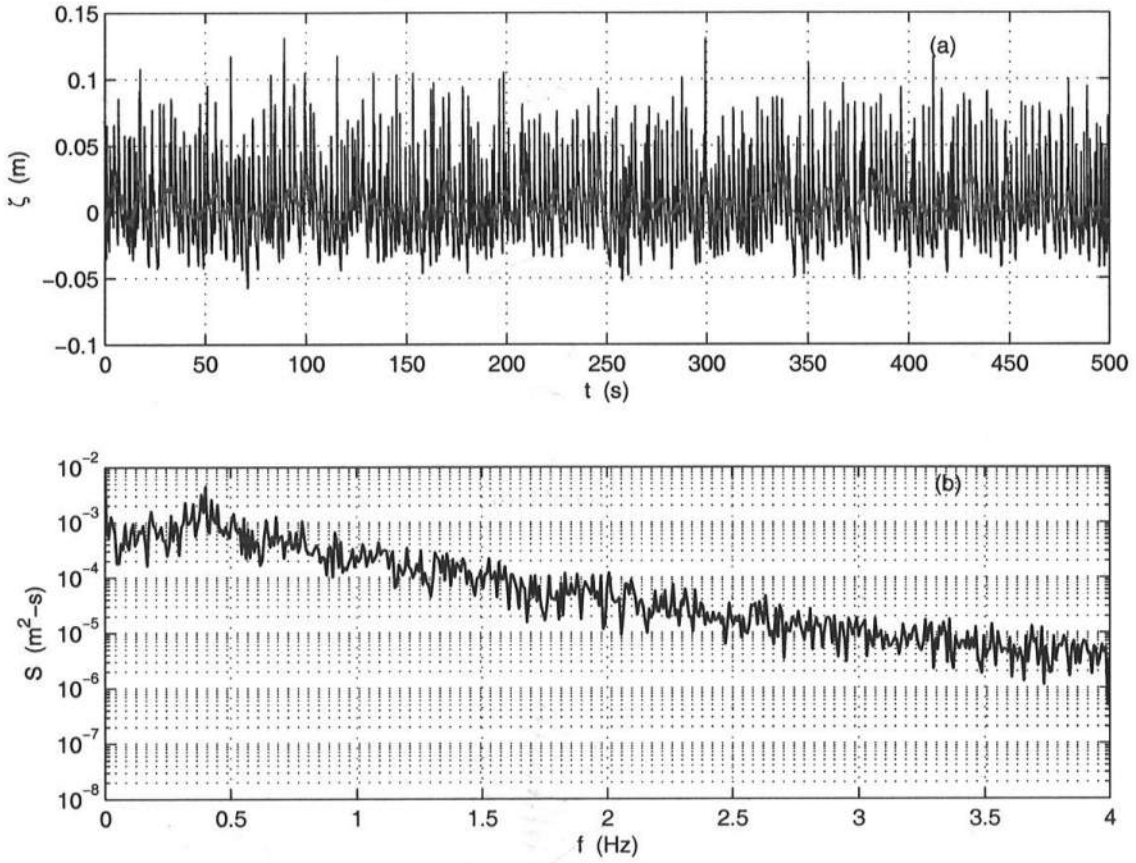

Figure 4.14: (a) Measured instantaneous surface elevations (thin solid line) and the derived temporal variation of wave-averaged mean water levels (thick dash line), and (b) the spectral density of surface elevations at $x = 13.9\,m$, $y = 13.7\,m$ in Test 8E (Hamilton and Ebersole, 2001).

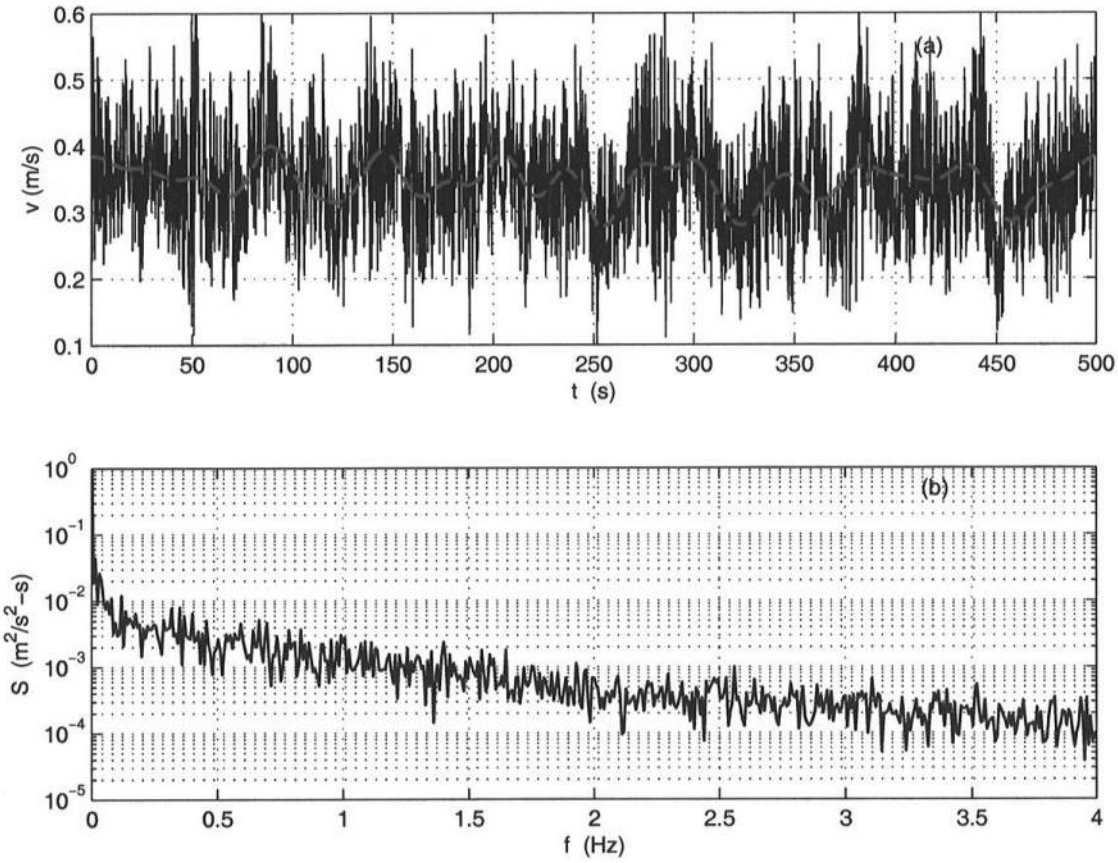

Figure 4.15: (a) Measured longshore flow velocities (thin solid line) and the derived temporal variation of wave-averaged longshore currents (thick dash line), and (b) the spectral density of longshore flow velocities at $x = 13.9\,m$, $y = 13.7\,m$ in Test 8E (Hamilton and Ebersole, 2001).

components in the longshore direction are smaller than the wave-averaged currents (low frequency components) at this location. The wave velocities in the longshore direction are small because the wave angles are small. However, the energy for the peak frequency ($0.4\ Hz$) is comparable to that for low frequency components for the cross-shore flow velocities, as shown in Figure 4.16. This suggests that the wave particle velocities in the cross-shore direction are comparable to the wave-averaged cross-shore currents.

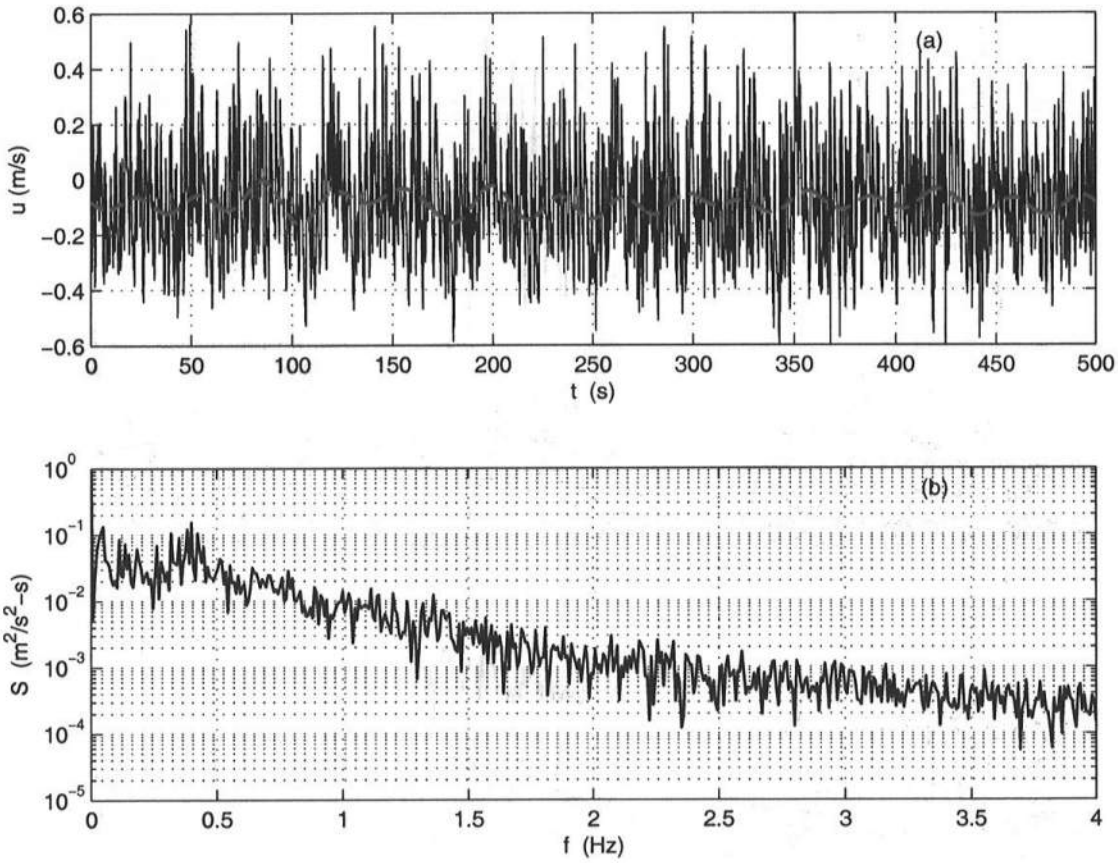

Figure 4.16: (a) Measured cross-shore flow velocities (thin solid line) and the derived temporal variation of wave-averaged cross-shore currents (thick dash line), and (b) the spectral density of cross-shore flow velocities at $x = 13.9\,m$, $y = 13.7\,m$ in Test 8E (Hamilton and Ebersole, 2001).

Wave heights and wave periods were derived in this study using the zero up-crossing method on the time series of the measured surface elevations subtracting the derived (wave-averaged) mean water levels. As an example Figure 4.17 shows the resulting wave heights and periods at $x = 3\,m$, $y = 12.7\,m$. Significant temporal variations can be found for both wave heights and wave periods. These data are therefore further smoothed to obtain the time series of **slowly** varying wave heights and periods, which were finally used as the inputs to the irregular wave model and in

the comparisons with the model prediction. The smoothed wave heights and wave periods at this location are also presented in Figure 4.17.

The smoothing procedure is performed first because the basic assumption of the kinematic wave model requires waves to vary slowly both spatially and temporally. In addition, a milder temporal variation of wave properties helps the model achieve numerical stability. However, by using the smoothing procedure, the random behavior of irregular waves is somewhat restrained and irregular waves are now represented by time variations that resemble wave groups. This may present one of the limitations of the kinematic wave model for irregular waves.

4.2.2 Incident Wave Conditions

The incident wave conditions of the irregular wave model are the time series of wave heights, wave periods and wave angles at the offshore boundary. In the present study the mean position of the wave generators ($x = 0$) was chosen as the offshore (wall) boundary in the SC simulation. Therefore, the wave conditions at $x = 0$ should be used as the incident wave conditions for the irregular wave model. However, the offshore-most wave gages were located 3 meters shoreward from the wave generators. As a result, the derived wave heights and periods at $x = 3\,m$, $y = 12.7\,m$, as showed in Figure 4.17, were used as the incident wave heights and periods at $x = 0$ in the preliminary model simulation. [4] The offshore incident wave angle is 10 degrees.

However, the wave heights at $x = 0$ should be smaller than that at $x = 3\,m$ because of wave shoaling. As a result, the wave heights predicted by the wave model using the wave conditions at $x = 3\,m$ as the incident wave conditions (at $x = 0$) are larger than they should be. Figure 4.18 shows the comparison of wave heights between the measurement and the preliminary model prediction. A general

[4] The obvious remedy of moving the offshore boundary to $x = 3m$ is not viable because it would distort the current patterns relative to the actual basin.

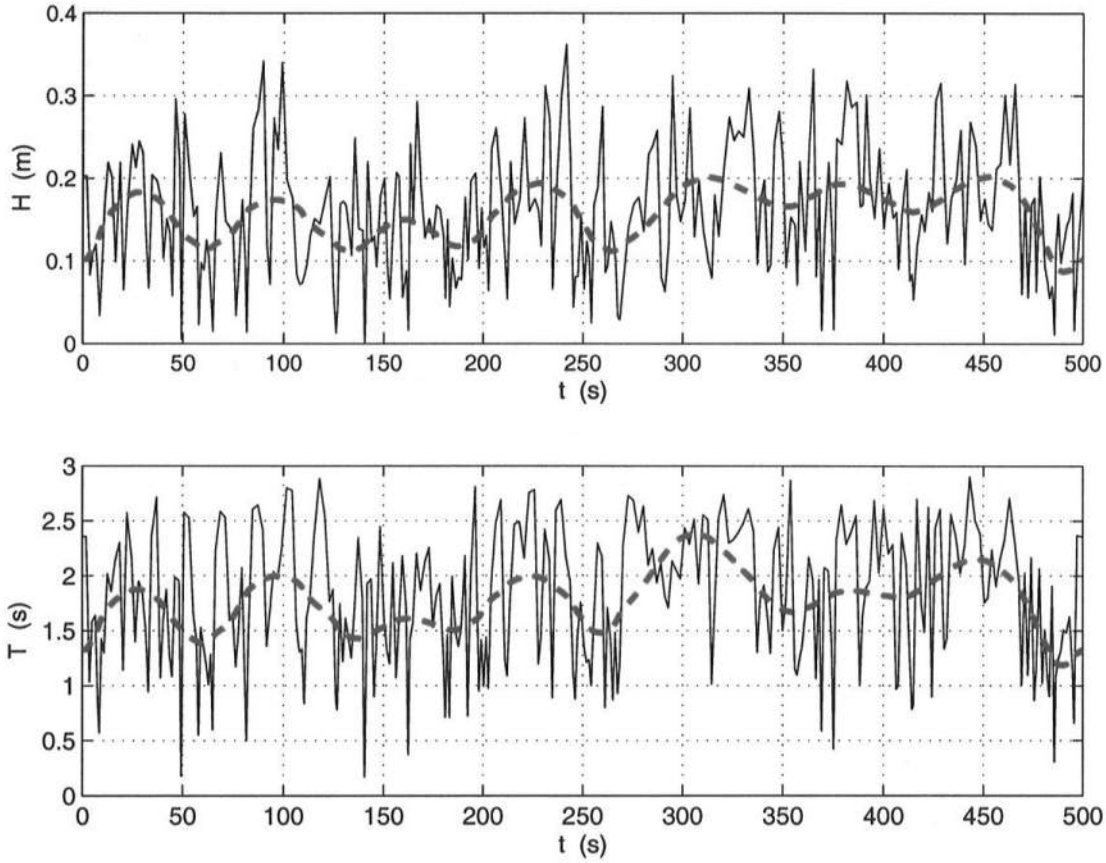

Figure 4.17: Derived temporal variations of wave heights and wave periods at $x = 3\,m$, $y = 12.7\,m$ in Test 8E (Hamilton and Ebersole, 2001). The thin solid lines are the results using the zero up-crossing method, and the thick dash lines are the smoothed results that were also used as the incident wave conditions in the model.

over-prediction of wave heights can be observed, and the wave-train-averaged wave height at $x = 3\,m$ was found to be over-predicted by approximately $0.008\,m$ in the preliminary simulation. Thus, the wave heights at $x = 3\,m$ reduced by $0.008\,m$ were used as the incident wave heights (at $x = 0$) in the subsequent formal simulation. The wave heights at $x = 3\,m$ predicted in the formal simulation is also presented in Figure 4.18 and we see that a much better agreement can be found between the measurements and the formal simulation results.

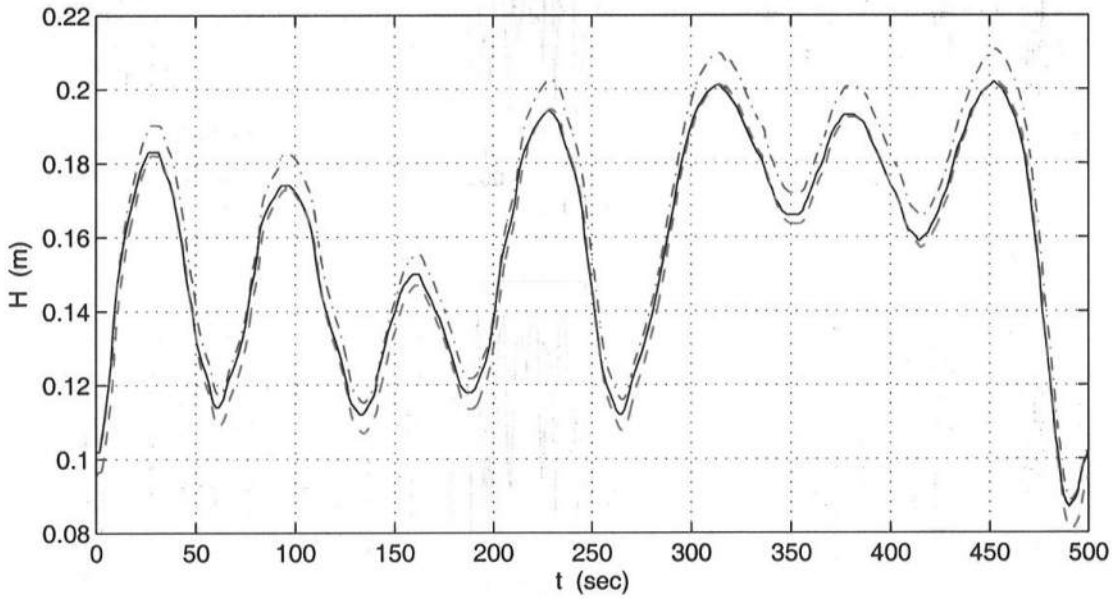

Figure 4.18: Temporal variations of the wave heights at $x = 3\,m$ derived from the measurement (—) in Test 8E (Hamilton and Ebersole, 2001) compared with the model predictions using the wave heights at $x = 3\,m$ without deduction (–·) and with deduction (– –) as the incident wave heights at $x = 0$.

4.2.3 Wave-Train-Averaged Wave Properties and Currents

Figure 4.19 presents the comparison of wave-train-averaged wave heights between the measurements and modeling results at 8 transects. The average breaking point is located at $x = 7.5\,m$. It is seen that the increase in wave height towards

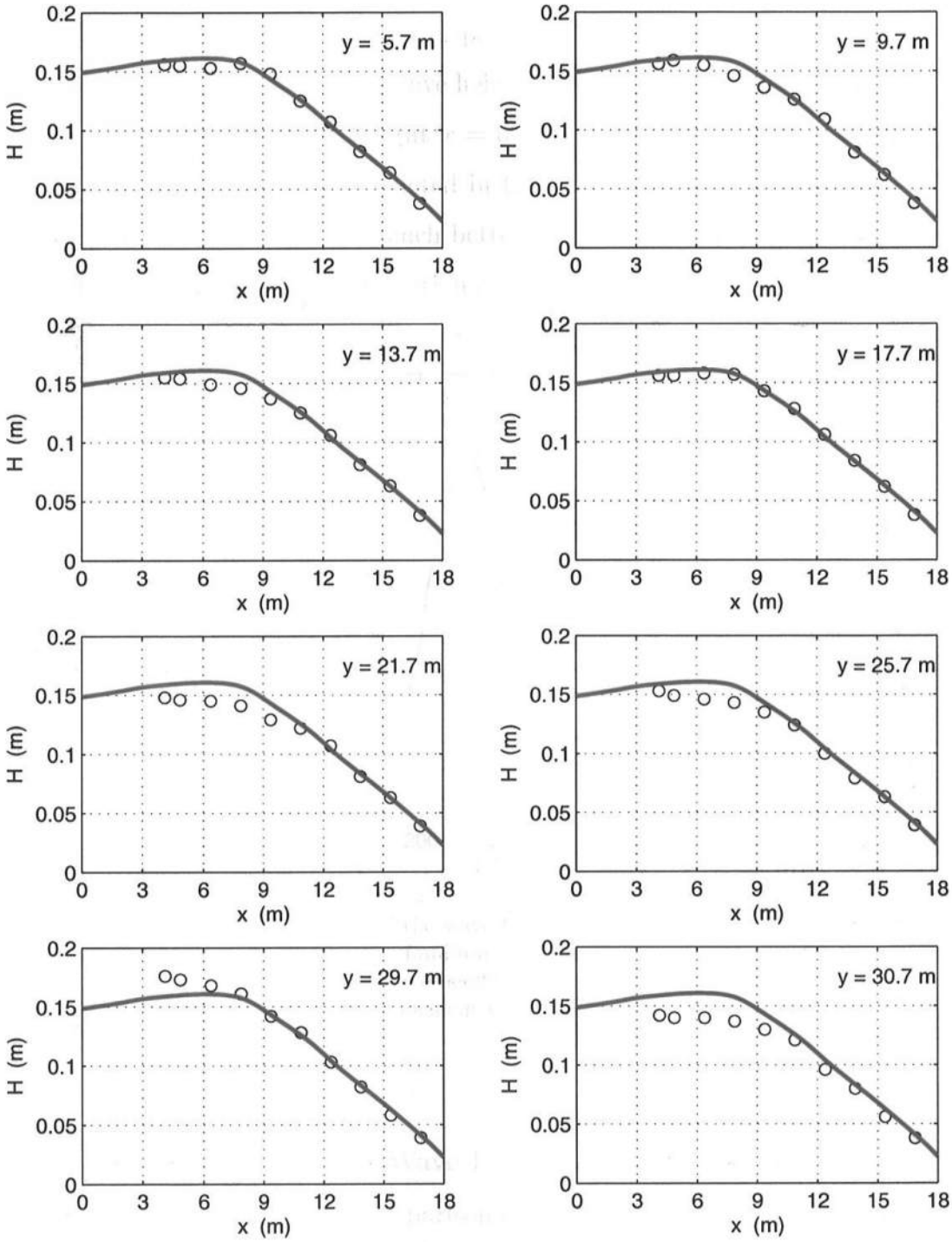

Figure 4.19: Comparisons of the wave-train-averaged wave heights between the experimental data (∘) in Test 8E (Hamilton and Ebersole, 2001) and the prediction using the irregular wave model (—).

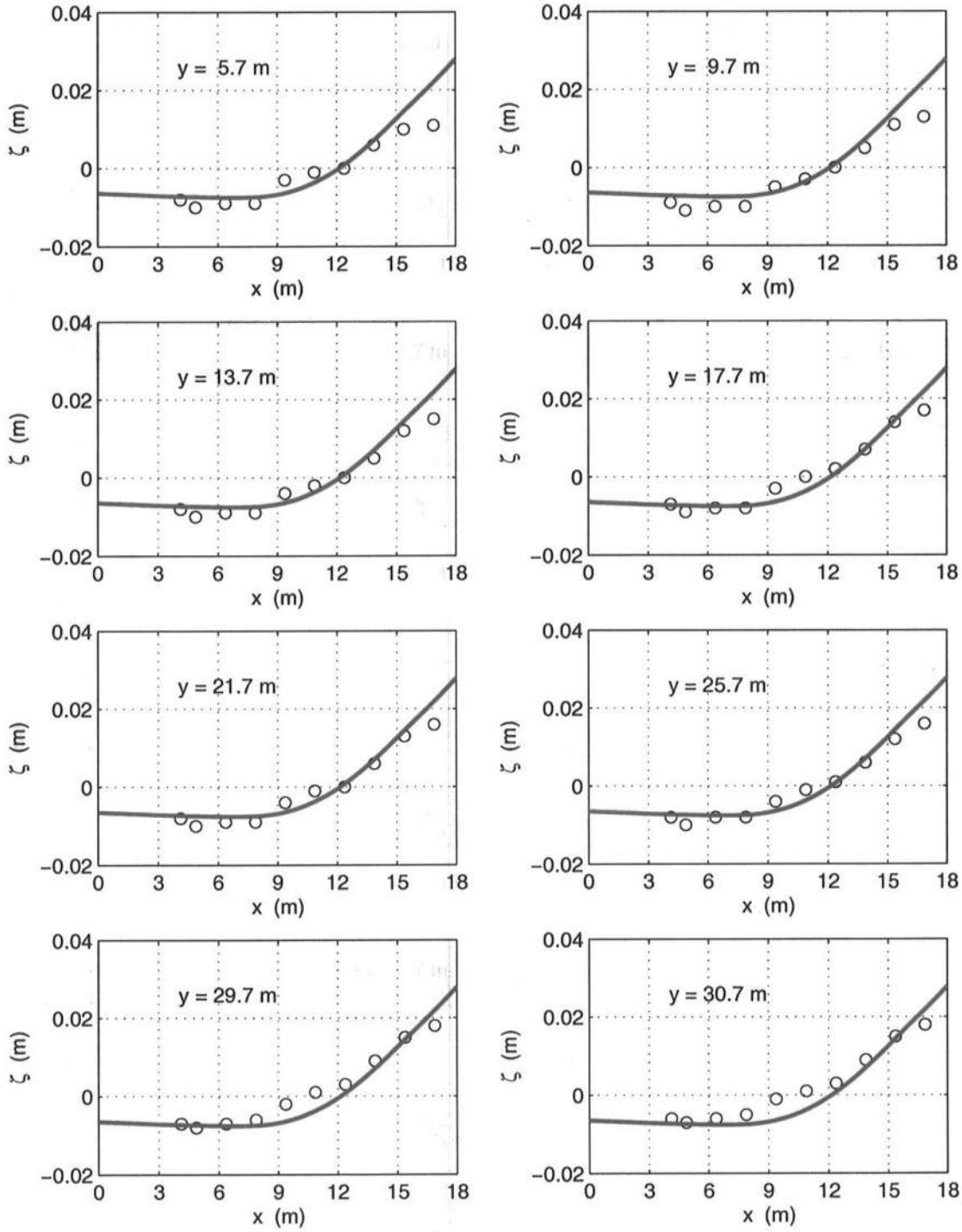

Figure 4.20: Comparisons of the wave-train-averaged mean water levels between the experimental data (∘) in Test 8E (Hamilton and Ebersole, 2001) and the prediction using the SC with the irregular wave driver (—).

(average) breaking for irregular waves is smaller than regular waves (see Fig. 4.1), as illustrated both by the experimental data and by comparisons of the model predictions for two cases. The breaking location changes with time and waves tend to break with smaller H/h because of the interactions among waves. Figure 4.19 also shows that the predicted wave-train-averaged wave heights well agree with the measurements.

A good agreement between the wave-train-averaged mean water levels derived from the experimental data and the model prediction can also be observed, as demonstrated in Figure 4.20. As compared to those in the regular wave test (Figure 4.5 for Test 6N), the setups inside the surfzone seem to be smaller in Test 8E, which is consistent with smaller breaking wave heights.

Figure 4.21 shows the wave-train-averaged quantities of the depth-averaged longshore currents in Test 8E compared with modeling results using the SC with the irregular wave driver. The depth-averaged longshore currents are again represented by those measured at one third of the local water depth above the bed in the experiment. A good agreement between the measurements and the model prediction can be found again for most of transects except the one close to the upstream boundary. Small reverse currents were found in the offshore region in the measurement. However, no reverse longshore currents occur in the modeling results because of the periodic bi-lateral boundary conditions used in the SC simulation for Test 8E.

The wave-train-averaged current vectors measured at the elevation of one third of the water depth above the bed as well as the computed results at that depth are presented in Figure 4.22. The SC with the irregular wave driver predicts the currents reasonably well both in magnitudes and in directions.

Figure 4.23 shows the comparisons of the vertical profiles of wave-train-averaged longshore currents and Fig. 4.24 shows the profiles of cross-shore undertow currents. The trend of the vertical variations of currents induced by irregular waves

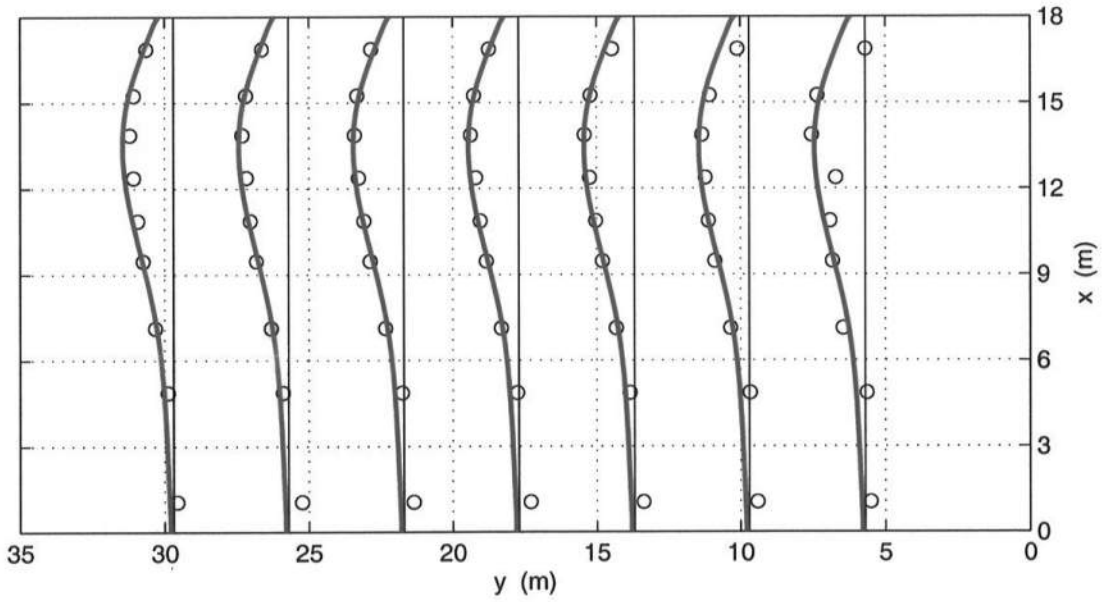

Figure 4.21: Comparisons of the wave-train-averaged longshore currents between the experimental data (∘) in Test 8E (Hamilton and Ebersole, 2001) and the prediction using the SC with the irregular wave driver (—).

are similar to those induced by regular waves (see Figs. 4.11 and 4.12), and the SC with the irregular wave driver is very capable of predicting the vertical profiles of currents induced by irregular waves.

4.2.4 Temporal Variations of Wave-Averaged Wave Properties and Currents

In addition to the wave-train-averaged quantities, it is interesting to further explore the model's capability of predicting the temporal variations of wave properties and wave-averaged currents induced by irregular waves. The temporally varying wave heights, wave-averaged mean water levels and longshore currents derived from the data measured at transect of $y = 13.7\,m$ were used in the comparisons. Transect of $y = 13.7\,m$ was selected because it is the one closest to the location ($x = 3\,m$,

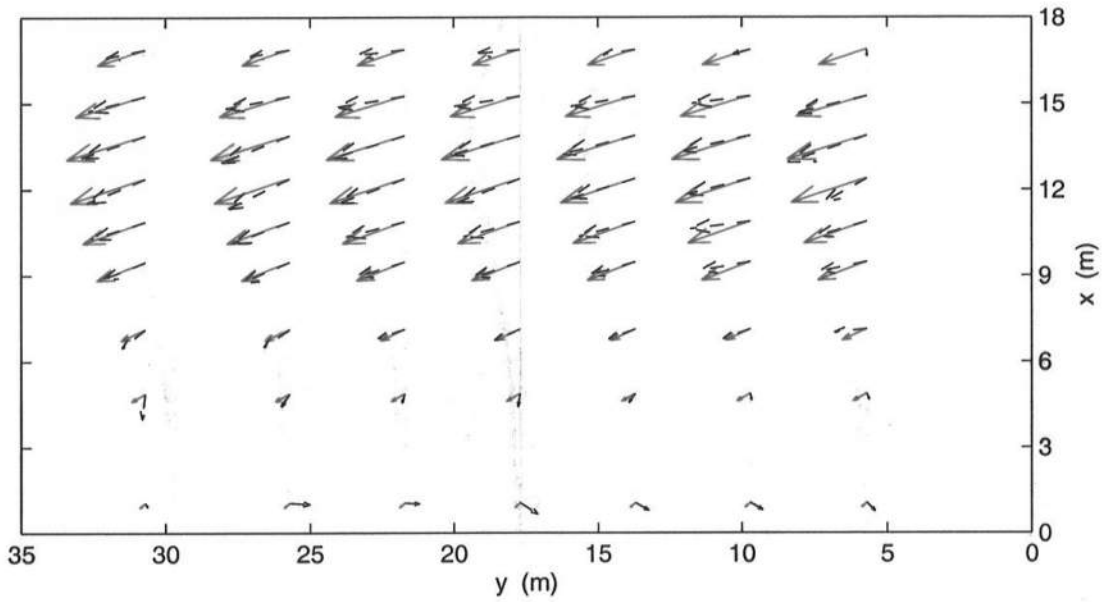

Figure 4.22: Comparisons of the wave-train-averaged currents at 1/3h above the bed between the experimental data ($-\rightarrow$) in Test 8E (Hamilton and Ebersole, 2001) and the prediction using the SC with the irregular wave driver ($\longrightarrow$).

$y = 12.7\,m$) where the measured data were used to derive the incident wave conditions for the irregular wave model.

Figure 4.25 presents the comparisons of the temporal variations of wave heights at $x = 4.9,\ 7.9,\ 10.9,\ 13.9\ m$ in the transect of $y = 13.7\,m$. It is seen that the temporal variations of wave heights become smaller as waves propagate shoreward, as illustrated both in the experimental data and in the modeling results. The irregular wave model appears to predict the temporal variations of wave heights reasonably well, particularly for the region far from breaking (as e.g., at $x = 4.9\,m$ and at $x = 13.9\,m$).

However, there are some measured wave heights that are not fully represented by the model. The worst prediction is found at $x = 7.9\,m$ where the averaged wave breaking is located. A significant discrepancy can be found at $x = 7.9\,m$ from $t = 360$ to 430 second between the measurement and the model prediction, while

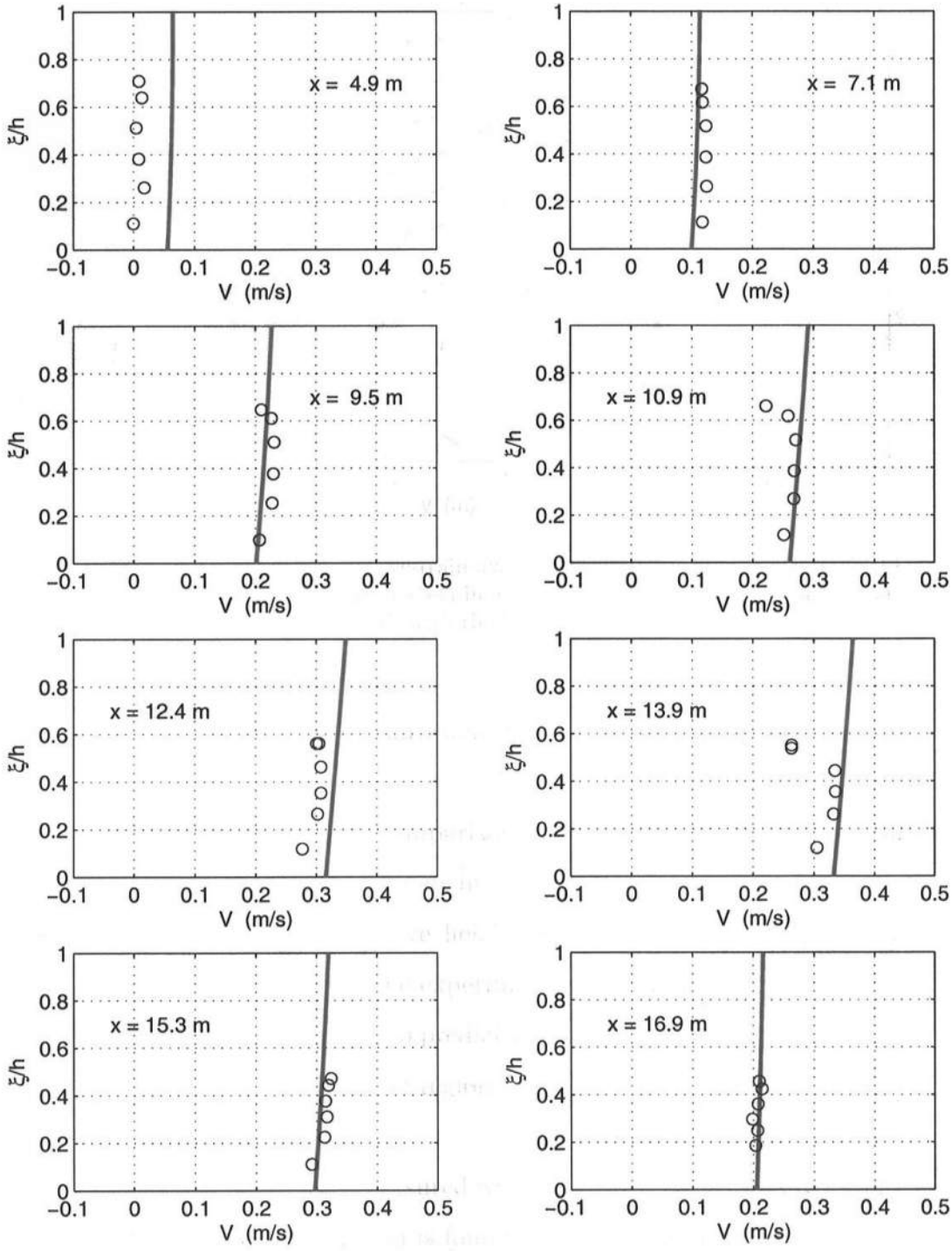

Figure 4.23: Vertical profiles of the wave-train-averaged longshore currents from the experimental data (∘) in Test 8E (Hamilton and Ebersole, 2001) compared with the prediction using the SC with the irregular wave driver (—).

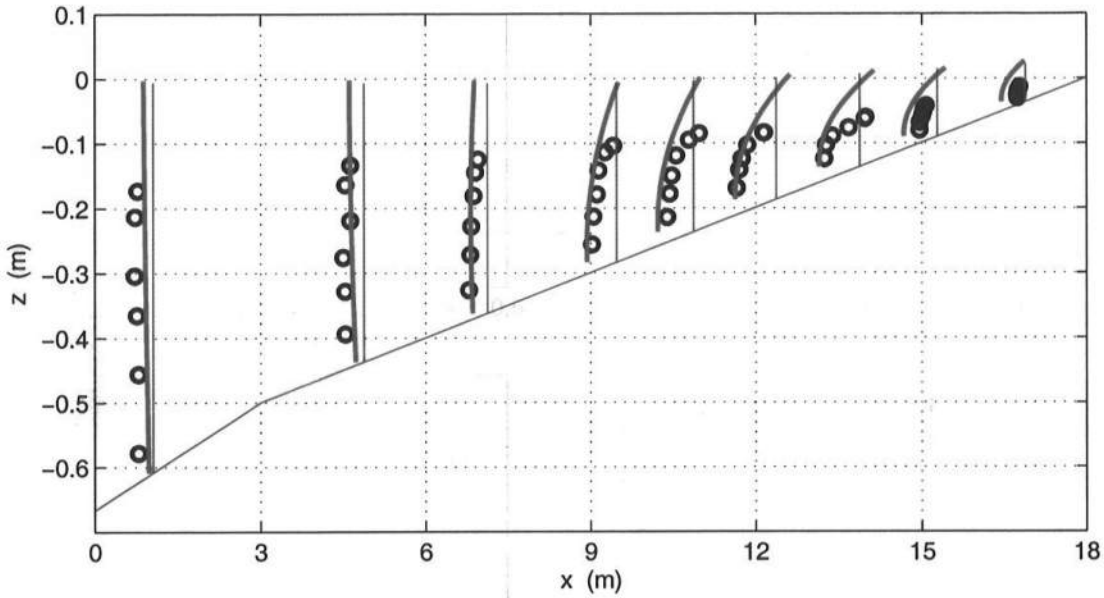

Figure 4.24: Vertical profiles of the wave-train-averaged cross-shore currents from the experimental data (∘) in Test 8E (Hamilton and Ebersole, 2001) compared with the prediction using the SC with the irregular wave driver (—).

the model well predicts the wave height at $x = 4.9\,m$ for the same period of time. On the other hand, a under-prediction of wave height from $t = 150$ to 180 second occurs both at $x = 7.9\,m$ and at $x = 4.9\,m$. The discrepancy in the temporal variation of wave heights seems to be caused by the criterion of wave breaking we used, which may not work for all the individual waves within the irregular wave group. However, such suspicion has not been confirmed yet.

Figure 4.26 shows the temporal variations of the wave-averaged mean water levels derived from the experimental data compared with the prediction using the SC with the irregular wave model. Significant temporal variations of (wave-averaged) mean water levels are found in the experiment data. The SC with the irregular wave model is capable of predicting the trend of the temporal variations of mean water levels. However, the magnitudes of the temporal variations are under-predicted by the model.

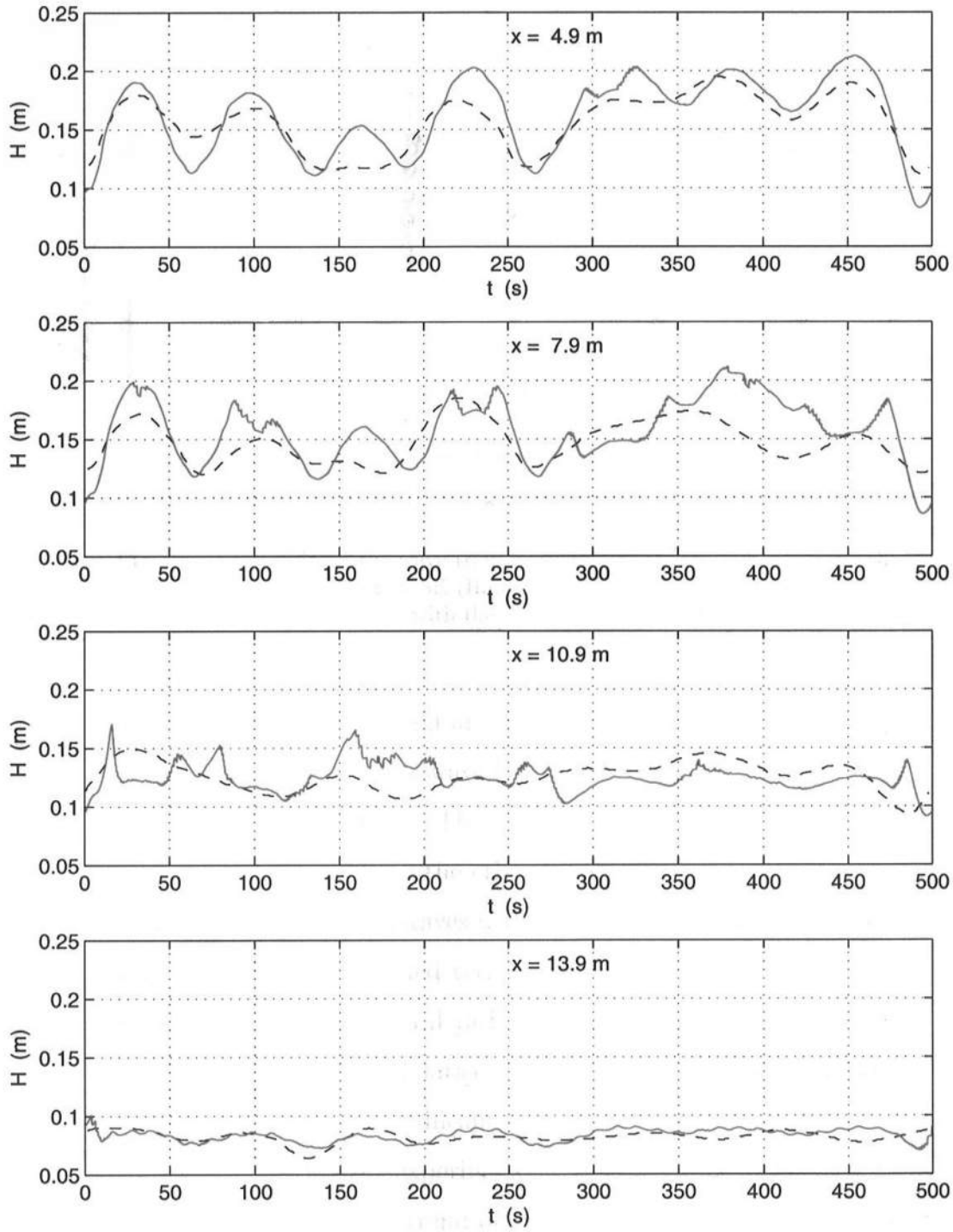

Figure 4.25: Comparisons of the temporal variations of wave heights (H) between the experimental data (−−) in Test 8E (Hamilton and Ebersole, 2001) and the irregular wave model (—).

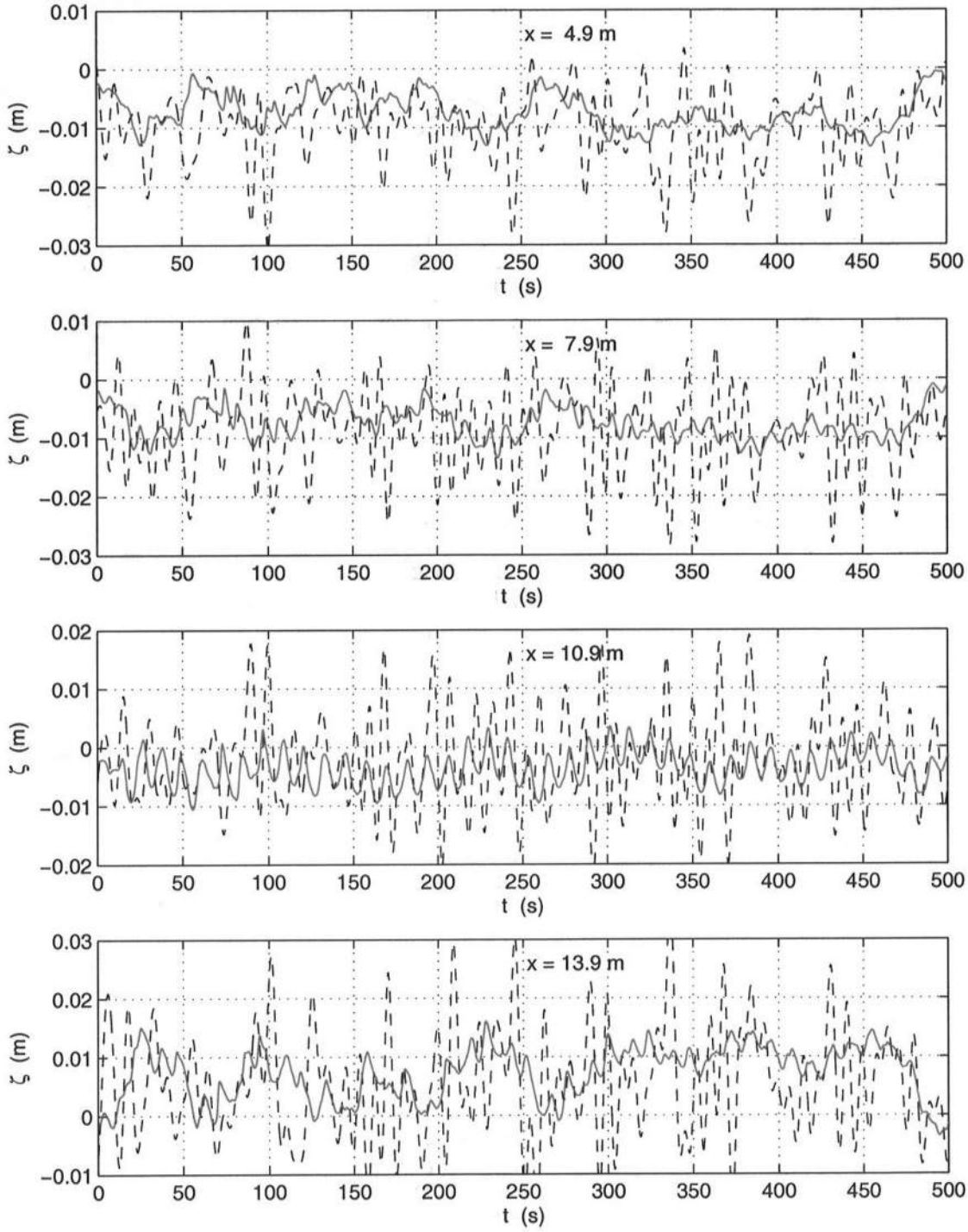

Figure 4.26: Comparisons of the temporal variations of mean water levels ($\bar{\zeta}$) between the experimental data (−−) in Test 8E (Hamilton and Ebersole, 2001) and the prediction using the SC with the irregular wave driver (—).

The temporally varying longshore currents derived from the experimental data as well as the model prediction are shown in Figure 4.27. While considerable temporal variations are found in the experiment, the SC with the irregular wave driver is only capable of predicting the general variations instead of the detailed magnitudes.

Because of the complicated features of the hydrodynamics induced by irregular waves, modeling nearshore circulation induced by irregular waves still presents a great challenge for coastal researchers. The comparisons of the temporal variations of wave heights and circulation between the experimental data and model prediction, as presented in this section, are not yet found in the literature. The present kinematic-type irregular wave model coupled with the SC demonstrates a general capability of predicting nearshore hydrodynamics under irregular wave environments. It is capable of accurately predicting the wave heights, mean water levels and wave-induced circulation averaged over wave-train cycle, and it also has a limited capability of predicting temporal variations of these quantities averaged over wave period. The limitation of the model appears to be its under-prediction of the magnitudes of the temporal variations of mean water levels and currents.

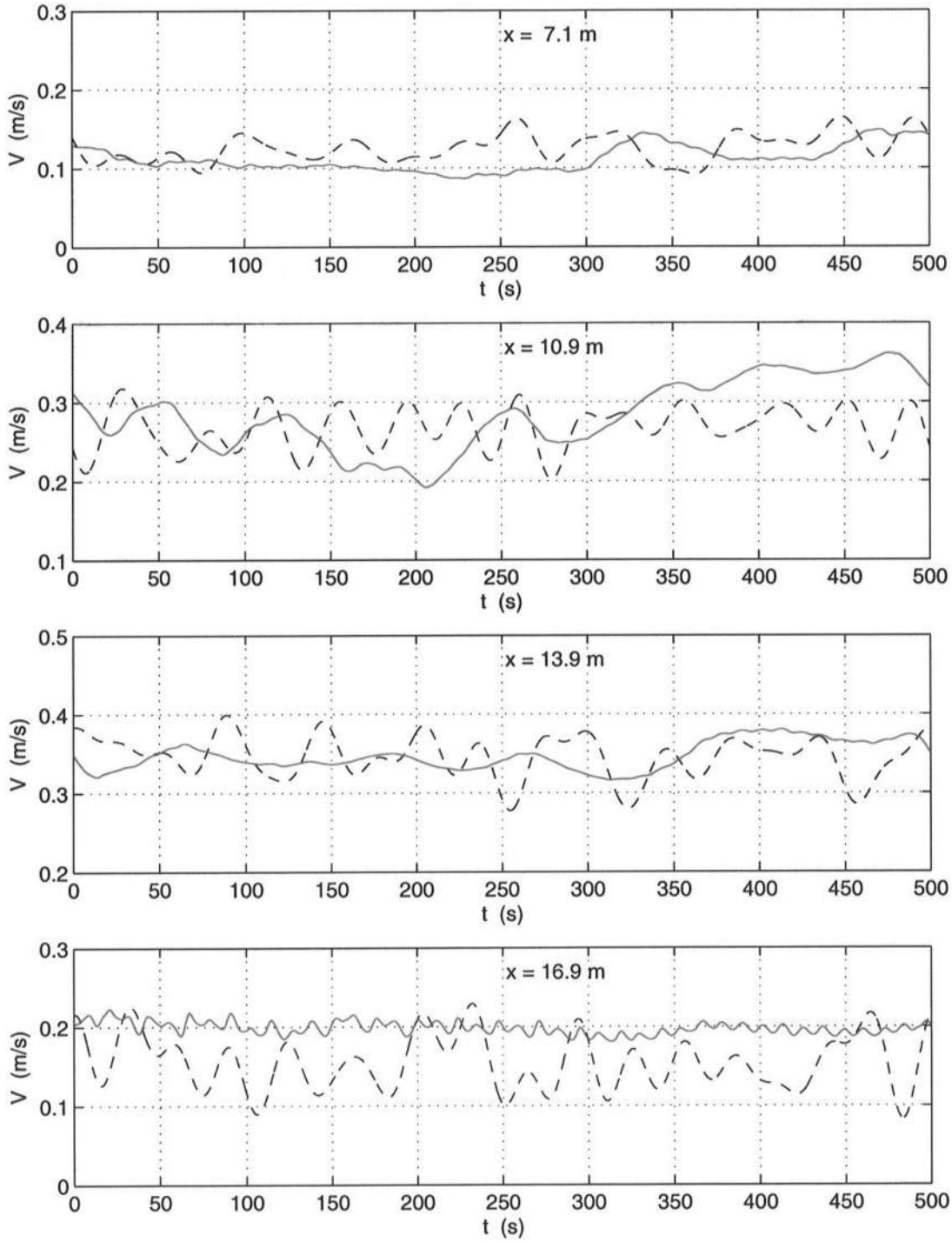

Figure 4.27: Comparisons of the temporal variations of the wave-averaged longshore currents (V) between the experimental data (−−) in Test 8E (Hamilton and Ebersole, 2001) and the SC with the irregular wave driver (—).

Chapter 5

THEORETICAL BACKGROUND OF THE NEARSHORE SEDIMENT TRANSPORT MODEL

The classic approach for investigating nearshore sediment transport is to split the sediment transport into the bedload mode and the suspended load mode, and the sediment transport rate is calculated as the sum of the bedload and the suspended load. This method is theoretically and numerically simple and has already been extensively applied to real engineering problems.

Alternative approach called the two-phase flow modeling has also been presented recently (as e.g., Drew (1983), Kobayashi and Seo (1985), Asano (1990), Li and Sawamoto (1995), Dong and Zhang (1999), Hsu *et al.* (2003)). The advantage of this approach lies in the fact that the mass and momentum equations for the fluid phase and the sediment phase are solved directly and it is not necessary to separate the bedload from the suspended load. However, the limited accuracy caused by the theoretical uncertainties of the main forces as well as the computational complexity and inefficiency make the two-phase flow model far from being applied to conditions as complex as modeling nearshore sediment transport.

The present study follows the classic approach to separate the sediment into the bedload and the suspended load. A formula was derived for the bedload transport rate starting from the two-phase flow theory, and two approaches were developed for the suspended sediment transport: One is to modify the Bailard (1981b)

formula to include the effect of wave breaking, and the other is to develop a detailed physics-based phase-resolving diffusion-convection model.

5.1 Introduction to the Two-Phase Flow Theory

5.1.1 Governing Equations

For the sediment transport in unsteady turbulent flows, the continuity and momentum equations for the fluid phase and the sediment phase can be written as follows (Kobayashi and Seo (1985), Asano (1990), Li and Sawamoto (1995), Dong and Zhang (1999)):

The continuity equations are

$$\text{Fluid:} \qquad \frac{\partial}{\partial t}\rho(1-c) + \frac{\partial}{\partial x_j}\rho(1-c)u_j = 0 \tag{5.1}$$

$$\text{Sediment:} \qquad \frac{\partial}{\partial t}\rho_s c + \frac{\partial}{\partial x_j}\rho_s c u_{sj} = 0 \tag{5.2}$$

where $x_i (i = 1, 2, 3)$ and t denote the Cartesian coordinate system and time, respectively, ρ and ρ_s are densities of the fluid and the sediment, both of which are usually assumed to be constant. c is the volumetric sediment concentration, u_j and u_{sj} are instantaneous x_j-components of the velocities of the fluid and the sediment, respectively. The concentration c and velocity components u_j and u_{sj} are functions of space (x_1, x_2, x_3) and time (t)

The momentum equations are

$$\text{Fluid:} \qquad \frac{\partial}{\partial t}\rho(1-c)u_i + \frac{\partial}{\partial x_j}\rho(1-c)u_i u_j = \rho(1-c)g_i - \frac{\partial p}{\partial x_i} - f_i \tag{5.3}$$

$$\text{Sediment:} \qquad \frac{\partial}{\partial t}\rho_s c u_{si} + \frac{\partial}{\partial x_j}\rho_s c u_{si} u_{sj} = \rho_s c g_i + f_i + \frac{\partial T_{sji}}{\partial x_j} \tag{5.4}$$

where g_i is the x_i-component of the gravitational acceleration, p is the total fluid pressure, f_i is the x_i-component of the interaction forces per unit volume between the sediment and the fluid including the effect of the pressure acting on the sediment phase, and T_{sji} is the component of the intergranular stress tensor.

For the analysis of the two-phase flow at the turbulent regime, the instantaneous quantities can be expressed as the sum of (turbulent) mean and fluctuating quantities by Reynolds decomposition:

$$u = \overline{u_i} + u_i'; \quad u_{si} = \overline{u_{si}} + u_{si}'; \quad c = \overline{c} + c'; \quad p = \overline{p} + p'$$

where the bar $^-$ denotes mean quantities and the prime $'$ denotes fluctuating quantities. Substituting these expressions into (5.1) to (5.4) yields:

$$\text{Fluid:} \quad \frac{\partial}{\partial t}\rho(1-\overline{c}) + \frac{\partial}{\partial x_j}\rho(1-\overline{c})\overline{u_j} = \frac{\partial}{\partial x_j}\rho\overline{c'u_j'} \tag{5.5}$$

$$\text{Sediment:} \quad \frac{\partial}{\partial t}\rho_s\overline{c} + \frac{\partial}{\partial x_j}\rho_s\overline{c}\,\overline{u_{sj}} = -\frac{\partial}{\partial x_j}\rho_s\overline{c'u_{sj}'} \tag{5.6}$$

$$\begin{aligned}\text{Fluid:} \quad & \frac{\partial}{\partial t}\rho[(1-\overline{c})\overline{u_i} - \overline{c'u_i'}] + \frac{\partial}{\partial x_j}\rho(1-\overline{c})\overline{u_i}\,\overline{u_j} \\ & = \rho(1-\overline{c})g_i - \frac{\partial p}{\partial x_i} - f_i + \frac{\partial \tau_{ji}}{\partial x_j}\end{aligned} \tag{5.7}$$

$$\text{Sediment:} \quad \frac{\partial}{\partial t}\rho_s[\overline{c}\,\overline{u_{si}} + \overline{c'u_{si}'}] + \frac{\partial}{\partial x_j}\rho_s\overline{c}\,\overline{u_{si}}\,\overline{u_{sj}} = \rho_s\overline{c}g_i + f_i + \frac{\partial T_{sji}}{\partial x_j} + \frac{\partial \tau_{sji}}{\partial x_j} \tag{5.8}$$

where τ_{ji} is the Reynolds turbulent stress of the fluid phase, and τ_{sji} is the turbulent stress of the sediment phase. The τ_{ji} is defined as the terms

$$\tau_{ji} = -\rho\,[\,(1-\overline{c})\,\overline{u_i'u_j'} - \overline{u_i}\,\overline{c'u_j'} - \overline{u_j}\,\overline{c'u_i'} - \overline{c'u_i'u_j'}\,] \tag{5.9}$$

and τ_{sji} as

$$\tau_{sji} = -\rho_s\,[\,\overline{c}\,\overline{u_{si}'u_{sj}'} + \overline{u_{si}}\,\overline{c'u_{sj}'} + \overline{u_{sj}}\,\overline{c'u_{si}'} + \overline{c'u_{si}'u_{sj}'}\,] \tag{5.10}$$

5.1.2 Major Forces

The most important as well as the most difficult part of the two-phase flow theory is to evaluate the forces and to provide closures for the turbulent stresses in terms of the primary flow and sediment parameters. For simplicity, the bar $^-$ which denotes turbulent mean quantities is omitted hereafter.

Interaction Forces

The interaction forces between the flow and the sediment can be expressed as the sum of the drag force, the lift force, the added mass inertial force and the pressure force.

A grain experiences a drag force F_{Di} and a lift force F_{Li} when a relative velocity occurs between the fluid and the grain. The drag force results from the form drag and skin friction as the fluid flows around the grain. The lift force is caused by the curvature of local streamlines in the flow over the top of it. The drag force is typically given by:

$$F_{Di} = \frac{\rho}{2} C_D A \left| u_{ri} \right| u_{ri} \tag{5.11}$$

where A is the cross sectional area of the grain facing the flow and $A = \pi d^2/4$ for a spherical particle, C_D is the drag coefficient, and u_{ri} is the relative velocity between the flow and the sediment, i.e., $u_{ri} = u_i - u_{si}$. While there are a few formulations for the lift force for a vertical 2D case, no detailed investigation or generalized formulation for the lift force has been found. In addition, the lift force is believed to be small as compared to the drag force. Thus, the lift force is neglected in the present study, as done by Kobayashi and Seo (1985) and by Asano (1990).

The added inertial force F_{Ai} on a grain in an accelerated flow arises from the acceleration of some fluid mass with it. The added inertial force is typically formulated as

$$F_{Ai} = C_m \rho V \frac{du_{ri}}{dt} \tag{5.12}$$

where V is the volume of the grain and $V = \pi d^3/6$ for a spherical particle, and C_m is the added mass coefficient which depends on the particle shape and on the proximity to the boundary. For a spherical particle far from other particles $C_m = 0.5$.

The net pressure force F_{Pi} experienced by a grain results from the spatial gradient of the flow pressure around it.

$$F_{Pi} = -V \frac{\partial p}{\partial x_i} \tag{5.13}$$

The vertical component of F_P is the familiar buoyancy force $\rho g V$ if a hydrostatic pressure is assumed. The pressure gradient in the flow direction is zero for uniform steady flows, while it is nonzero for oscillatory flows because of the hydrodynamic pressure.

The forces discussed above are experienced by one grain, and the number of grains per unit (mixture) volume is c/V. Therefore, the interaction force per unit volume is

$$f_i = \frac{c}{V}\left(F_{Di} + F_{Li} + F_{Ai} + F_{Pi}\right) \tag{5.14}$$

It is worthy of mention that while the pressure force on a grain is directly included in the governing equations in Asano (1990), Li and Sawamoto (1995) and Dong and Zhang (1999), it is treated as part of the interaction force in this study and in Kobayashi and Seo (1985).

Intergranular Stress

Collisions and continuous contacts among grains in granular flows generate intergranular forces both in the normal and in the tangential directions, which are referred to as the dispersive stress and the granular shear stress, respectively. Bagnold (1954, 1966) first studied the intergranular stresses in granular flows and expressed them as functions of the shear rate of the sediment motion du_s/dz and of the linear sediment concentration λ that is related to the volumetric concentration c as follows

$$\lambda = \frac{(c/c_0)^{1/3}}{1-(c/c_0)^{1/3}} \tag{5.15}$$

where c_0 is the maximum concentration generally assumed to be 0.65. It is noted that λ increases drastically as c approaches c_0.

Bagnold considered two different regimes in which different types of interactions dominate the behavior of the fluid-grain-mixture. For large, dense particles at high shear rates the interactions are dominated by particle collisions. This is

referred as the inertial regime. For small and light grains in very viscous fluid the interactions are dominated by viscosity. Bagnold termed this the macro-viscous regime. Bagnold also defined a dimensionless parameter

$$B = \frac{s\, d^2 \sqrt{\lambda}\, \frac{du_s}{dz}}{\nu} \tag{5.16}$$

to separate the regimes. Here s is the specific gravity of the grain $s = \rho_s/\rho$, and u_s is the grain velocity component tangential to the bed.

A pure inertial regime was found for $B > 450$, for which Bagnold suggested

$$\sigma_G = \frac{\tau_G}{\tan\varphi_d} = \frac{1}{25}\rho s\,(\lambda d\,\frac{du_s}{dz})^2 \tag{5.17}$$

where σ_G is the granular dispersive stress, τ_G is the granular shear stress, and φ_d is the dynamical response angle which was found to be about 18 degrees ($\tan\varphi_d = 0.32$).

A purely macro-viscous regime is found for $B < 40$ and Bagnold suggested

$$\sigma_G = \frac{\tau_G}{\tan\varphi_d} = 1.3\,(1+\lambda)\,(1+\lambda/2)\,\rho\nu\,\frac{du_s}{dz} \tag{5.18}$$

with a somewhat larger dynamical response angle of 37 degrees ($\tan\varphi_d = 0.75$).

With typical values ($s,\ d,\ \lambda,\ du/dz,\ \nu$) = ($2.65,\ 0.2\,mm,\ 1,\ 100\,s^{-1},\ 10^{-6}\,m^2/s$), we get $B = 10.6$. It may be expected that the sheet flow under moderate wave conditions is generally in the macro-viscous regime.

The Bagnold constitutive equation was used by Hanes and Inman (1985), and by Li and Sawamoto (1995). Based on the extensive experiments by Savage and McKeown (1983), Ahilan and Sleath (1987) proposed another simple relationship for the granular stresses

$$\tau_G = \sigma_G \tan\varphi_d = 1.2\lambda^2\rho\nu\,\frac{\partial u_s}{\partial z} \tag{5.19}$$

This relation was used by Ahilan and Sleath (1987), Asano (1990), Ono *et al.* (1996), and Dong and Zhang (1999).

Turbulent Stress

It is noted from Eqs. (5.9) and (5.10) that the turbulent shear stresses in the two-phase flow are much more complex than those in the single-phase flow. The normal turbulent stresses are usually neglected in comparison to the corresponding pressure and gravity terms. We can rewrite Eqs. (5.9) and (5.10) as

$$\tau_{x_\alpha z} = -\rho \left[(1-\bar{c}) \overline{u'_\alpha w'} - u_\alpha \overline{c'w'} - w \overline{c'u'_\alpha} - \overline{c'u'_\alpha w'} \right] \tag{5.20}$$

$$\tau_{sx_\alpha z} = -\rho_s \left[\bar{c} \overline{u'_{s\alpha} w'_s} + u_{s\alpha} \overline{c'w'_s} + w_s \overline{c'u'_{s\alpha}} + \overline{c'u'_{s\alpha} w'_s} \right] \tag{5.21}$$

where subscript α denotes the horizontal directions and $\alpha = 1, 2$ (x, y). After assuming $w \overline{c'u'_\alpha}$ and $\overline{c'u'_\alpha w'}$ are negligible as compared to $u_\alpha \overline{c'w'}$, and $w_s \overline{c'u'_{s\alpha}}$ and $\overline{c'u'_{s\alpha} w'_s}$ are negligible as compared to $u_{s\alpha} \overline{c'w'_s}$, the formulations of turbulent shear stresses reduce to

$$\tau_{x_\alpha z} = -\rho \left[(1-c) \overline{u'_\alpha w'} - u_\alpha \overline{c'w'} \right] \tag{5.22}$$

$$\tau_{sx_\alpha z} = -\rho_s \left[c \overline{u'_{s\alpha} w'_s} + u_{s\alpha} \overline{c'w'_s} \right] \tag{5.23}$$

The classic approach can be introduced to establish the closure for the turbulent terms as

$$\overline{u'_\alpha w'} \approx \overline{u'_{s\alpha} w'_s} = -\epsilon_z \frac{\partial u_\alpha}{\partial z} \tag{5.24}$$

$$\overline{c'w'} \approx \overline{c'w'_s} = -\epsilon_{sz} \frac{\partial c}{\partial z} \tag{5.25}$$

where ϵ_z is the vertical turbulent eddy viscosity and ϵ_{sz} is the vertical sediment diffusion coefficient.

5.1.3 Discussion

Although the two-phase flow model directly solves the continuity and momentum equations for the fluid phase and the sediment phase, several uncertainties still remain in the dominant force terms in the governing equations: The formulations of granular stresses are based on a few simple experiments; the evaluation of

interaction forces depends on several parameters such as drag and lift coefficients that are uncertain for sheet flows; the effect of sediment on flow turbulent shear stresses is also unresolved.

In addition, the two-phase flow model involves highly non-linear and coupled equations. Thus, the numerical calculation procedure was found to be very complex and time-consuming. As a result, the two-phase flow model has so far been limited to modeling sediment transport in the uniform, small scale, linear and purely oscillatory or steady sheet flows. It is far from the practical application in modeling the nearshore sediment transport, which the present study aims at. However, we will use the essential idea of the two-phase flow theory in the present model formulations.

5.2 Derivation of Formula for Bedload Transport Rate from the Two-Phase Flow Theory

The instantaneous bedload transport rate for oscillatory flows is usually determined as **a formula for steady flows**. To take advantages of both the theoretical integrity of the two-phase flow theory and the simple structure of classic bedload formulas, a formula for the bedload transport rate is re-derived in this study starting with the momentum equations for the two-phase flow. After assuming quasi-steady situation and neglecting small terms, a simplified formula for the bedload transport rate is obtained. This formula has a similar structure to the classic formulas such as Engelund and Fredsøe (1976), and Bailard and Inman (1981a) but is a theoretical improvement of those formulas.

The beach slope in practice is very small, and $\tan\beta \approx \sin\beta \leq 1$ where β is the bottom slope. Hence, a locally plane beach with a small bottom slope in the cross-shore direction is assumed in this study, as also done by Bailard and Inman (1981a), and by Fredsøe *et al.* (1985). By assuming a small bottom slope higher order terms of $O(\tan\beta)^2$ can be neglected for mathematical simplicity.

Following Bailard and Inman (1981a), the local coordinate system is chosen so that the positive x is the onshore direction, the positive y is the downstream longshore direction, z is the upward direction normal to the bed and $z = 0$ at the local bottom, as shown in Figure 5.1. By choosing (x, y) tangential to the local bottom, the bedload moves parallel to the (x, y) plane with bottom flows. It has been found that the bedload transport only occurs within a very thin layer close to the bed, and the thickness of the bedload layer l_B is very small as compared to the water depth.

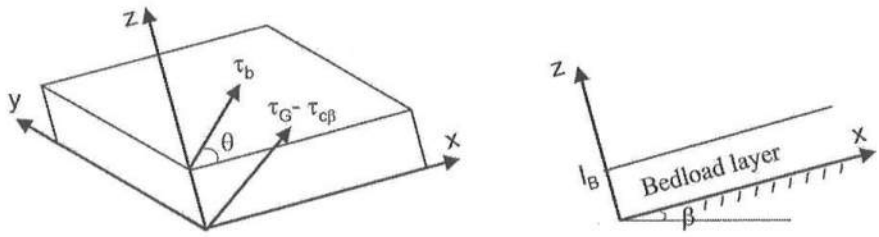

Figure 5.1: Schematic diagram of the coordinate system for bedload transport

5.2.1 Simplified Momentum Equations for Quasi-Steady Flows

Adding (5.7) and (5.8), we obtain the momentum equation for the combined fluid-grain flow

$$\frac{\partial}{\partial t}\{\rho(1-c)u_i + \rho_s c u_{si} - \rho\overline{c'u_i'} + \rho_s\overline{c'u_{si}'}\} + \frac{\partial}{\partial x_j}\{\rho(1-c)u_i u_j + \rho_s c u_{si}u_{sj}\}$$
$$= \{\rho(1-c) + \rho_s c\}g_i - \frac{\partial p}{\partial x_i} + \frac{\partial}{\partial x_j}(T_{ji}) \tag{5.26}$$

where T_{ji} is the stress of the combined flow consisting of the intergranular stress T_{sji} and the turbulent stress τ_{ji}' including contributions from both the fluid phase

τ_{ji} and the sediment phase τ_{sji}, i.e.,

$$T_{ji} = \tau'_{ji} + T_{sji} \qquad \text{with} \qquad \tau'_{ji} = \tau_{ji} + \tau_{sji} \tag{5.27}$$

For a quasi-steady situation, the local acceleration $\partial/\partial t = 0$, and the pressure may be assumed to become locally the hydrostatic pressure which satisfies

$$\frac{\partial p}{\partial x_i} = \rho g_i \tag{5.28}$$

For a plane beach with a bottom slope in the cross-shore direction

$$g_i = (\ -g\sin\beta,\ 0,\ -g\cos\beta\ ) \tag{5.29}$$

If we further assume a locally uniform situation, $\partial/\partial x,\ \partial/\partial y \ll \partial/\partial z$, and neglect the velocities in the vertical direction ($w \approx 0,\ w_s \approx 0$), the momentum equation (5.26) reduces to

$$(\rho_s - \rho)cg_i + \frac{\partial T_{zi}}{\partial z} = 0 \tag{5.30}$$

After plugging in (5.29) for g_i, this equation can be rewritten as separate equations in the x, y and z directions

$$x: \qquad -(\rho_s - \rho)cg\sin\beta + \frac{\partial T_{zx}}{\partial z} = 0 \tag{5.31}$$

$$y: \qquad 0 + \frac{\partial T_{zy}}{\partial z} = 0 \tag{5.32}$$

$$z: \qquad -(\rho_s - \rho)cg\cos\beta + \frac{\partial T_{zz}}{\partial z} = 0 \tag{5.33}$$

5.2.2 Boundary Conditions for the Bedload Layer

At the top of the bedload layer ($z = l_B$), it is reasonable to assume the intergranular stress is much less than the turbulent stress, i.e., $T_{sji} \ll \tau'_{ji}$. Thus,

$$T_{ji} \approx \tau'_{ji} \qquad \text{at } z = l_B \tag{5.34}$$

The normal turbulent stress is typically negligible as compared to the pressure and gravity components in that direction. Therefore, T_{ij} can be also be written as

$$x: \qquad T_{zx}|_{z=l_B} = \tau'_{zx}|_{z=l_B} = \tau_0 \cos\theta \tag{5.35}$$

$$y: \qquad T_{zy}|_{z=l_B} = \tau'_{zy}|_{z=l_B} = \tau_0 \sin\theta \tag{5.36}$$

$$z: \qquad T_{zz}|_{z=l_B} = \tau'_{zz}|_{z=l_B} \approx 0 \tag{5.37}$$

where θ is the angle between the turbulent stress shear and the x direction, as shown in Fig. 5.1, and τ_0 is the turbulent shear stress at the top of the bedload layer. Here, τ_0 is actually equivalent to the bottom shear stress $|\vec{\tau}_b|$, which is expressed as the common quadratic form (neglecting the effect of the sediment phase on the flow turbulence)

$$\vec{\tau}_b = \frac{1}{2}\rho f |\vec{u}|\,\vec{u} \tag{5.38}$$

Here, $\vec{u}$ is the bottom flow velocity for open channel flows and is the velocity above the wave boundary layer for oscillatory flows. Hence,

$$\tau_0 = |\vec{\tau}_b| = \frac{1}{2}\rho f |\vec{u}|^2 \qquad \text{and} \qquad \vec{\tau}_b/\tau_0 = \vec{u}/|\vec{u}| \tag{5.39}$$

At the bottom of the bedload layer ($z = 0$) it is expected that the total (combined) flow stresses in the normal direction are dominated by the granular dispersive stress, and the interganular shear stress is much larger than the flow turbulent shear stress when an intense bedload transport occurs. However, the flow turbulent shear stress becomes as significant as the granular shear stress for weak bedload transport, and thus it is included in the present study. The total stresses for the combined flow at the bottom of the bedload layer can now be approximated by

$$\text{x-y plane:} \qquad |\vec{T}_0| \equiv \sqrt{T_{zx}^2|_{z=0} + T_{zy}^2|_{z=0}} = \tau_G + \tau'' \tag{5.40}$$

$$\text{z:} \qquad T_{zz}|_{z=0} = -\sigma_G \tag{5.41}$$

in which τ'' is the residual flow shear stress, τ_G is the granular shear stress and σ_G is the granular dispersive stress at the bottom of the bedload layer, and

$$\tau_G \equiv \sqrt{T_{szx}^2|_{z=0} + T_{szy}^2|_{z=0}} \tag{5.42}$$

$$\sigma_G \equiv -T_{szz}|_{z=0} \tag{5.43}$$

The similar boundary conditions for bedload transport were also used in Bailard and Inman (1981a). The difference is that the residual flow shear stress is now included in this study while it was neglected in Bailard and Inman (1981a). It will be illustrated later that the final formula for the bedload transport rate become theoretically more elegant and realistically more reasonable by including the residual flow shear stress.

The volumetric bedload transport rate is defined as

$$\vec{q}_B = \int_0^{l_B} c\vec{u}_B \, dz \tag{5.44}$$

where $\vec{u}_B$ is the local bedload transport velocity and c is the (bedload) sediment concentration, both of which are functions of the vertical location z. For simplicity Eq. (5.44) is typically rewritten as

$$\vec{q}_B = \vec{U}_B \int_0^{l_B} c \, dz \tag{5.45}$$

where $\vec{U}_B$ is a representative bedload transport velocity which is now independent of z. We focus on the second formulation in this study. The values of $\int_0^{l_B} c\,dz$ and $\vec{U}_B$ are determined separately as follows before the formula for $\vec{q}_B$ is finally derived.

5.2.3 Determination of $\int_0^{l_B} c\,dz$

Integrating Eqs. (5.31), (5.32) and (5.33) separately over the bedload layer ($0 \le z \le l_B$), and applying (5.35), (5.36) and (5.37) for the corresponding boundary conditions at $z = l_B$, we have

$$\text{x:} \qquad T_{zx}|_{z=0} = \tau_0 \cos\theta - \tau_g \tag{5.46}$$

$$\text{y:} \qquad T_{zy}|_{z=0} = \tau_0 \sin\theta \tag{5.47}$$

$$\text{z:} \qquad T_{zz}|_{z=0} = -(\rho_s - \rho) g \cos\beta \int_0^{l_B} c\, dz \tag{5.48}$$

where τ_g is the x component of the effective gravity of the bedload layer

$$\tau_g = (\rho_s - \rho) g \sin\beta \int_0^{l_B} c\, dz \tag{5.49}$$

The magnitude of the combined flow shear stress at the bottom thus becomes

$$|\vec{T_0}| \equiv \sqrt{T_{zx}^2|_{z=0} + T_{zy}^2|_{z=0}} = \tau_0 \sqrt{1 - 2\cos\theta \frac{\tau_g}{\tau_0} + (\frac{\tau_g}{\tau_0})^2} \tag{5.50}$$

After neglecting higher order terms of $O(\tan\beta)^2$ or $O(\sin\beta)^2$ for a small bottom slope, we obtain

$$|\vec{T_0}| \approx \tau_0 - \tau_g \cos\theta \tag{5.51}$$

Combining (5.51) and (5.40) for a boundary condition at $z = 0$ yields

$$\tau_G = \tau_0 - \tau_g \cos\theta - \tau'' \tag{5.52}$$

and combining (5.48) and (5.41) for the other boundary condition at $z = 0$ gives

$$\sigma_G = (\rho_s - \rho) g \cos\beta \int_0^{l_B} c\, dz \tag{5.53}$$

According to the granular flow theory $\tau_G = \tan\phi_d\, \sigma_G$ and thus

$$\tau_G = \tan\phi_d\, (\rho_s - \rho) g \cos\beta \int_0^{l_B} c\, dz \tag{5.54}$$

After rewriting (5.52) as

$$\tau_0 = \tau_G + \tau_g \cos\theta + \tau'' \tag{5.55}$$

it can be found that the total bottom flow shear stress balances the granular shear stress, the tangential component of the bedload weight and the residual shear stress as well. The bedload transport only occurs when the flow shear stress τ_0 exceeds

τ''. Hence, the residual shear stress τ'' is actually **the threshold shear stress** for sediment movement and (5.55) can be written as

$$\tau_0 = \tau_G + \tau_g \cos\theta + \tau_{c\beta} \tag{5.56}$$

where $\tau_{c\beta}$ is the threshold shear stress at a sloping bottom. For a horizontal bottom, $\tau_g = 0$ and

$$\tau_0 = \tau_G + \tau_{c0} \tag{5.57}$$

where τ_{c0} is the threshold shear stress at the bottom.

The threshold shear stress $\tau_{c\beta}$ was not included in Bagnold (1956, 1963, 1966) and in Bailard and Inman (1981a), and thus bedload transport occurs as long as there is a flow shear stress. The threshold shear stress for a horizontal bottom was included and (5.57) was used in Engelund and Fredsøe (1976). In the modified version of Engelund and Fredsøe (1976) formula for the sloping bottom (as e.g., Andersen, 1999), Eq.(5.57) was still used just with τ_{c0} replaced with $\tau_{c\beta}$ instead of using (5.56).

Inserting (5.49) for τ_g and (5.54) for τ_G into (5.56) and rearranging terms, we have

$$\int_0^{l_B} c\, dz = \frac{\tau_0(1 - \tau_{c\beta}/\tau_0)}{(\rho_s - \rho) g \tan\phi_d \cos\beta} \frac{1}{1 + \frac{\tan\beta}{\tan\phi_d} cos\theta} \tag{5.58}$$

After neglecting higher order terms of $O(\tan\beta)^2$, we obtain

$$\int_0^{l_B} c\, dz = \frac{\tau_0(1 - \tau_{c\beta}/\tau_0)}{(\rho_s - \rho) g \tan\phi_d \cos\beta} \left(1 - \frac{\tan\beta}{\tan\phi_d} cos\theta\right) \tag{5.59}$$

5.2.4 Representative Bedload Velocity

After obtaining $\int_0^{l_B} c\, dz$, we need to determine the representative bedload velocity $\vec{U}_B$ in order to obtain the bedload transport rate according to (5.45). While $\int_0^{l_B} c\, dz$ is derived starting from the momentum equation for the combined flow, $\vec{U}_B$ will be derived starting from the momentum equation for the sediment phase.

Magnitude of $\vec{U}_B$

After we neglect the turbulent stress for the sediment phase, and again assume a quasi-steady and locally uniform situation, the momentum equation for the sediment phase (5.8) reduces to

$$\rho_s c g_i + f_i + \frac{\partial T_{szi}}{\partial z} = 0 \tag{5.60}$$

If only the leading terms such as the drag force and the net pressure force are included for the interaction forces, i.e.,

$$f_i = \frac{c}{V}\left(F_{Di} + F_{Pi}\right) = F_{Di}\frac{c}{V} - \rho c g_i \tag{5.61}$$

Eq. (5.60) becomes

$$(\rho_s - \rho) c g_i + F_{Di}\frac{c}{V} + \frac{\partial T_{szi}}{\partial z} = 0 \tag{5.62}$$

We denote the drag force

$$F_{Di} = F_D(\cos\theta_1,\ \sin\theta_1) \tag{5.63}$$

where θ_1 is the angle between the drag force (or relative velocity) and the x axis and F_D is the magnitude of the drag force. Therefore,

$$F_D = \frac{\rho}{2} C_D A\,|\vec{u_r}|^2 \tag{5.64}$$

Substituting (5.29) for g_i, Eq. (5.62) can be written as

$$\text{x:} \qquad -(\rho_s - \rho) g \sin\beta\, c + F_D \cos\theta_1 \frac{c}{V} + \frac{\partial T_{szx}}{\partial z} = 0 \tag{5.65}$$

$$\text{y:} \qquad F_D \sin\theta_1 \frac{c}{V} + \frac{\partial T_{szy}}{\partial z} = 0 \tag{5.66}$$

$$\text{z:} \qquad -(\rho_s - \rho) g \cos\beta\, c + \frac{\partial T_{szz}}{\partial z} = 0 \tag{5.67}$$

Neglecting the vertical variations of u_r and θ_1, integrating (5.65) and (5.66), respectively, over the bedload layer and applying the boundary condition at the top of the bedload layer (i.e., negligible granular stresses at $z = l_B$), we have

$$T_{szx}|_{z=0} = nF_D \cos\theta_1 - \tau_g \tag{5.68}$$

$$T_{szy}|_{z=0} = nF_D \sin\theta_1 \tag{5.69}$$

in which n is the number of bedload grains per unit bed area

$$n = \int_0^{l_B} c\, dz \,/\, V \tag{5.70}$$

Therefore, the magnitude of the granular shear stress at the bottom becomes

$$\tau_G \equiv \sqrt{T_{szx}^2|_{z=0} + T_{szy}^2|_{z=0}} = nF_D\sqrt{1 - 2\cos\theta_1 \frac{\tau_g}{nF_D} + (\frac{\tau_g}{nF_D})^2} \tag{5.71}$$

It is noted that $\tau_g = O(\tan\beta)$. After neglecting higher order terms of $O(\tan\beta)^2$ in Eq. (5.71), we have

$$\tau_G \approx nF_D - \tau_g \cos\theta_1 \tag{5.72}$$

It is reasonable to assume the bedload moves in the same direction as the flow does, and $\cos\theta_1 = \vec{i} \cdot \vec{U}_B / |\vec{U}_B|$ in which $\vec{i}$ is the unit vector in the x direction. It can be shown later from (5.92) that

$$\cos\theta_1 \approx \vec{i} \cdot \vec{u}/|\vec{u}| + O(\tan\beta) = \cos\theta + O(\tan\beta) \tag{5.73}$$

After neglecting higher order terms of $O(\tan\beta)^2$, (5.72) finally reduces to

$$\tau_G \approx nF_D - \tau_g \cos\theta \tag{5.74}$$

Inserting (5.74) for τ_G into (5.56) and rearranging terms, we have

$$\tau_0 - \tau_{c\beta} = nF_D \tag{5.75}$$

from which it can be noted that the effective flow shear stress generates the drag force for sediment. For a horizontal bottom $\tau_g = 0$, $\tau_G = nF_D = \tau_0 - \tau_{c\beta}$. In another

word, the effective flow shear stress generates the drag force for sediment to balance the granular shear stress. This relation was also used by Engelund and Fredsøe (1976).

Inserting (5.49) for τ_g, (5.54) for τ_G, (5.64) for F_D, and (5.70) for n into (5.74), we obtain

$$\tan\phi(\rho_s-\rho)g\cos\beta=\frac{3}{4d}\rho c_D|\vec{u}_r|^2-(\rho_s-\rho)g\sin\beta\cos\theta \tag{5.76}$$

for a spherical grain ($A=\pi d^2/4$ and $V=\pi d^3/6$). From this we can further obtain

$$|\vec{u}_r|^2=(s-1)gd\frac{4\tan\phi_d}{3C_D}\cos\beta\,(\,1+\frac{\tan\beta}{\tan\phi_d}\cos\theta\,) \tag{5.77}$$

We denote $\vec{u}_{z_0}$ the representative flow velocity at the bedload layer, where z_0 is the elevation above the bottom. After assuming bedload moves at the same direction as the flow does, we have

$$|\vec{u}_r|=|\vec{u}_{z_0}|-|\vec{U}_B| \tag{5.78}$$

According to the logarithmic velocity distribution for fully rough turbulent flows

$$|\vec{u}(z)|=\frac{U_*}{\kappa}\ln\frac{z}{k_s/30} \tag{5.79}$$

in which U_* is the shear velocity $U_*\equiv\sqrt{\tau_0/\rho}$, $\kappa\approx 0.4$ is the von Kármán constant, k_s is the bottom roughness. If we express $|\vec{u}_{z_0}|$ as

$$|\vec{u}_{z_0}|=e_cU_* \tag{5.80}$$

it can be found that

$$e_c=\frac{1}{\kappa}\ln(\frac{z_0}{k_s/30}) \tag{5.81}$$

If we assume the representative elevation $z_0=2d$ and the bottom roughness $k_s=2d$, it can be found that $e_c=8.5$.

After substituting (5.77) for $|\vec{u}_r|$ and (5.80) for $|\vec{u}_{z_0}|$ into (5.78), we obtain the magnitude of the bedload transport velocity

$$|\vec{U}_B| = e_c U_* \left\{ 1 - \sqrt{\frac{g(s-1)d}{U_*^2} \frac{4\tan\phi_d}{3C_D e_c^2} \cos\beta \left(1 + \frac{\tan\beta}{\tan\phi_d} \cos\theta \right)} \right\} \tag{5.82}$$

The Shields parameter is defined as

$$\psi \equiv \frac{\tau_0}{\rho g(s-1)gd} = \frac{U_*^2}{g(s-1)d} \tag{5.83}$$

Denoting

$$\psi_{c\beta} \equiv \frac{4\tan\phi_d}{3C_D e_c^2} \cos\beta \left(1 + \frac{\tan\beta}{\tan\phi_d} \cos\theta \right) \tag{5.84}$$

Eq. (5.82) can be written as

$$|\vec{U}_B| = e_c U_* \{ 1 - \sqrt{\psi_{c\beta}/\psi} \} \tag{5.85}$$

from which it can be found that $\psi_{c\beta}$ is actually *the critical Shields parameter* and the bedload transport only occurs when $\psi \geq \psi_{c\beta}$

For a horizontal bottom, $\psi_{c0} = \frac{4\tan\phi_d}{3C_D e_c^2}$. If we assume $\tan\phi_d = 0.75$, $e_c = 8.5$ and $c_D = 0.4$, it is found that $\psi_c \approx 0.05$. We can also link the critical shear stress to the critical Shields parameter by $\tau_{c\beta} = \psi_{c\beta}\, \rho g(s-1)gd$, and rewrite (5.85) as

$$|\vec{U}_B| = e_c U_* \{ 1 - \sqrt{\tau_{c\beta}/\tau_0} \} \tag{5.86}$$

Direction of $\vec{U}_B$

As discussed by Bailard and Inman (1981a), the bedload grains are concentrated in the lower portion of the moving layer. For mathematical simplicity the direction of the representative bedload velocity can be approximated by the direction of the mixture flow shear stress at the bottom, i.e.,

$$\frac{\vec{U}_B}{|\vec{U}_B|} = \frac{\vec{i}\, T_{zx}|_{z=0} + \vec{j}\, T_{zy}|_{z=0}}{|\vec{T}_0|} \tag{5.87}$$

After substituting (5.46) for $T_{zx}|_{z=0}$, (5.47) for $T_{zx}|_{z=0}$ and (5.51) for $|\vec{T}_0|$, we have

$$\frac{\vec{U}_B}{|\vec{U}_B|} = \frac{\vec{i}\cos\theta + \vec{j}\sin\theta - \vec{i}\frac{\tau_g}{\tau_0}}{1 - \frac{\tau_g}{\tau_0}\cos\theta} = \frac{\frac{\vec{u}}{|\vec{u}|} - \vec{i}\frac{\tau_g}{\tau_0}}{1 - \frac{\tau_g}{\tau_0}\cos\theta} \tag{5.88}$$

Comparing (5.54) with (5.49) it is found that

$$\tau_G = \tau_g \tan\phi_d / \tan\beta \tag{5.89}$$

Using this to replace τ_G in (5.56) and rearranging terms yields

$$\frac{\tau_g}{\tau_0} = \frac{1 - \tau_{c\beta}/\tau_0}{\frac{\tan\phi_d}{\tan\beta} + \cos\theta} = (1 - \frac{\tau_{c\beta}}{\tau_0})\{\frac{\tan\beta}{\tan\phi_d} + O(\tan\beta)^2\} \tag{5.90}$$

After neglecting higher order terms of $O(\tan\beta)^2$, this equation reduce to

$$\frac{\tau_g}{\tau_0} \approx (1 - \frac{\tau_{c\beta}}{\tau_0})\frac{\tan\beta}{\tan\phi_d} \tag{5.91}$$

Substituting τ_g/τ_0 into (5.88) with (5.91) and neglecting high order terms of $O(\tan\beta)^2$, we have

$$\frac{\vec{U}_B}{|\vec{U}_B|} \approx \frac{\vec{u}}{|\vec{u}|}(1 + (1 - \frac{\tau_{c\beta}}{\tau_0})\frac{\tan\beta}{\tan\phi_d}\cos\theta) - \vec{i}(1 - \frac{\tau_{c\beta}}{\tau_0})\frac{\tan\beta}{\tan\phi_d} \tag{5.92}$$

It is noted that if the critical shear stress is neglected the direction of the bedload velocity is the same as that in Bailard and Inman (1981a).

5.2.5 Formula for the Bedload Transport Rate

After substituting (5.59) for $\int_0^{l_B} c\,dz$, (5.86) and (5.92 for $\vec{U}_B$ into (5.45), and neglecting higher order terms of $O(\tan\beta)^2$, the formula for the bedload transport rate vector now reads

$$\begin{aligned}\vec{q}_B = {} & \frac{1}{(\rho_s - \rho)g\cos\beta}\frac{\tau_0\, e_c U_*}{\tan\phi_d}\left(1 - \sqrt{\frac{\tau_{c\beta}}{\tau_0}}\right)\left(1 - \frac{\tau_{c\beta}}{\tau_0}\right) \\ & \left\{\frac{\vec{u}}{|\vec{u}|}\left(1 - \frac{\tau_{c\beta}}{\tau_0}\frac{\tan\beta}{\tan\phi_d}\cos\theta\right) - \vec{i}\left(1 - \frac{\tau_{c\beta}}{\tau_0}\right)\frac{\tan\beta}{\tan\phi_d}\right\}\end{aligned} \tag{5.93}$$

Bailard and Inman (1981a) defined the bedload efficiency coefficient ϵ_B as

$$\epsilon_B = \frac{\int_0^{l_B} c|\vec{u}_B|\,dz}{|\vec{u}|\int_0^{l_B} c\,dz} \tag{5.94}$$

which is equivalent to

$$\epsilon_B = \frac{|\vec{U}_B|}{|\vec{u}|} \tag{5.95}$$

in the present study. Substituting $|\vec{U}_B|$ with (5.85), we obtain

$$\epsilon_B = \frac{e_c U_*}{|\vec{u}|}\left(1 - \sqrt{\frac{\psi_{c\beta}}{\psi}}\right) \tag{5.96}$$

and (5.93) can be rewritten as

$$\begin{aligned}\vec{q}_B &= \frac{1}{(\rho_s-\rho)g\cos\beta}\,\frac{\epsilon_B\tau_b|\vec{u}|}{\tan\phi_d}\left(1-\frac{\tau_{c\beta}}{\tau_b}\right)\\ &\left\{\frac{\vec{u}}{|\vec{u}|}\left(1-\frac{\tau_{c\beta}}{\tau_0}\,\frac{\tan\beta}{\tan\phi}\cos\theta\right) - \vec{i}\left(1-\frac{\tau_{c\beta}}{\tau_0}\right)\frac{\tan\beta}{\tan\phi}\right\}\end{aligned} \tag{5.97}$$

As compared to Bailard and Inman (1981a), the effect of the threshold shear stress for sediment movement is included in (5.97). As (5.97) shows, the bedload transport rate is not a continuous function of the bottom shear stress, and the bedload transport only occurs (i.e., $|\vec{q}_B| > 0$) when the bottom shear stress exceeds the threshold shear stress $\tau_{c\beta}$. This is more realistic than Bailard and Inman (1981a).

5.2.6 Discussion of the Bedload Efficiency Coefficient

If open channel flows are fully rough turbulent flows, (5.79) for the logarithmic velocity profile applies for the whole water depth and the corresponding depth-averaged velocity is

$$\bar{U} \equiv \frac{1}{h}\int_{k_s/30}^{h} |\vec{u}(z)|dz \;=\; \frac{U_*}{\kappa}\ln\frac{30h}{e\,k_s} \tag{5.98}$$

Since the depth-averaged velocity is used in the expression of the bottom friction τ_0 for open channel flows, $|\vec{u}|$ in (5.96) is now represented by $\bar{U}$, and the bedload efficiency coefficient for open channel flows becomes

$$\epsilon_B = \frac{e_c\kappa}{\ln\frac{30h}{ek_s}}\left(1-\sqrt{\frac{\psi_{c\beta}}{\psi}}\right) \tag{5.99}$$

For turbulent flows in the wave boundary layer (WBL) of oscillatory flows, we assume the vertical profile of the (quasi-steady) velocity in the WBL to satisfy (5.79) as well. Therefore, the velocity at the top of the WBL ($z = \delta_w$ with δ_w the thickness of the WBL) is

$$|\vec{u}_b| = \frac{U_*}{\kappa} \ln \frac{30\delta_w}{k_s} \tag{5.100}$$

The velocity $\vec{u}_b$, however, is always used in the expression of the bottom friction τ_0 for oscillatory flows. Thus, $|\vec{u}|$ in (5.96) is represented by $|\vec{u}_b|$, and the bedload efficiency coefficient for oscillatory flows becomes

$$\epsilon_B = \frac{e_c \kappa}{\ln \frac{30\delta_w}{k_s}} \left(1 - \sqrt{\frac{\psi_{c\beta}}{\psi}}\right) \tag{5.101}$$

After analyzing laboratory and field data Bailard (1981b) suggested that the bedload efficiency coefficient $0 < \epsilon_B < 0.44$ with a mean value of 0.21 for oscillatory flows, while it was estimated $\epsilon_B \approx 0.13$ for open channel flows by Bagnold (1963, 1966). Now it is easy to explain the difference of the bedload efficiency coefficient between open channel flows and oscillatory flows.

By comparing (5.99) and (5.101) it is found that the ratio of the bedload efficiency coefficient for oscillatory flows to that for open channel flows is

$$r_\epsilon = \ln(30h/ek_s)/\ln(30\delta_w/k_s) \tag{5.102}$$

Since the water depth h in open channel flows is much larger than the thickness of the WBL δ_w in oscillatory flows, $r_\epsilon > 1$, i.e., ϵ_B for oscillatory flows is generally larger than that for open channel flows. As an example, assuming the Shields parameters are the same, $k_s = 2d = 0.3mm$, $h = 1m$ and $\delta_w = h/50 = 2cm$, ϵ_B for oscillatory flows is 1.4 times larger than that for open channel flows.

The flow intensity determines the Shields parameter for both open channel flows and oscillatory flows. At the same time it also determines the thickness of the WBL for oscillatory flows. As the flow intensity increases, the Shields parameter

increases, and $1-\sqrt{\psi_{c\beta}/\psi}$ increases in both (5.99) and (5.101). However, δ_w usually decreases as the flow intensity increases, resulting in increasing of $e_c\kappa/\ln(30\delta_w/k_s)$ in (5.101). Thus, ϵ_B for oscillatory flows increases faster than that for open channels flows as the flow intensity increases and vice verse. In another words, as compared to that for open channel flows, the bedload efficiency coefficient for oscillatory flows is more sensitive to the flow intensity and thus the results are more scattered in the measurements, as shown in Bailard (1981b).

5.2.7 Dimensionless Bedload Transport Rate

The dimensionless bedload transport rate is defined as

$$\phi_B \equiv \frac{|\vec{q}_B|}{\sqrt{(s-1)gd}\,d} \tag{5.103}$$

After inserting (5.58) for $\int_0^{l_B} c\,dz$ and (5.85) for $|\vec{U}_B|$ in (5.45), and substituting this $\vec{q}_B$ and (5.83) for ψ into (5.103), we obtain the dimensionless bedload transport rate

$$\phi_B = \frac{e_c}{\tan\phi_d}\frac{1}{\cos\beta\,(\,1+\frac{\tan\beta}{\tan\phi_d}\,cos\theta\,)}\,(\psi-\psi_{c\beta})\,(\sqrt{\psi}-\sqrt{\psi_{c\beta}}) \tag{5.104}$$

For a horizontal bottom ($\beta = 0$) this formula becomes Engelund and Fredsøe (1976) formula. However, for a sloping bottom, the bottom slope affects the bedload transport rate not only via the critical Shields parameter, as also shown in the modified Engelund and Fredsøe (1976) formula in Engelund and Fredsøe (1982) and in Andersen (1999), but also via the term of $\cos\beta\,(\,1+\frac{\tan\beta}{\tan\phi_d}\,cos\theta\,)$, as shown in (5.104). Unfortunately, the second effect has been ignored in all previous studies.

5.3 Modified Bailard-Inman Formula for Suspended Load Transport Rate

In addition to the bedload, the sediment is also transported by flows as the suspended load mode. In fact, the suspended sediment is the major mode of the sediment transport for most situations. Different from the bedload, the suspended

load is always assumed to move along with the flow and the difference of the velocity between the sediment and the flow is the falling velocity in the vertical direction. Two approaches, as detailed as follows, were developed in this study for the suspended load transport: One is to modify an empirical formula for the suspended load transport rate to include the effect of wave breaking, the other is to develop a detailed physics-based diffusion-convection model for sediment suspension.

Numerous empirical formulas have been proposed for the suspended load transport rate. One of the common used formulas is the energetics-based formulation by Bailard (1981b), which was an extension of the works by Bagnold (1963, 1966) and Bowen (1980). The basic assumption of the energetics-based formulas is that the suspended load transport is assumed to be supported by the stream fluid via turbulent diffusion, and the energy in transporting the suspended sediment is provided by the stream.

In Bailard (1981b) the suspended sediment transport in oscillatory flows was assumed to respond to the flow condition in an instantaneous, quasi-steady manner, and the instantaneous suspended sediment transport rate was given by

$$\vec{i}_s = \frac{1}{2}\rho f \frac{\epsilon_s}{w_f}\left(|\vec{u}|^3\,\vec{u} - \frac{\epsilon_s}{w_f}\tan\beta\,|\vec{u}|^5\,\vec{i}\right) \tag{5.105}$$

where ϵ_s is the suspended load efficiency coefficient which was suggested to be $0.016 \leq \epsilon_s \leq 0.031$ for oscillatory flows (Bailard, 1981b), w_f is the falling velocity of the sediment grain, and $\vec{i}_s$ is the immersed weight suspended load transport rate which is defined as

$$\vec{i}_s \equiv (\rho_s - \rho)g\cos\beta \int_{l_B}^{h} c\vec{u}dz \;=\; (\rho_s - \rho)g\cos\beta\;\vec{q}_s \tag{5.106}$$

Here, c is the volumetric concentration of the suspended sediment and $\vec{q}_s$ is the volumetric suspended sediment transport rate per unit width.

Further investigation of this formula shows that an obvious effect, the additional stirring of sediment by the turbulence induced by wave breaking, was ignored

when applying this formula to predicting the suspended sediment transport rate inside the surfzone. Roelvink and Stive (1989) extended the work by Bailard (1981b) and proposed a formula including the effect of wave breaking for a horizontal bottom

$$\vec{i}_s = \frac{\epsilon_s \vec{u}}{w_f}(\omega_b + \omega_{Bb}) \tag{5.107}$$

where ω_b is the local turbulent energy production rate via bottom friction

$$\omega_b = \tau_b \cdot \vec{u} = \tau_0 |\vec{u}| \tag{5.108}$$

and ω_{Bb} is the local turbulent energy production rate near the bottom induced by wave breaking. Roelvink and Stive (1989) derived the same result of the energy dissipation of wave breaking as Battjes (1975)

$$\mathcal{D} = \rho \beta_d \bar{k}^{3/2} \qquad\qquad \beta_d \approx 1.0 \tag{5.109}$$

where $\bar{k}$ is a depth-mean, time-averaged turbulent kinetic energy. Roelvink and Stive (1989) also assumed

$$\omega_{Bb} = \rho \beta_d k_b^{3/2} \tag{5.110}$$

in which k_b is the magnitude of the turbulent kinetic energy near the bottom. Svendsen (1987) found that the turbulent kinetic energy decays approximately exponentially with distance from the surface. Roelvink and Stive (1989) expressed the following decay model with a depth length scale proportional to H_{rms} was assumed by,

$$k_b = \bar{k} \left[e^{(h/H_{rms})} - 1 \right]^{-1} \tag{5.111}$$

where H_{rms} is the root-mean-square wave height. Therefore, ω_{Bb} can be linked to $\mathcal{D}$ by

$$\omega_{Bb} = e_r \mathcal{D} \tag{5.112}$$

where $e_r = \left[e^{(h/H_{rms})} - 1 \right]^{-1.5}$. It can be found that $0.16 \leq e_r \leq 0.35$ for $0.5 \leq H_{rms}/h \leq 0.9$ inside the surfzone. Kobayashi and Johnson (2001) also found e_r to range from 0.2 to 1.0 in their experiments.

Hence, (5.107) can be rewritten as

$$\vec{i}_s = \frac{\epsilon_s \vec{u}}{w_f}(\omega_b + e_r D) \tag{5.113}$$

For a sloping bottom, the effect of wave breaking on the suspended load transport can also be added to Bailard (1981b) formula. According to Bailard (1981b), the energy dissipation rate associated with supporting the suspended load transport is

$$\omega_s = w_f \ (\rho_s - \rho) g \cos\beta \int_{l_B}^{h} c \, dz \tag{5.114}$$

After comparing with (5.106) it was found that this corresponds to

$$\omega_s \approx |\vec{i}_s| w_f / |\vec{u}| \tag{5.115}$$

While the turbulent energy production rate of flow via bottom friction ω_b is given by (5.108), the energy production via the movement of suspended load along the slope is

$$\omega_\beta = -(\rho_s - \rho) g \sin\beta \int_{l_B}^{h} c \ (\vec{u} \cdot \vec{i} \,) \, dz \tag{5.116}$$

which is linked to $\vec{i}_s$ after using (5.106)

$$\omega_\beta \approx -\tan\beta \ \vec{i}_s \cdot \vec{i} \ = \ -\tan\beta \ |\vec{i}_s| \cos\theta \tag{5.117}$$

In contrast to Bailard (1981b), in the present study the turbulent energy production at the bottom via wave breaking ω_{Bb} is also directly included in ω_s, in which ω_{Bb} is given by (5.112) and $\mathcal{D}$ is given by (3.14). Based on the assumption of the energetic approach

$$\omega_s = \epsilon_s \left(\omega_b + \omega_\beta + \omega_{Bb}\right) \tag{5.118}$$

Substituting (5.108) for ω_b, (5.112) for ω_{Bb}, (5.115) for ω_s and (5.117) for ω_β and rearranging terms, we obtain the magnitude of the suspended load transport rate

$$|\vec{i}_s| = \frac{1}{1 + \frac{\epsilon_s |\vec{u}|}{w_f} \tan\beta \cos\theta} \frac{\epsilon_s |\vec{u}|}{w_f} \left(\omega_b + e_r \mathcal{D}\right) \tag{5.119}$$

After neglecting higher order terms of $O(\tan\beta)^2$, we have

$$|\vec{i}_s| = \frac{\epsilon_s|\vec{u}|}{w_f}\left(1 - \frac{\epsilon_s|\vec{u}|}{w_f}\ \tan\beta\ \cos\theta\right)\ (\omega_b + e_r\mathcal{D}) \tag{5.120}$$

Bailard and Inman (1981a) assumed the direction of the suspended sediment transport was, however, somewhat different from the flow velocity because of the existence of the bottom slope and it was approximated by

$$\frac{\vec{i}_s}{|\vec{i}_s|} = \frac{\vec{u}}{|\vec{u}|} - \frac{\epsilon_s|\vec{u}|}{w_f}\ \tan\beta\left(\sin^2\theta\ \vec{i} - \sin\theta\cos\theta\ \vec{j}\right) \tag{5.121}$$

However, it can be found that the effect of the bottom slope on the direction of the suspended sediment transport is very small because both ϵ_s and $\tan\beta$ are very small, and in practice the suspended sediment can be assumed to move in the same direction as the flow does. For simplicity (5.121) is still used in the present study even though we include the additional effect of wave breaking. Combining (5.120) and (5.121) and neglecting higher order terms of $O(\tan\beta)^2$, the suspended sediment transport rate vector then reads

$$\vec{i}_s = \left(\frac{\epsilon_s\vec{u}}{w_f} - \vec{i}\,\frac{\epsilon_s^2|\vec{u}|^2}{w_f^2}\ \tan\beta\right)\ (\omega_b + e_r\mathcal{D}) \tag{5.122}$$

As shown in (5.122), the present study includes the effect of wave breaking on the suspended sediment transport as compared to Bailard (1981b), and includes the effect of the bottom slope as compared to Roelvink and Stive (1989). However, since both ϵ_s and $\tan\beta$ are very small, the effect of the small bottom slope on the suspended sediment transport is limited and the difference between (5.122) and Roelvink and Stive (1989) can be negligible for a small bottom slope in practice.

To account for the effect of the critical shear stress on the suspended sediment transport, we also intuitively include τ_c in ω_b as follows

$$\omega_b = \begin{cases} (\tau_0 - \tau_c)\,|\vec{u}| & \tau_0 > \tau_c \\ 0 & \tau_0 \le \tau_c \end{cases} \tag{5.123}$$

5.4 A Diffusion-Convection Model for Sediment Suspension

The effect of the suspended sediment on the flow condition is always neglected. The suspended sediment is typically assumed to move along with the flow, and the difference of the velocity between the sediment and the flow is the falling velocity in the vertical direction. It this assumption is adopted, it is no longer necessary to solve the momentum equation of the sediment phase or the two-phase flow for the velocity of suspended sediment, and the suspended sediment transport rate (vector) per unit width can be written as

$$q_{S\alpha} = \int_{-h_{0s}}^{\zeta} c u_\alpha \, dz \tag{5.124}$$

where u_α is the flow velocity component and h_{0s} is the still water depth of the suspended load layer and $h_{0s} = (h_0 - l_B)$ in which h_0 is the still water depth.

In this section a so-called diffusion-convection model for sediment suspension is described in detail. The vertical profile of sediment concentrations can be computed from this model and the suspended sediment transport rate can then be calculated using (5.124) provided the flow velocity is known. As compared to the empirical formula, this approach has better theoretical basis and is capable of providing more detailed information. In the following we will derive the governing equation for the diffusion-convection model, discuss the factors and parameters essentially affecting the model prediction such as the boundary conditions and the sediment diffusion coefficient, as well as the numerical scheme developed to solve the diffusion-convection problem.

5.4.1 Governing Equations

Assuming the difference of the velocity between the sediment and the flow is the falling velocity in the vertical direction, i.e., $\vec{u}_s - \vec{u} = -\vec{k}\, w_f$ in which $\vec{k}$ is the

unit vector in the vertical direction, the continuity equation of the sediment phase (5.6) can be written as

$$\frac{\partial c}{\partial t} + \frac{\partial}{\partial x_j}(u_j c) - w_f \frac{\partial c}{\partial z} = -\frac{\partial}{\partial x_j}(\overline{c' u_j'}) \tag{5.125}$$

After neglecting the effect of the suspended sediment on the flow, the continuity equation of the fluid phase (5.5) for the incompressible flow reduces to

$$\frac{\partial u_j}{\partial x_j} = 0 \tag{5.126}$$

With this equation and expressing $\overline{c' u_j'} = -\epsilon_{sj} \frac{\partial c}{\partial x_j}$ where ϵ_{sj} is the sediment diffusion coefficient in the x_j direction, (5.125) becomes

$$\frac{\partial c}{\partial t} + u_j \frac{\partial c}{\partial x_j} - w_f \frac{\partial c}{\partial z} = \frac{\partial}{\partial x_j}\left(\epsilon_{sj} \frac{\partial c}{\partial x_j}\right) \tag{5.127}$$

Because the gradients of sediment concentrations in the horizontal directions are much smaller than that in the vertical direction, i.e., $\partial c/\partial x$, $\partial c/\partial y \ll \partial c/\partial z$, the convective and diffusion terms in the horizontal directions are usually neglected as a first approximation and thus

$$\frac{\partial c}{\partial t} + (w - w_f) \frac{\partial c}{\partial z} = \frac{\partial}{\partial z}\left(\epsilon_{sz} \frac{\partial c}{\partial z}\right) \tag{5.128}$$

where w is the vertical flow velocity.

This is the so-called diffusion-convection equation for the sediment suspension. The vertical convective term $w \frac{\partial c}{\partial z}$ was neglected in most studies, as e.g., in Fredsøe and Deigaard (1992) and in Rakha *et al.* (1997). However, Nielsen (1992) showed that this vertical convective term was important for sediment distribution in oscillatory flows and thus this term is kept in the present study.

To solve the partial differential equation (5.128), the boundary conditions are required at the surface and the bottom and the sediment diffusion coefficient ϵ_{sz} needs to be determined. In addition, the instantaneous surface varies with time for oscillatory flows and the bottom elevation may also be somewhat time-dependent as

bed accretion or erosion occurs. Therefore, a coordinate transformation is required to transform the temporally varying boundaries into time-independent boundaries before a numerical scheme is applied. These problems are essential for the final solution of the sediment concentration, and are detailed as follows.

The coordinate system is chosen for the sediment suspension so that the positive x is the shoreward direction, the positive y is the downstream longshore direction, the positive z is the upward direction and $z = 0$ at the still water level (SWL). As a result, the surface boundary for the suspended sediment layer is located at $z = \zeta$ which is the instantaneous surface elevation relative to the SWL, and the bottom boundary is at $z = -h_{0s}$.

5.4.2 Surface Boundary Condition

As there is no sediment flux across through the water surface, the surface boundary condition for the suspended sediment is

$$(w_f - w)c + \epsilon_{sz}\frac{\partial c}{\partial z} = 0 \qquad z = \zeta \tag{5.129}$$

5.4.3 Bottom Boundary Condition

Although there is still no satisfactory solution to the bottom boundary condition for the suspended sediment, even for steady open channel flows, two approaches are generally used in practice. One is to set a reference sediment concentration at the bottom, and the other is to specify a spatial derivative in the vertical direction of the sediment concentration at the bottom. For sediment transport in oscillatory flows, the bottom boundary conditions are always specified as the quasi-steady equivalent to those for open channel flows.

Bottom Reference Concentration

One of the commonly used formulas for the bottom reference sediment concentration was proposed by Engelund and Fredsøe (1976). For oscillatory flows it

has also been used to calculate the instantaneous bottom sediment concentration, as e.g., in Fredsøe *et al.* (1985), Ribberink and Al-Salem (1995), and Li and Davis (1996). Engelund and Fredsøe (1976) formula is a semi-empirical formula that relates the sediment concentration at $z = 2d$ to the Shields parameter as follows

$$c_b = c_0 \left(1 + \frac{1}{\lambda_b}\right)^{-3} \tag{5.130}$$

where λ_b is the linear concentration of the suspended sediment at the bed level

$$\lambda_b^2 = \frac{0.4\kappa^2}{0.013 s\psi} \left(\psi - \psi_c - n\frac{\pi}{6} d^2 \tan\phi_d\right) \tag{5.131}$$

with

$$n = \frac{1}{d^2}\left[1 + \left(\frac{\frac{\pi}{6}\tan\phi_d}{\psi - \psi_c}\right)^4\right]^{-1/4} \tag{5.132}$$

To simplify Engelund and Fredsøe (1976) formula, Zyserman and Fredsøe (1994) suggested another empirical formula for the bottom sediment concentration that is

$$c_b = \frac{0.331(\psi - \psi_c)^{1.75}}{1 + \frac{0.331}{c_m}(\psi - \psi_c)^{1.75}} \tag{5.133}$$

where the maximum concentration $c_m = 0.32$.

Pickup Function

By using the bottom reference concentration boundary condition it is implied that there is an instantaneous equilibrium between the bed shear stress and the bottom sediment concentration. However, this instantaneous equilibrium does not exist for unsteady flows, where the near-bed sediment concentrations may well be considerable at times when the bed shear stress is zero because of the sediment settling from above. An alternative approach, which has been suggested by Nielsen *et al.* (1978) for oscillatory flows, is to consider sediment entrainment and deposition as independent processes and to specify the instantaneous rate at which sand is picked up at the bed in terms of a **pickup function** which is defined as follows

$$p \equiv -\epsilon_{sz} \frac{\partial c}{\partial z} \tag{5.134}$$

Rijn (1984) recommended the following empirical pickup function (in metric units) after analyzing the experimental data for steady flows

$$p = 0.00033\,(\frac{\psi - \psi_c}{\psi_c})^{1.5}\,\frac{(s-1)^{0.6} g^{0.6} d^{0.8}}{\nu^{0.2}} \tag{5.135}$$

This steady-flow pickup function is, however, also widely applied instantaneously on unsteady flow.

Both approaches for specifying the bottom boundary condition are included in the present model, and the differences in the final results are illustrated in Chapter 6.

5.4.4 Sediment Diffusion Coefficient and Turbulent Eddy Viscosity

The sediment diffusion coefficient ϵ_s is normally taken to be equal or proportional to the turbulent eddy viscosity ϵ of the flow. i.e.,

$$\epsilon_s = \beta_s\,\epsilon \qquad \text{with } \beta_s = O(1) \tag{5.136}$$

Two approaches are generally used to determine ϵ. One is to solve the turbulence closure model numerically. The other is to develop simple formulations to obtain the essential part of ϵ based on the theories, for example, a mixing-length theory. Because of the simplicity and accuracy in practice, the second approach has been widely used and was adopted in this study as well.

According to the classic mixing-length theory, the eddy viscosity can be expressed as the production between a length scale and a velocity scale of large eddies. i.e.,

$$\epsilon = l\sqrt{k} \tag{5.137}$$

where l is the mixing length, k is the turbulent kinetic energy and $\sqrt{k}$ represents the scale of the fluctuating velocity

$$k = \frac{1}{2}(\overline{u'^2} + \overline{v'^2} + \overline{w'^2}) \tag{5.138}$$

with u', v' and w' are the turbulent velocity fluctuations.

In the turbulent bottom boundary layer for steady flows it is often used

$$l \propto \kappa z' \qquad\qquad \sqrt{k} \propto U_* \tag{5.139}$$

where z' is the vertical distance from the bottom. Hence, the simplest expression for the eddy viscosity is

$$\epsilon = \kappa U_* z' \tag{5.140}$$

However, by comparing with data a parabolic variation of the eddy viscosity is also commonly used

$$\epsilon = \kappa U_* z'(1 - z'/D) \tag{5.141}$$

where D is the thickness of the boundary layer.

For open channel flows the bottom boundary layer covers the whole water depth. However, the situation becomes much more complex for nearshore (combined wave-current) flows. Turbulence outside the surfzone is mainly generated by the bottom boundary layer, which consists of an inner wave boundary layer (WBL) close to the bottom and an upper current boundary layer (CBL). The WBL is a very thin layer that is dominated by the oscillatory wave motion, and the CBL is a layer above the WBL that is dominated by the current motion. In addition to the bottom boundary layer, turbulence inside the surfzone is also generated via the wave breaking process.

Eddy Viscosity for Purely Oscillatory Flows

For purely oscillatory flows the wave boundary layer is limited to a very thin layer close to the bottom and above this WBL the flow is irrotational. As a result, the sediment suspension only occurs within this thin WBL. The eddy viscosity in the WBL is also expected to be proportional to the shear velocity and the boundary layer thickness which is now δ_w for purely oscillatory flows.

There have been a lot of formulas (models) which describe the vertical distribution of the eddy viscosity. In the three-layered distribution model (as e.g., Kajiura, 1968; Christoffersen and Jonsson, 1985), the WBL was divided into three layers and each layer has its own distribution function. Brevik (1981) and Trowbridge and Madsen (1987) neglected the inner layer of the three-layered model and developed two-layered eddy viscosity distribution models. However, the widely used approach is to assume one vertical distribution function of the eddy viscosity for the whole WBL, while the distribution can be constant, linear or parabolic.

The linear time-independent eddy viscosity distribution formula that was used by Grant and Madsen (1979), Grant and Madsen (1986), Glenn (1983), Christoffersen and Jonsson (1985) and You (1994) is

$$\epsilon = \kappa U_{*wm} z' \qquad\qquad z_0 < z' < \delta_w \tag{5.142}$$

where U_{*wm} is the maximum shear velocity defined as $U_{*wm} \equiv \sqrt{\tau_{wbm}/\rho}$. Here, τ_{wbm} is the maximum bottom friction. While Grant and Madsen (1979, 1986) simply chose $z_0 = 0$, Glenn (1983) and Christoffersen and Jonsson (1985) chose $z_0 = k_N/30$ where k_N is the Nikuradse roughness. The later one is theoretically complete but the difference between the two is negligible in practice.

Another realistic approach is to assume a parabolic distribution of the eddy viscosity over the WBL (as e.g., Fredsøe *et al.* (1985), Fredsøe and Deigaard (1992), Staub *et al.* (1996)).

$$\epsilon = \kappa U_{*w} z'(1 - z'/\delta_w) \qquad\qquad 0 < z' < \delta_w \tag{5.143}$$

While a time-dependent eddy viscosity was used in Fredsøe *et al.* (1985); Fredsøe and Deigaard (1992) by not taking the memory of the turbulence into account, a time-averaged ϵ was used in Staub *et al.* (1996).

There were several wave shear velocity values used in the eddy viscosity models described above. The bottom shear stress due to pure wave motion may be defined by

$$\tau_{wb}(t) = \frac{f_w}{2}\rho|u_{wb}(t)|u_{wb}(t) \tag{5.144}$$

where f_w is the bottom friction coefficient for pure wave flows, and define the wave orbital velocity at the bottom

$$u_{wb}(t) = u_0 f(\theta) \tag{5.145}$$

where u_0 is the amplitude of the bottom wave orbital velocity, $f(\theta)$ is the phase variation with $\theta = kx - \omega t$ and $f(\theta) = \cos\theta$ for sinusoidal waves. Thus, the instantaneous wave shear velocity is

$$U_{*w}(t) = \sqrt{\frac{|\tau_{wb}(t)|}{\rho}} = \sqrt{\frac{f_w}{2}}u_0|f(\theta)| \tag{5.146}$$

and the time-averaged wave shear velocity is

$$\overline{U_{*w}} \equiv \overline{U_{*w}(t)} = \sqrt{\frac{f_w}{2}}u_0\overline{|f(\theta)|} \tag{5.147}$$

which for sinusoidal waves becomes

$$\bar{U}_{*w} = \frac{2}{\pi}\sqrt{\frac{f_w}{2}}u_0 \tag{5.148}$$

The maximum bottom shear stress can be written as

$$\tau_{wbm} = max|\tau_{wb}(t)| = \frac{f_w}{2}\rho u_m^2 \tag{5.149}$$

and the maximum wave shear velocity is

$$U_{*wm} \equiv \sqrt{\frac{\tau_{wbm}}{\rho}} = \sqrt{\frac{f_w}{2}}u_m \tag{5.150}$$

where u_m is the maximum bottom wave velocity and $u_m = u_0$ for sinusoidal waves.

It is recalled that the thickness of the wave boundary layer is not well defined. Usually the (maximum) thickness is expressed as a function of wave conditions at

the bottom. One common used formula for δ_w is (Jonsson (1963, 1967), and Jonsson and Carlsen (1976))

$$\frac{30\delta_w}{k_N}\log_{10}\frac{30\delta_w}{k_N} = 1.2\frac{A_b}{k_N} \tag{5.151}$$

which can also be approximated by

$$\frac{\delta_w}{A_b} = 0.072(\frac{A_b}{k_N}) \tag{5.152}$$

where A_b is the excursion amplitude of the wave orbital velocity at the bottom, and $A_b = u_m/\omega$ in which ω is the angular wave frequency. Another widely used formula for δ_w is (Grant and Madsen (1979), Glenn and Grant (1987), and You (1994))

$$\delta_w = n\frac{\kappa U_{*wm}}{\omega} \tag{5.153}$$

where n is an empirical constant. This is also used in this study. The values of $1 \leq n \leq 2$ was suggested by Grant and Madsen (1979) and in Glenn and Grant (1987), while $n = 0.5$ was used by You (1994).

Eddy Viscosity for Combined Wave-Current Flows

For combined wave and current flows the turbulence extends over the whole water depth. Experimental data showed that while the structure of the oscillatory flows is almost unchanged by the addition of currents, the addition of waves change current profiles considerably. In essence the effect of waves is to suppress vertical current gradients and in turn the current strength inside the WBL, an effect that is generally attributed to increasing the wave-induced mixing near the bed.

In the three-layered distribution model for ϵ (as e.g., Glenn and Grant (1987), and You (1994)) the boundary layer for the combined wave-current flow was split conceptually into three parts: an inner wave dominant WBL, a wave-current interaction layer and a upper current dominant layer (CBL). However, in most models the boundary layer was split only into two parts: the inner WBL and the upper CBL.

The basic concepts in the two-layered models are the same, while the distribution functions may be different.

Grant and Madsen (1979) assumed linear distributions of ϵ in both the WBL and CBL

$$\epsilon = \begin{cases} \kappa U_{*wcm} z' & 0 < z' < \delta_w \\ \kappa U_{*c} z' & \delta_w < z' < h \end{cases} \tag{5.154}$$

where U_{*wcm} is the shear velocity corresponding to the maximum bottom shear stress for combined wave-current flows, and U_{*c} is the shear velocity for the CBL. Christoffersen and Jonsson (1985) assumed a similar distribution of ϵ in the CBL and either a constant or a linear distribution of ϵ in the WBL based on the bed roughness. A parabolic distribution of ϵ for the CBL is used by Coffey and Nielsen (1984).

It is noted that the eddy viscosity distribution models mentioned above are discontinuous at δ_w, which may not be realistic. To obtain a continuity of ϵ at $z' = \delta_w$, Fredsøe *et al.* (1985) and Fredsøe and Deigaard (1992) suggested

$$\epsilon = \begin{cases} \kappa U_{*wc} z' [1 - \frac{z'}{\delta_w}(1 - \frac{U_{*c}}{U_{*wc}})] & z' < \delta_w \\ \kappa U_{*c} z' (1 - \frac{z'}{h}) & \delta_w < z' \end{cases} \tag{5.155}$$

and Nielsen (1992) proposed

$$\epsilon = \begin{cases} \kappa U_{*c} \delta_w & z' < \delta_w \\ \kappa U_{*c} z' & \delta_w < z' \end{cases} \tag{5.156}$$

The bottom shear stress for combined wave-current flows is usually defined as

$$\tau_{b,\alpha}(t) = \frac{1}{2} \rho f_{cw} |U_{b,\alpha} + u_{wb,\alpha}(t)| (U_{b,\alpha} + u_{wb,\alpha}(t)) \tag{5.157}$$

where $U_{b,\alpha}$ is the current velocity vector near the bottom and $u_{wb,\alpha}(t)$ is the wave orbital velocity vector at the bottom. Therefore, the maximum shear stress is

$$\tau_{bm} \equiv max(|\tau_{b,\alpha}(t)|) = \frac{1}{2} \rho f_{cw} max(|U_{b,\alpha} + u_{wb,\alpha}(t)|^2) = \frac{1}{2} \rho f_{cw} u_0^2 \beta_{1m}^2 \tag{5.158}$$

where

$$\beta_{1m} = \{(\frac{U_b}{u_m})^2 + 2\frac{U_b}{u_m}\cos\mu + 1\}^{1/2} \tag{5.159}$$

Here, $U_b = |U_{b,\alpha}|$ and μ is the angle between the current velocity vector and the wave orbital velocity vector.

The bottom current shear stress τ_{bc} is usually represented by the time averaged bottom shear stress $|\ \overline{\tau_{b,\alpha}(t)}\ |$. If the bottom wave velocity is defined as (5.145) then it is found

$$\tau_{cb} = |\ \overline{\tau_{b,\alpha}(t)}\ | = \frac{1}{2}\rho f_{wc} u_0 u_0' \tag{5.160}$$

where

$$u_0' = \{(\beta_1 V_b)^2 + 2\beta_1 V_b \beta_2 u_0 \cos\mu + (\beta_2 u_0)^2\}^{1/2} \tag{5.161}$$

with

$$\beta_1 = \overline{\{(\frac{U_b}{u_0})^2 + 2\frac{U_b}{u_0}\cos\mu f(\theta) + f^2(\theta)\}^{1/2}} \tag{5.162}$$

and

$$\beta_2 = \overline{f(\theta)\{(\frac{U_b}{u_0})^2 + 2\frac{U_b}{u_0}\cos\mu f(\theta) + f^2(\theta)\}^{1/2}} \tag{5.163}$$

For sinusoidal waves, β_1 and β_2 can be further approximated by some simple curves (Svendsen *et al.*, 2002).

As a result, the instantaneous shear velocity for combined wave-current flows is

$$U_{*wc}(t) \equiv \sqrt{\frac{|\tau_b(t,\alpha)|}{\rho}} = \sqrt{\frac{f_{cw}}{2}}\ |U_{b,\alpha} + u_{wb,\alpha}(t)| \tag{5.164}$$

the maximum shear velocity is

$$U_{*wcm} \equiv \sqrt{\frac{\tau_{bm}}{\rho}} = \sqrt{\frac{f_{cw}}{2}}\ \beta_{1m} u_m \tag{5.165}$$

and the current shear velocity is

$$U_{*c} \equiv \sqrt{\frac{|\ \overline{\tau_{b,\alpha}(t)}\ |}{\rho}} = \sqrt{\frac{f_{wc}}{2}\ u_0 u_0'} \tag{5.166}$$

It is also worth to mention that in all models the thickness of the WBL for combined wave-current flows is determined with the similar formula to that for purely oscillatory flows except the shear velocity for combined wave-current flows is now used.

Eddy Viscosity for Wave Breaking

For flows inside the surfzone the turbulence is generated via both the bottom boundary layer and the wave breaking process. Although there have been several experiments and models to analyze the surfzone turbulence, it is still poorly understood.

The classic approach to estimate the eddy viscosity due to wave breaking is again to use the mixing-length theory described in Eqs.(5.137). What remains is to estimate l and k. Battjes (1975) linked l and k to the energy dissipation due to wave breaking, and this idea was further pursued by Svendsen (1987) and Svendsen *et al.* (1987). After presenting a thorough review of the turbulence characteristics in the surfzone, and analyzing several independent experimental investigations (Okayasu *et al.* (1980), Stive and Wind (1982), Hattori and Aono (1985), and Nadaoka and Kondoh (1982)), Svendsen (1987) found that the temporal variation over a wave period of the turbulent kinetic energy k at a fixed position was fairly small, which was also shown in Cox *et al.* (1995). By assuming below trough level part of dE_f/dx was dissipated and solving the depth-integrated transport equation for $\bar{k}$, Svendsen (1987) obtained

$$\sqrt{\frac{\bar{k}}{gh}} \,/\, e_x^{1/3} = f(\frac{z'}{h}) \tag{5.167}$$

where

$$e_x = \frac{1}{(gh)^{3/2}} \frac{D}{\rho} \tag{5.168}$$

and

$$D = -\frac{dE_f}{dx} \tag{5.169}$$

By fitting the experimental data by Stive and Wind (1982), $f(\frac{z}{h})$ was found to be slowly depth-varying

$$f(\frac{z'}{h}) = \frac{e^{z'/h}}{4} \tag{5.170}$$

and thus

$$\sqrt{\bar{k}} = \frac{e^{z'/h}}{4} (\frac{D}{\rho})^{1/3} \tag{5.171}$$

Using this $\bar{k}$ as a representative turbulent kinetic energy and fitting the experimental data, Svendsen *et al.* (1987) found (after our new correction)

$$l = \alpha h \qquad \text{with } 0.15 < \alpha < 0.35 \tag{5.172}$$

Hence, the eddy viscosity due to wave breaking can be expressed as

$$\epsilon = l\sqrt{k} = \alpha \frac{e^{z'/h}}{4} h(\frac{D}{\rho})^{1/3} \tag{5.173}$$

The experiment measurements have showed that high turbulent intensities due to wave breaking exist low above the bottom. However, the measurement in the layer very close the bottom (with the order of WBL thickness) is still sparse. It is possible that the turbulence generated from the intense plunging breakers may disturb the bottom boundary layer. However, such speculations have not been verified yet. It seems reasonable to assume that the layer very close to the bottom is not affected by the spilling breakers and a traditional WBL still exists in a thin layer close to the bottom.

Proposed Eddy Viscosity Model for Nearshore Flows

In the present study the eddy viscosity ϵ for nearshore flows is expressed by linear summation of the eddy viscosity due to the bottom boundary layer and that due to the wave breaking. The following model for time-independent and depth-varying eddy viscosity is proposed

$$\epsilon = \begin{cases} \kappa U_{*wcm} z'(1 - m\frac{z'}{\delta_w}) & z' < \delta_w \\ \kappa U_{*c} z'(1 - \frac{z'}{h}) + \alpha\frac{3}{5}\sqrt{\frac{z'-\delta_w}{h}}\, h(\frac{D}{\rho})^{1/3} & \delta_w < z' \end{cases} \tag{5.174}$$

where the shear velocity for the inner WBL U_{*wcm} is evaluated with (5.165), the shear velocity for the upper CBL U_{*c} is evaluated with (5.166), the WBL thickness δ_w is evaluated with (5.153), the energy dissipation is determined by the corresponding wave model. The constant m is determined by matching ϵ at $z' = \delta_w$ for the two layers and is found to be

$$m = 1 - \frac{U_{*c}}{U_{*wcm}} (1 - \frac{\delta_w}{h}) \tag{5.175}$$

It is noted that (5.170) for the empirical formula for $f(\frac{z}{h})$ used in Svendsen (1987) is replaced by another approximation in the present study

$$f(\frac{z'}{h}) = \frac{3}{5}\sqrt{\frac{z' - \delta_w}{h}} \tag{5.176}$$

While (5.176) and (5.170) provide very similar results for the upper layer, $f(\frac{z}{h})$ now approaches zero as z approaches δ_w according to (5.176) which it did not in (5.170). A qualitative illustration of the present eddy viscosity model is shown in Figure 5.2.

Based on this model, the eddy viscosities due to the wave motion and the current motion are both represented by parabolic functions. While the eddy viscosity within the WBL is always dominated by the wave motion, the eddy viscosity in the upper CBL is dominated by the current motion for flows outside the surfzone ($D = 0$) and consists of both the current-generated part and the breaker-generated part inside the surfzone.

The depth-averaged eddy viscosity is always used in the nearshore hydrodynamic model. Due to fact that the WBL is very thin, the depth-averaged eddy viscosity can for simplicity be obtained by integrating the eddy viscosity for the upper layer through the whole water depth, i.e.,

$$\begin{aligned} \bar{\epsilon} &= \frac{1}{h}\int_0^h \{\kappa U_{*c} z'(1 - \frac{z'}{h}) + \alpha\frac{3}{5}\sqrt{\frac{z' - \delta_w}{h}}\, h(\frac{D}{\rho})^{1/3}\} dz' \\ &= C_1 \kappa h U_{*c} + M h (\frac{D}{\rho})^{1/3} \end{aligned} \tag{5.177}$$

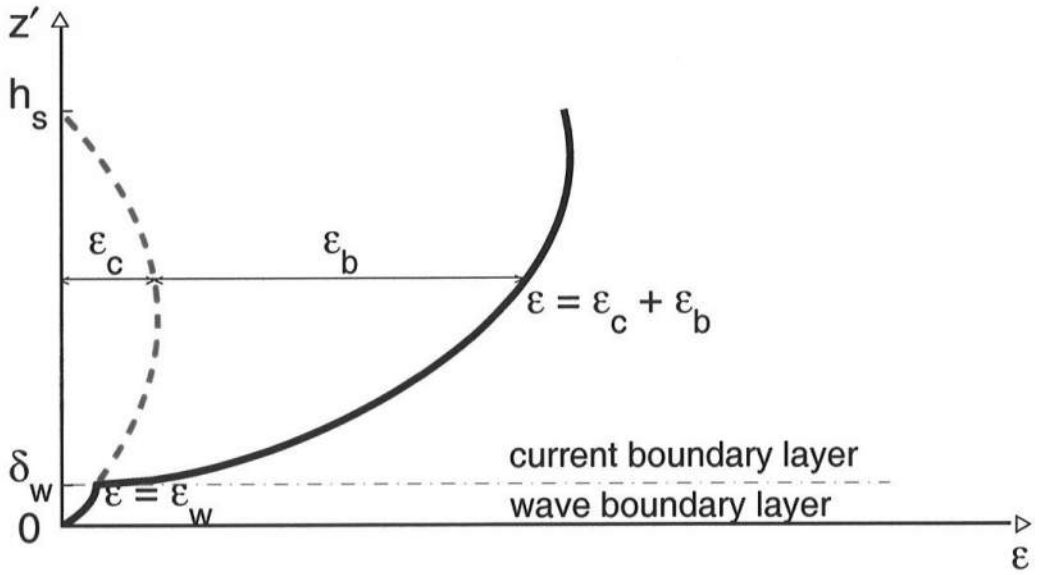

Figure 5.2: A qualitative illustration of the vertical distribution of the eddy viscosity for nearshore flows. ϵ_w, ϵ_c,ϵ_b are the eddy viscosities corresponding to the wave boundary layer, current boundary layer and wave breaking process, respectively.

where $C_1 = 1/6$ and $M \approx 0.1$ for $\alpha = 0.25$, both of which were used in the SHORECIRC. This kind of depth-averaged eddy viscosity model has been used in several turbulence closures with different values of M (as e.g., De Vriend and Stive (1987), Sanchez-Arcilla *et al.* (1992), Reniers *et al.* (1995), and Özkan-Haller and Kirby (1999)).

5.4.5 σ Coordinate Transformation

As mentioned before both the surface and bottom boundaries vary temporally for sediment suspension in oscillatory flows. In order to facilitate a finite difference scheme to solve the sediment diffusion-convection equation, the so-called σ coordinate transformation is used to transform the temporally varying boundaries

into constant boundaries. The sketch of the σ coordinate transformation is shown in Figure 5.3.

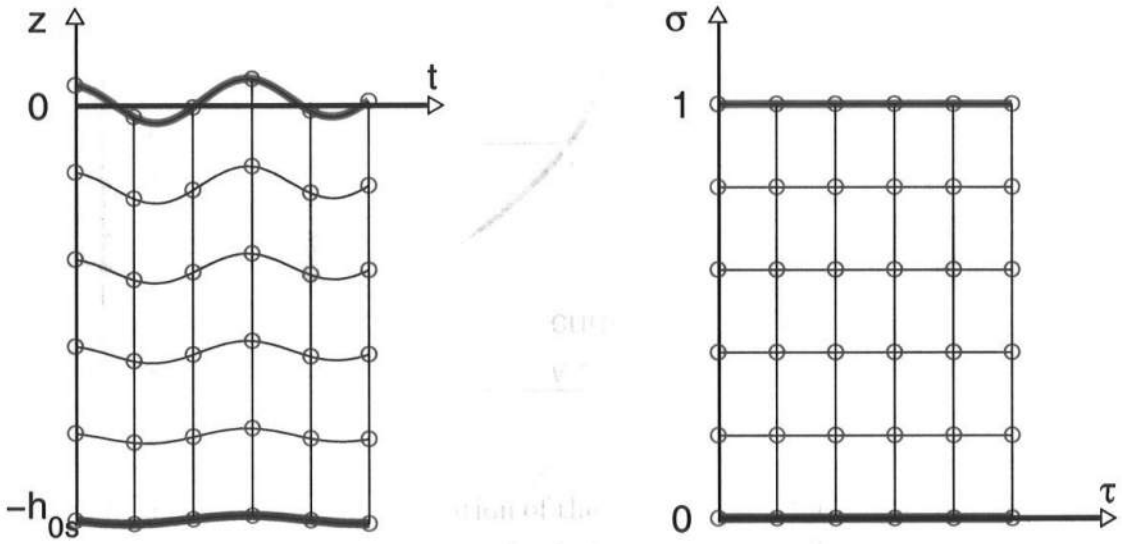

Figure 5.3: Sketch of the σ coordinate transformation

After choosing

$$\sigma = \frac{z + h_{0s}}{\zeta + h_{0s}} \qquad \tau = t \tag{5.178}$$

the temporally varying domain in the $z-t$ coordinates ($-h_{0s} \leq z \leq \zeta$) now becomes a constant domain in the $\sigma - \tau$ coordinates ($0 \leq \sigma \leq 1$), and

$$\frac{\partial}{\partial z} = \frac{\partial}{\partial \sigma}\frac{\partial \sigma}{\partial z} + \frac{\partial}{\partial \tau}\frac{\partial \tau}{\partial z} = \frac{1}{h_s}\frac{\partial}{\partial \sigma} \tag{5.179}$$

$$\frac{\partial}{\partial t} = \frac{\partial}{\partial \sigma}\frac{\partial \sigma}{\partial t} + \frac{\partial}{\partial \tau}\frac{\partial \tau}{\partial t} = \{(1-\sigma)\frac{\partial h_{0s}}{\partial t} - \sigma\frac{\partial \zeta}{\partial t}\}\frac{1}{h_s}\frac{\partial}{\partial \sigma} + \frac{\partial}{\partial \tau} \tag{5.180}$$

where $h_s = h_{0s} + \zeta$ is the local instantaneous depth of the suspended sediment layer. Since h_{0s} and ζ are both dependent on t only at given x and y, $\partial h_{0s}/\partial t = \partial h_{0s}/\partial \tau$, $\partial \zeta/\partial t = \partial \zeta/\partial \tau$. Therefore, (5.180) can be written as

$$\frac{\partial}{\partial t} = \{(1-\sigma)\frac{\partial h_{0s}}{\partial \tau} - \sigma\frac{\partial \zeta}{\partial \tau}\}\frac{1}{h_s}\frac{\partial}{\partial \sigma} + \frac{\partial}{\partial \tau} \tag{5.181}$$

Inserting (5.179) and (5.181) into the sediment diffusion-convection equation (5.128) yields

$$\frac{\partial c}{\partial \tau} = w_\sigma \frac{1}{h_s}\frac{\partial c}{\partial \sigma} + \frac{1}{h_s^2}\frac{\partial}{\partial \sigma}\left(\epsilon_{sz}\frac{\partial c}{\partial \sigma}\right) \qquad 0 \le \sigma \le 1 \tag{5.182}$$

where w_σ is the (relative) falling velocity in the $\sigma - \tau$ domain

$$w_\sigma = w_f + \sigma\frac{\partial \zeta}{\partial \tau} - (1-\sigma)\frac{\partial h_{0s}}{\partial \tau} - w \tag{5.183}$$

Now instead of solving (5.128) with temporally varying boundaries in the $z - t$ coordinates, we only need to solve (5.182) in the $\sigma - \tau$ coordinates with constant boundaries $0 \le \sigma \le 1$. Furthermore, (5.182) can be simplified by using the (linearized) kinematic surface and bottom boundary conditions for oscillatory flows which are

$$w = \frac{\partial \zeta}{\partial t} = \frac{\partial \zeta}{\partial \tau} \qquad \text{at } z = \zeta \text{ or } \sigma = 1 \tag{5.184}$$

$$w = \frac{\partial h_{0s}}{\partial t} = \frac{\partial h_{0s}}{\partial \tau} \qquad \text{at } z = -h_{0s} \text{ or } \sigma = 0 \tag{5.185}$$

It is found that $w_\sigma \approx w_f$ at the surface ($\sigma = 1$) and at the bottom ($\sigma = 0$). If assuming a linear vertical profile of w through the water column ($-h_{0s} \le z \le \zeta$ or $0 \le \sigma \le 1$), it is expected from (5.183) that w_σ is a linear function of σ, and thus $w_\sigma = w_f$ for the whole water column because $w_\sigma = w_f$ at both $\sigma = 0$ and $\sigma = 1$. Hence, w_σ can be replaced by w_f as a first approximation and this would significantly simplify the numerical procedure of solving (5.182).

5.4.6 Numerical Scheme

The numerical method used to solve (5.182) was chosen to be as consistent as possible with that used in the SHORECIRC (Sancho and Svendsen, 1997). The predictor-corrector scheme was used for the differential in time, the Adams-Bashforth scheme was used for the predictor and the Adams-Moulton scheme was used for the corrector.

If symbolically denoting

$$\mathbf{F} = \mathbf{w}_\sigma \frac{\mathbf{1}}{\mathbf{h}_s}\frac{\partial \mathbf{c}}{\partial \sigma} + \frac{\mathbf{1}}{\mathbf{h}_s^2}\frac{\partial}{\partial \sigma}\left(\epsilon_{sz}\frac{\partial \mathbf{c}}{\partial \sigma}\right) \tag{5.186}$$

Eq. (5.182) can be written as

$$\frac{\partial c}{\partial \tau} = \mathbf{F} \tag{5.187}$$

The Adams-Bashforth scheme for the predictor is

$$c_k^* = \mathbf{c_k^n} + \mathbf{\Delta\tau\alpha_0(\alpha_1 F_k^n + \alpha_2 F_k^{n-1} + \alpha_3 F_k^{n-2}) + O(\Delta\tau^3)} \tag{5.188}$$

where superscript n denotes the time level, subscript k denotes the grid locations in the σ direction and

$$\alpha_0 = 1/12, \qquad \alpha_1 = 23, \qquad \alpha_2 = -16, \qquad \alpha_3 = 5 \tag{5.189}$$

The Adams-Moulton scheme for the corrector is

$$c_k^{n+1} = \mathbf{c_k^n} + \mathbf{\Delta\tau\beta_0(\beta_1 F_k^* + \beta_2 F_k^n + \beta_3 F_k^{n-1}) + O(\Delta\tau^3)} \tag{5.190}$$

where $\mathbf{F_k^*}$ is the value of $\mathbf{F}$ corresponding to c_k^* and

$$\beta_0 = 1/12, \qquad \beta_1 = 5, \qquad \beta_2 = 8, \qquad \beta_3 = -1 \tag{5.191}$$

Because (5.182) is a parabolic-type partial differential equation and the convection term $\frac{w_\sigma}{h_s}\frac{\partial c}{\partial \sigma}$ is important, the second order upwind difference scheme is used for the first-order derivative $\frac{\partial c}{\partial \sigma}$. The upwind difference scheme is chosen to avoid the so-called 'wiggle' problem and to achieve better numerical stability (Peyret and Taylor, 1982). The second order accuracy is chosen to avoid the numerical diffusion problem. The second order upwind difference scheme for $\frac{\partial c^n}{\partial \sigma}$ is

$$\frac{\partial c_k^n}{\partial \sigma} = (1-\alpha)\frac{-c_{k+2}^n + 4c_{k+1}^n - 3c_k^n}{4\Delta\sigma} + (1+\alpha)\frac{3c_k^n - 4c_{k-1}^n + c_{k-2}^n}{4\Delta\sigma} + O(\Delta\sigma^2) \tag{5.192}$$

where $\alpha = -\text{sign}(w_\sigma)$ and $\alpha = -1$ if $w_\sigma \approx w_f$. In addition, the centered difference scheme is used for the diffusion term in (5.182).

For a general linear parabolic equation

$$\frac{\partial f}{\partial t} + A\frac{\partial f}{\partial x} - \epsilon\frac{\partial^2 f}{\partial x^2} = 0 \tag{5.193}$$

the criterion for the numerical stability is

$$\Delta t \leq \frac{(\Delta x)^2}{2\epsilon + \Delta x|A|} \tag{5.194}$$

if the non-centered difference scheme is used for the first-order spatial derivative (Peyret and Taylor, 1982). This criterion becomes the well known Courant-Friedrichs-Lewy condition (CFL) $\Delta t \leq \frac{\Delta x}{|A|}$ only when $\epsilon = 0$. Thus, the stability criterion of the numerical scheme used in the present study is expected to be

$$\Delta\tau \leq \frac{(\Delta\sigma)^2}{2\frac{\epsilon_{sz}}{h_s^2} + \Delta\sigma\frac{|w_\sigma|_m}{h_s}} \tag{5.195}$$

which can also be rewritten as

$$\Delta t \leq \frac{(\Delta z)^2}{2\epsilon_{sz} + \Delta z|w_\sigma|_m} \tag{5.196}$$

where $|w_\sigma|_m$ is the maximum $|w_\sigma|$ and as a first approximation $|w_\sigma|_m \approx w_f$.

5.5 Phase Variations of Surfzone Waves

A significant effect of the wave phase variation on the time-averaged sediment transport rate arises from the wave asymmetry about the horizontal axis or the so-called wave skewness: higher and shorter crest, but longer and shallower trough. The wave skewness tends to induce net sediment transport in the wave direction (shoreward and downstream direction).

Waves become more peaked and thus wave skewness becomes more considerable as propagating to breaking. This variation can be represented by the non-linear wave theories, such as the cnoidal wave theory used in this study. However, no conventional wave theory is appropriate for the description of the phase variation of

surfzone waves, as discussed in Chapter 3. To represent the effect of the wave asymmetry on the sediment transport inside the surfzone, an empirical formula for the wave phase variation, which is usually expressed in terms of the surface profile, is necessary.

Extensive experimental observations have found that the surface profiles inside the surfzone change from a peaked shape at breaking to a sawtooth-like profile at the shoreline, and the wave skewness reduced as waves propagate to the shoreline. Based on this fact, the simplest formulation of the surface profile inside the surfzone appears to be a linear weighted summation of the peaked shape at breaking and the sawtooth shape at the shoreline, i.e.,

$$\frac{\eta(t)}{H} = \frac{\eta(t)}{H}|_B \frac{h}{h_B} + (\frac{1}{2} - \frac{t}{T})(1 - \frac{h}{h_B}) \tag{5.197}$$

where $\frac{\eta(t)}{H}|_B$ is the surface profile at breaking which is predicted by the cnoidal wave theory in the present study.

It is worth to mention that (5.197) just qualitatively describes the surface profile variation inside the surfzone which in reality is much more complex than (5.197) indicates. On the other hand, while no wave theory can appropriately represent the surface profile inside the surfzone, Eq. (5.197) can simply and reasonably represent the surface profile and thus the effect of the wave asymmetry on the net sediment transport in the surfzone. This can not be represented by ordinary linear wave theory.

5.6 Bathymetry Update

The bathymetry update is derived by solving the depth-integrated equation for sediment mass conservation

$$\frac{\partial h_0}{\partial t} = \frac{1}{1 - n_p} \left(\frac{\partial \bar{q}_{sx}}{\partial x} + \frac{\partial \bar{q}_{sy}}{\partial y} \right) \tag{5.198}$$

where n_p is the porosity of the sediment and $n_p \approx 0.4$, $\bar{q}_{sx}$ and $\bar{q}_{sy}$ are the time-averaged volumetric sediment transport rates per unit width including both the bedload and the suspended load, i.e.,

$$\bar{q}_{s\alpha} = \bar{q}_{B\alpha} + \bar{q}_{S\alpha} = \bar{q}_{B\alpha} + \overline{\int_{h_{0s}}^{\zeta} c u_\alpha \, dz} \tag{5.199}$$

It is always important to analyze the performance of a mathematical model and test the accuracy of the model predictions with experimental measurements. The performance the present sediment transport model incorporated with the wave models and the SHORECIRC will be analyzed in Chapter 6 and 7, and comparisons between the model predictions and experimental data in the LSTF are presented in Chapter 7.

Chapter 6

ANALYSES OF PREDICTED NEARSHORE SEDIMENT TRANSPORT

The objective of this chapter is to present extensive numerical simulation results predicted by the sediment transport model combined with the wave models and the SHORECIRC model. The purpose is to test the behavior of the present sediment transport model, analyze the effects of the primary factors on sediment transport and illustrate some characteristics of nearshore sediment transport which are difficult to discern in experiments. A presumed simple scenario, which is sediment transport on a plane beach under regular wave environments, was simulated using the present wave-current-sediment transport model. The initial beach profile and incident wave conditions were chosen to be the same as those in Test 6N in the LSTF. The regular wave condition was chosen over the irregular wave for the purpose of illustrating the effects of nearshore wave transformations on sediment transport. These effects tend to be smoothed out for irregular waves because of the temporal variations of wave conditions and spatial variations of the breaking location. A plane beach profile was chosen over an equilibrium beach profile in order to amplify cross-shore variations of sediment transport and to illustrate the evolutions of the beach profile.

6.1 Sediment Transport Rates Predicted by Various Models

Bedload transport rate

Figure 6.1 shows the cross-shore variations of the wave-averaged volumetric bedload transport rates per unit width in the cross-shore direction (Q_{Bx}) and in the longshore direction (Q_{By}) predicted by the Engelund and Fredsøe (1976) formula, by the Bailard and Inman (1981a) formula, by the present modified Engelund and Fredsøe formula (5.104) and by the modified Bailard and Inman formula (5.97) with the bedload efficiency coefficient $\epsilon_B = 0.21$, respectively. The cnoidal-bore wave model was used in the tests and thus the wave asymmetry about the horizontal axis, sometimes termed the wave "skewness", is presented in the model results. The cross-shore location of wave breaking is at $x_B = 9\,m$. It is worth to point out that under regular wave conditions the wave-averaged sediment transport rate is also the net transport rate.

It is seen that all the formulas predict a similar trend for the cross-shore distributions of net bedload transport rates. A net shoreward bedload transport is predicted for the region outside the surfzone whereas a net seaward transport for the inner surfzone as the result of the balance between the wave asymmetry and cross-shore currents. The predicted longshore bedload transport rates are always towards the downstream direction because both longshore currents and the wave asymmetry tend to induce net bedload transport in that direction. The effect of the wave asymmetry on the net longshore bedload transport rate is limited because of the small wave angles. A significant longshore bedload transport appears to occur in the mid surfzone where significant longshore currents exist.

As illustrated theoretically in Chapter 5, both the Bailard and Inman (1981a) formula and the Engelund and Fredsøe (1976) formula for the bedload transport rate can be derived from the two-phase flow theory. The difference between the two formulas lies in the fact that while the bedload efficiency coefficient is assumed to be a constant in the Bailard and Inman (1981a) formula it is linked to the Shields parameter in the Engelund and Fredsøe (1976) formula. Therefore, both

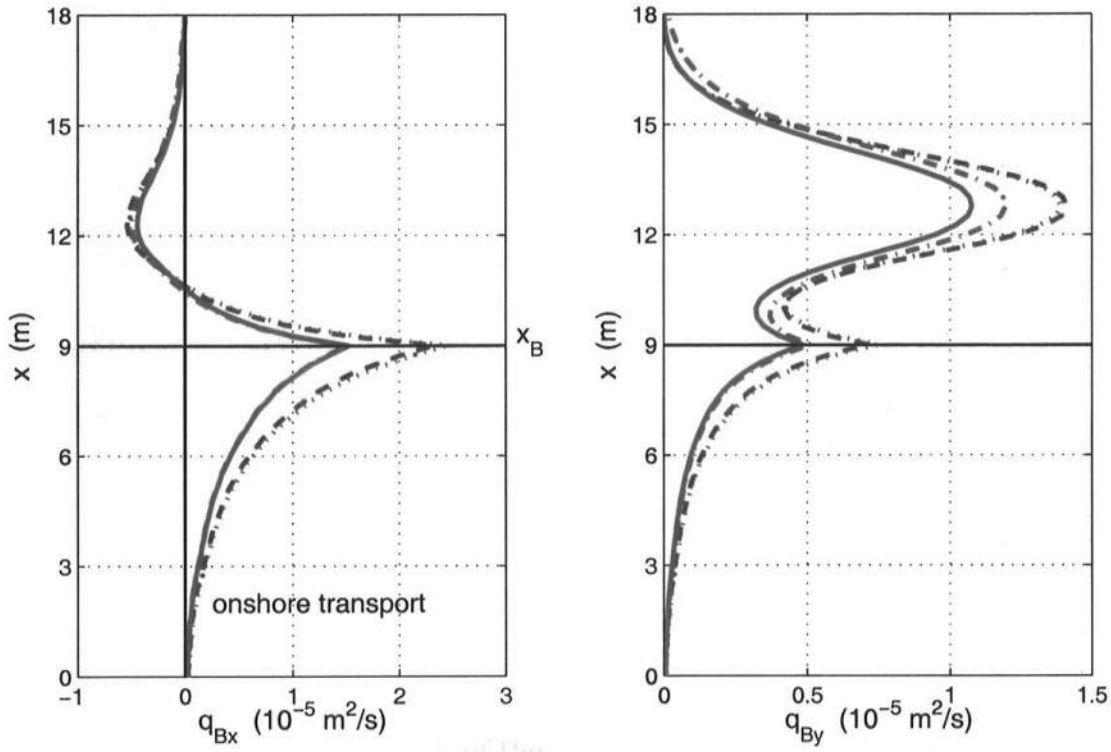

Figure 6.1: Comparison of wave-averaged bedload transport rates per unit width predicted by the Engelund and Fredsøe (1976) formula (..), by the Bailard and Inman (1981a) formula (−.), by (5.104) (−−) and by (5.97) with $\epsilon_B = 0.21$ (—).

formulas predict similar shapes but somewhat different magnitudes of the cross-shore variations of bedload transport rates, as shown in Figure 6.1. For different values of ϵ_B, different magnitudes of bedload transport rates would be predicted by the Bailard and Inman (1981a) formula.

As an improved version of the Bailard and Inman (1981a) formula, Eq. (5.97) includes the effect of the critical shear stress on the bedload transport. The net bedload transport rates per unit width predicted by (5.97) are also presented in Figure 6.1. The net bedload transport rates predicted by (5.97) are close to those predicted by the Bailard and Inman (1981a) formula for the region outside the surfzone but are smaller for the region inside the surfzone. As illustrated in (5.97)

the instantaneous bedload transport rate decreases after including the critical shear stress. Because the wave velocity is dominant for flows outside the surfzone, the effect of the critical shear stress on the instant bedload transport rate in the shoreward direction is comparable to that in the seaward direction, resulting in a negligible difference in the net bedload transport rates. However, as currents become significant inside the surfzone, less net bedload transport rate would be predicted in the current direction after including the effect of the critical shear stress.

Figure 6.1 also demonstrates the net bedload transport rates per unit width predicted by (5.104), which is an improved version of the Engelund and Fredsøe (1976) formula. However, no obvious difference is found in the predicted results between (5.104) and the Engelund and Fredsøe (1976) formula. This is because the bottom slope in this test case is so small that the difference between two formulas is hardly discriminated.

Suspended sediment transport rate

Figure 6.2 presents cross-shore variations of the wave-averaged suspended sediment transport rates per unit width in the cross-shore direction (Q_{Sx}) and in the longshore direction (Q_{Sy}) predicted by the Bailard (1981b) formula, by the modified Bailard formula (5.122) and by the present sediment diffusion-convection model using the pick-up function as the bottom boundary condition, respectively.

As similar to the bedload and for the similar reasons, the net cross-shore suspended sediment transport rate is found to be towards the shore for the region outside the surfzone and towards the sea for the inner surfzone. The net longshore suspended sediment transport rate is in the downstream direction and becomes significant in the mid surfzone.

Different from the bedload, the cross-shore distributions of the net suspended sediment transport rates predicted by different models (formulas) show significant difference, both in shapes and in magnitudes. This is because different models

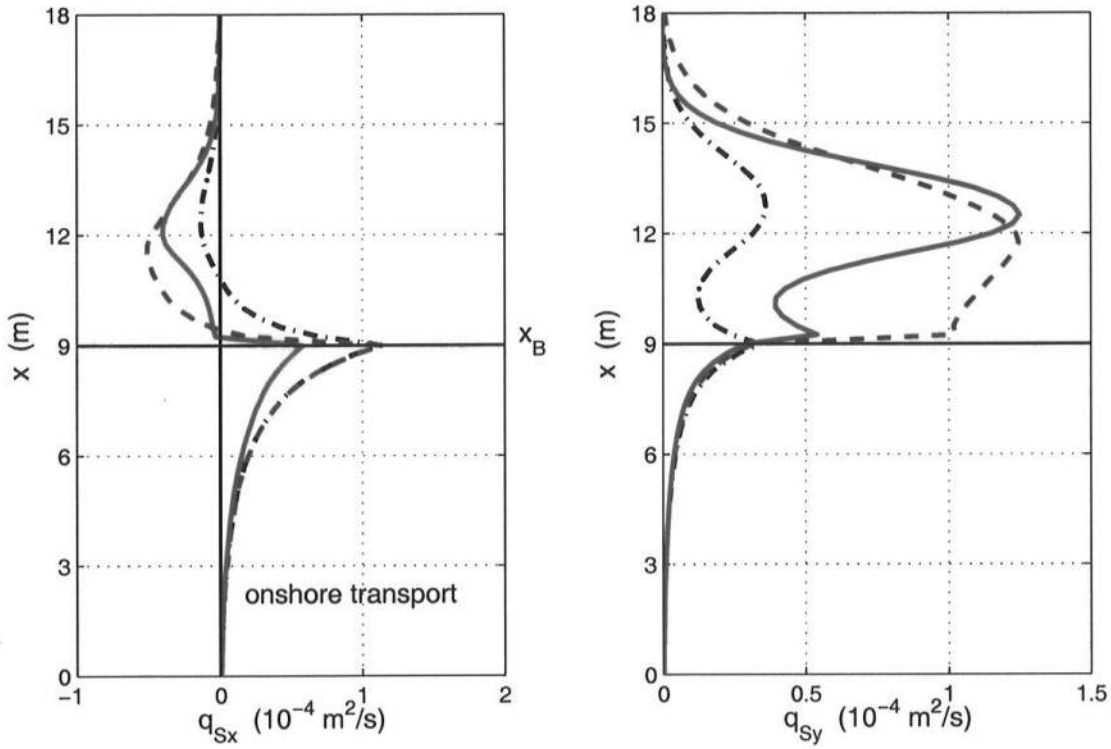

Figure 6.2: Comparison of the wave-averaged suspended sediment transport rates per unit width predicted by Bailard (1981b) (−.), by (5.122) (−−), by the present sediment diffusion-convection model applying the pick-up function boundary condition (—)

(formulas) are based on different approaches. The Bailard (1981b) formula is derived from a simple energetic approach, while the present diffusion-convection model is solving the sediment diffusion-convection equation.

After including the effect of wave breaking, the net longshore suspended sediment transport rate predicted by the modified Bailard formula (5.122) is much larger than that determined by the original version for the surfzone. As illustrated in (5.122), the energy dissipation of wave breaking is directly added in the modified Bailard formula. Hence, a considerable transport rate is predicted by this formula for the region immediately after breaking where the maximum energy dissipation occurs. The effect of wave breaking is reflected in the diffusion-convection model by

including the energy dissipation in the sediment diffusion coefficient (see (5.174)). However, the bottom boundary condition of sediment suspension is primarily determined by the bottom friction. As a result, the diffusion-convection model predicts a significant net suspended sediment transport rate in the mid surfzone where significant longshore currents occur instead of the region immediately after breaking, as shown in Fig. 6.2. This might be more realistic.

It is interesting to notice the double peaks of the predicted cross-shore distributions of net longshore transport rates of the bedload as well as the suspended load. One is located around the breaking point and the other in the mid surfzone,. The double peaks seem to be the result of the balance between the intensity of longshore currents and the wave asymmetry. It is also seen that wave breaking not only amplifies the magnitudes of the double peaks but also shifts the location of the first peak from the breaking point into the surfzone for suspended sediment.

For this test case, the magnitude of the net bedload transport rate is approximately 10 to 20 percent of the suspended load transport rate. However, this ratio may vary in reality depending on the wave and current conditions and sediment characteristics.

6.2 Effect of Wave Asymmetry

Figure 6.3 illustrates the difference of the cross-shore variations of the net bedload transport rates predicted by (5.122) using the sinusoidal wave model and using the cnoidal-bore wave model, respectively. Similarly Figure 6.4 presents the difference for suspended sediment transport. It is noted that for both the bedload and the suspended load, the cross-shore sediment transport is towards the shoreward direction for the region outside the surfzone and changes to the seaward direction for the inner surfzone if the cnoidal-bore wave model is applied. However, it is always towards the seaward direction if using the sinusoidal wave model. While the cross-shore variations of longshore sediment transport rates have double peaks if using

the cnoidal-bore wave model, only one peak is found if using the sinusoidal wave model. In addition, the predicted longshore transport rate using the sinusoidal wave model is generally less than that using the cnoidal-bore wave model. Thus there are significant differences in the predicted transport rates using the two models. These differences essentially reflect the effects of wave asymmetry on the sediment transport in nearshore flows.

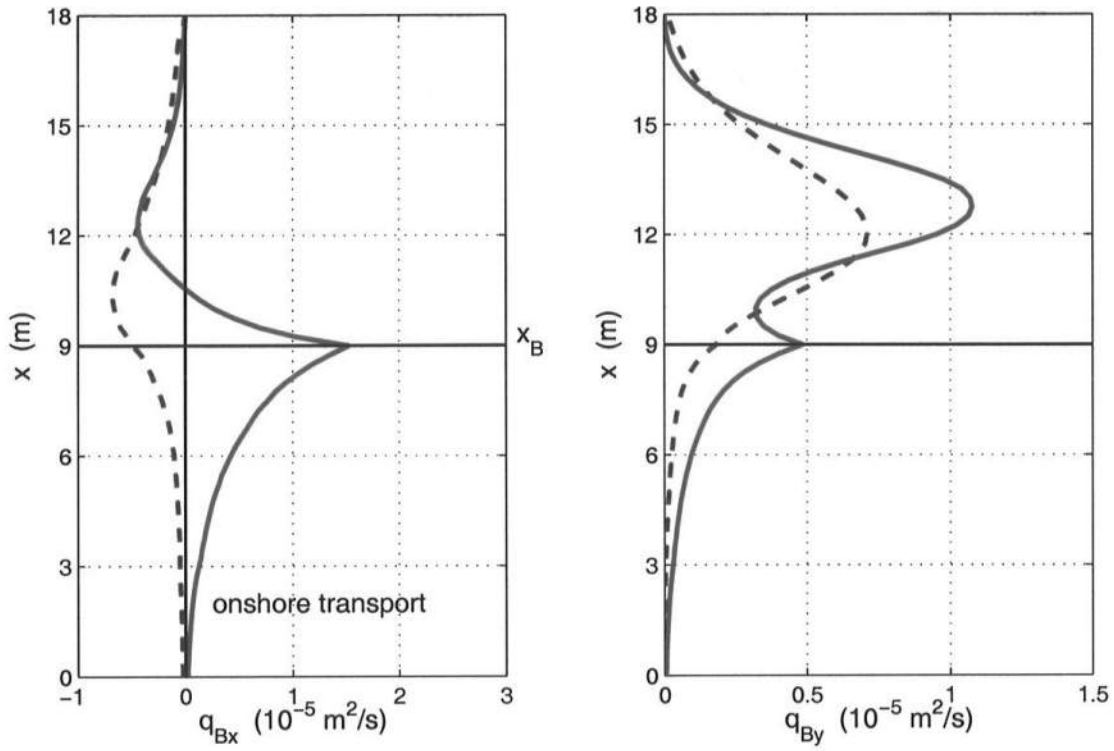

Figure 6.3: Comparison of the wave-averaged bedload transport rates per unit width predicted by (5.122) using the sinusoidal wave model(−−) and using the cnoidal-bore wave model (—)

Sinusoidal waves are symmetric about the horizontal axis. The forward (shoreward and downstream) and backward (seaward and upstream) sediment transport rates due to the wave velocity are equivalent because of the wave symmetry. Therefore, the net sediment transport rate would be zero for pure (sinusoidal) waves

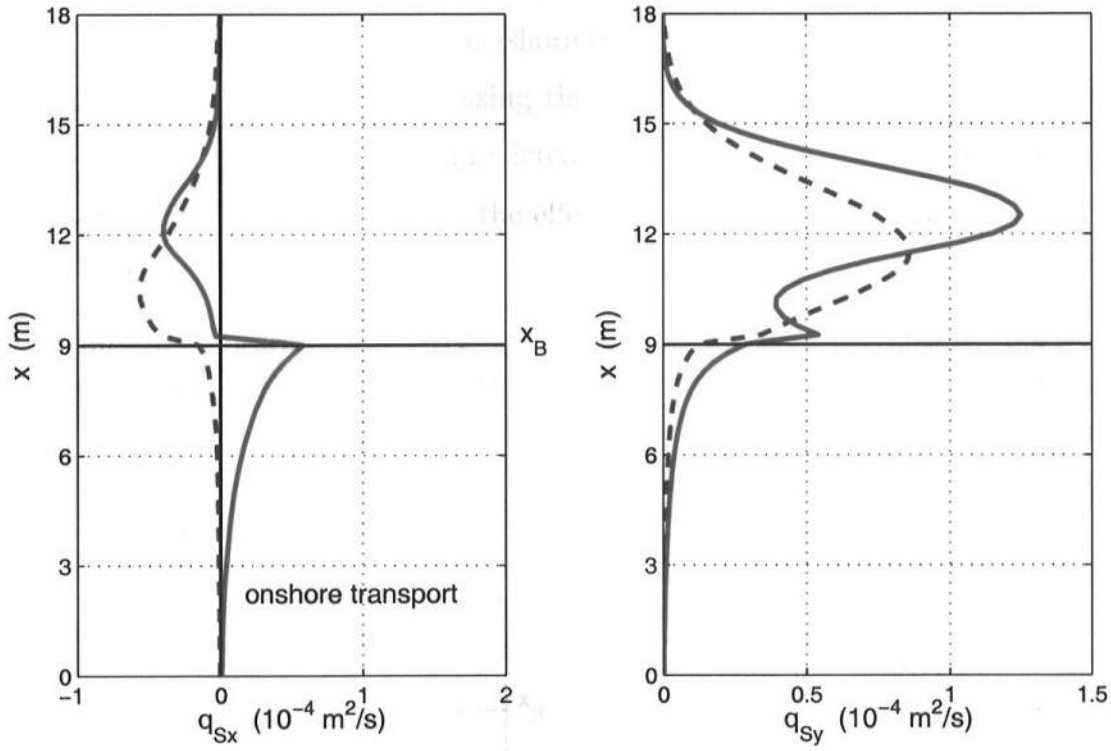

Figure 6.4: Comparison of wave-averaged suspended sediment transport rates per unit width predicted by the present diffusion-convection model using the sinusoidal wave model(− −) and using the cnoidal-bore wave model (—).

and would follow the current direction (i.e., the seaward and downstream direction) for combined (sinusoidal) wave and current flows. As shown in Figure 6.3 and 6.4, a net seaward and downstream sediment transport is predicted for the whole nearshore region if the sinusoidal wave model is used.

However, nearshore waves in the field are always in non-sinusoidal shapes. Waves become more peaked as approaching breaking: crests shorter and more peaked, troughs longer and flatter. This wave asymmetry about the horizontal axis, i.e., the wave skewness, tends to induce more sediment transport in the wave direction than the opposite direction, resulting in a net sediment transport in the wave direction (i.e., the shoreward and downstream direction). On the other hand,

wave-induced currents tend to induce a net sediment transport in the current direction (i.e., the seaward and downstream direction). Therefore, the direction of net sediment transport depends on the balance between the wave skewness and currents.

As a result of weak currents, the effect of wave asymmetry on sediment transport appears to be more noticeable for the region outside the surfzone. As waves propagate to breaking, wave skewness increases and reaches the maximum value at breaking, and so does the net sediment transport rate which is towards the shoreward and downstream direction. Inside the surfzone the situation is reversed. Instantly after breaking starts waves become less peaked and wave skewness reduces. On the other hand, wave-induced currents become more significant. The result is that the direction of net sediment transport rate is adjusted to follow the current direction as current intensity increases. As shown in Figure 6.3 and 6.4, a net seaward sediment transport in the cross-shore direction is predicted for the mid and inner surfzone, and the maximum net seaward sediment transport occurs in the middle surfzone where the strongest wave-induced currents occur.

As a result of the small wave angles in this test case (incident wave angle of 10 degrees), the longshore wave velocity component and thus the effect of wave asymmetry on the net longshore sediment transport rate are less significant than those in the cross-shore direction. Therefore, the predicted longshore sediment transport rates show less difference when using the sinusoidal or cnoidal-bore wave model, as compared to the significant difference in the predicted cross-shore transport rates.

6.3 Contributions of Waves and Currents

To illustrate more clearly the contributions of waves and of currents to sediment transport, Figures 6.5 and 6.6 present the predicted net bedload and suspended load transport rates per unit width for purely oscillatory flows, pure current flows and the combined wave and current flows. Here, Eq. (5.122) was used for the bedload, the diffusion-convection model was used for the suspended load. The flow

velocities used in the tests are the wave velocity only, wave-induced current velocity only and combined wave and current velocity, respectively.

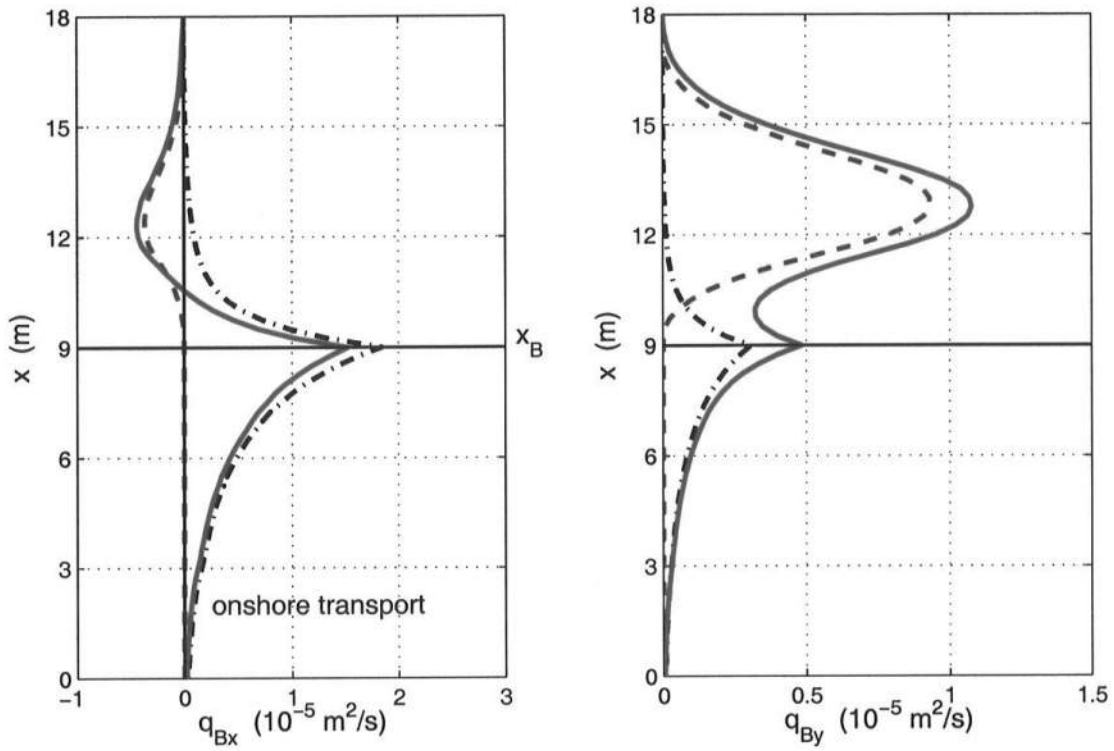

Figure 6.5: Comparison of the wave-averaged bedload transport rates per unit width predicted by (5.122) for three flow conditions: waves only (−.), wave-induced currents only (−−) and combined wave and current flows (—)

As shown in Figures 6.5 and 6.6, the wave asymmetry is the mechanism of the net sediment transport which is towards the wave direction for pure oscillatory flows. The trend of the cross-shore variation of net sediment transport rates follows that of wave skewness: increase towards breaking and decay inside the surfzone. For pure current flows, the net sediment transport is as expected towards the seaward and downstream direction as currents do, and the trend of the cross-shore variation of net sediment transport rates is similar to that of wave-induced currents. Sediment transport mainly occurs inside the surfzone with the maximum transport rate at the

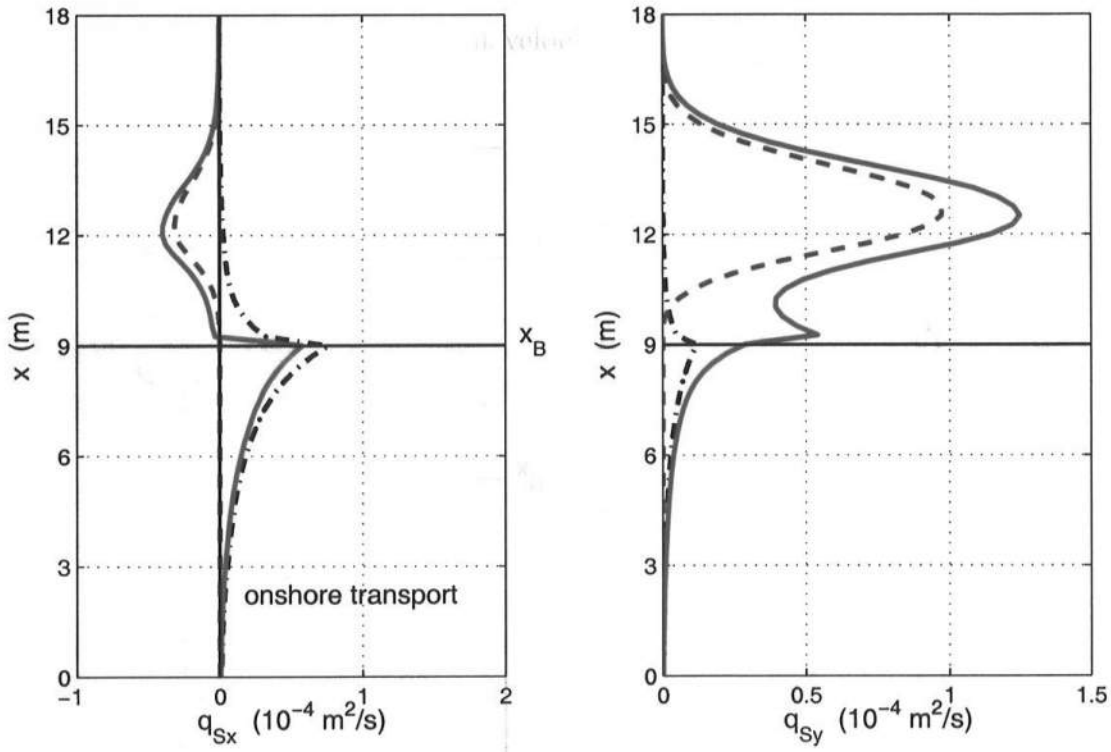

Figure 6.6: Comparison of the wave-averaged suspended sediment transport rates per unit width predicted by the present diffusion-convection model for three flow conditions: waves only (−.), wave-induced currents only (−−) and combined wave and current flows (—)

middle surfzone where the maximum current occurs, while the net sediment transport rate is negligible outside the surfzone where currents are weak. For combined wave and current flows, currents together with the wave asymmetry determine the net sediment transport rate, which, however, is not the linear summation of the transport rate for pure oscillatory flows and that for pure wave-induced current flows.

The reason for this can be seen by considering the suspended sediment transport in combined wave and current flows. We divide the instantaneous sediment

concentration and velocity into a wave-averaged part and an oscillatory part

$$c = \bar{c} + c_t \qquad\qquad u_\alpha = U_\alpha + u_{w\alpha} \tag{6.1}$$

Here, the wave-averaged part of the flow velocity becomes the current velocity and the oscillatory part is the wave velocity. Therefore, the wave-averaged sediment transport rate is

$$\bar{q}_{s\alpha} = \overline{\int_{h_0}^{\zeta} c u_\alpha \, dz} = \int_{h_0}^{\bar{\zeta}} \bar{c} U_\alpha \, dz + \overline{\int_{h_0}^{\zeta} c u_{w\alpha} \, dz} \tag{6.2}$$

As an example, Figure 6.7 presents the $\int_{h_{0s}}^{\bar{\zeta}} \bar{c} U_\alpha \, dz$ for suspended sediment as well as the wave-averaged transport rates predicted by the diffusion-convection model together with the cnoidal-bore wave model. It is found that the net suspended transport rates differ from the $\int_{h_{0s}}^{\bar{\zeta}} \bar{c} U_\alpha \, dz$ primarily in the region close to breaking where wave asymmetry is significant, while the difference is negligible for the inner and middle surfzone and for the region further offshore where wave asymmetry is negligible. Hence, it can be concluded that the effect of the wave asymmetry on net sediment transport lies in $\overline{\int_{h_0}^{\zeta} c u_{w\alpha} \, dz}$, which is the difference between $\bar{q}_{s\alpha}$ and $\int_{h_0}^{\bar{\zeta}} \bar{c} U_\alpha \, dz$, as illustrated in (6.2). As wave angles in the test case are small, the $\overline{\int_{h_0}^{\zeta} c u_{wy} \, dz}$ is small as well, resulting in a limited difference between the net longshore sediment transport rates and the $\int_{h_0}^{\bar{\zeta}} \bar{c} V \, dz$. In another words, for small wave angles $\int_{h_0}^{\bar{\zeta}} \bar{c} V \, dz$ could be an approximation of the net longshore sediment transport rates.

Figure 6.7 also shows the predicted net sediment transport rates for pure (wave-induced) current flows, which are smaller than $\int_{h_0}^{\bar{\zeta}} \bar{c} U_\alpha \, dz$ for combined wave and current flows. Because current velocities are the same in the two tests, the difference is caused by the difference in sediment concentration. The (wave-averaged) sediment concentration is generated by both currents and wave velocities for combined wave and current flows. However, for pure current flows it is only created by the currents.

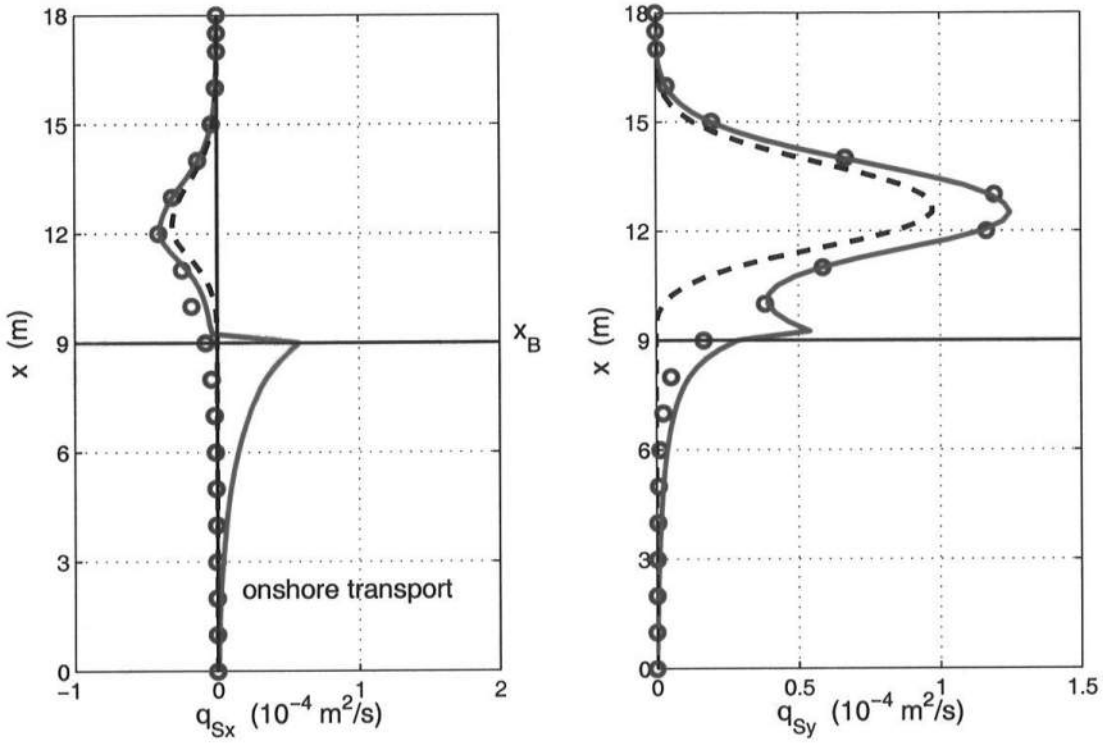

Figure 6.7: Comparison between the predicted wave-averaged suspended sediment transport rates per unit width (—), and $\int_{h_{0s}}^{\bar{\zeta}} \bar{c}U_i\, dz$ (∘) for combined wave and current flows, as well as the wave-averaged sediment transport rates per unit width for pure wave-induced current flows (−−).

6.4 Vertical Convection of Sediment

As a first approximation the convection term caused by the vertical flow velocity is usually neglected and the boundaries of suspended sediment layer are assumed to be temporally constant (as e.g., from the bottom to the mean water level). The diffusion-convection equation (5.128) for suspended sediment thereby reduces to

$$\frac{\partial c}{\partial t} - w_f \frac{\partial c}{\partial z} = \frac{\partial}{\partial z}\left(\epsilon_{sz}\frac{\partial c}{\partial z}\right) \qquad -h_{0s} \le z \le \bar{\zeta} \tag{6.3}$$

which is the governing equation for the so-called **sediment diffusion model**. The sediment diffusion model is commonly used to solve for the vertical distribution of

suspended sediment in open channel flows as well as in combined wave and current flows (as e.g., Fredsøe and Deigaard (1992) and Rakha *et al.* (1997)). However, Nielsen (1992) showed that in oscillatory flows the diffusion model is not accurate enough for sediment suspension and the effect of the vertical flow velocity should be included.

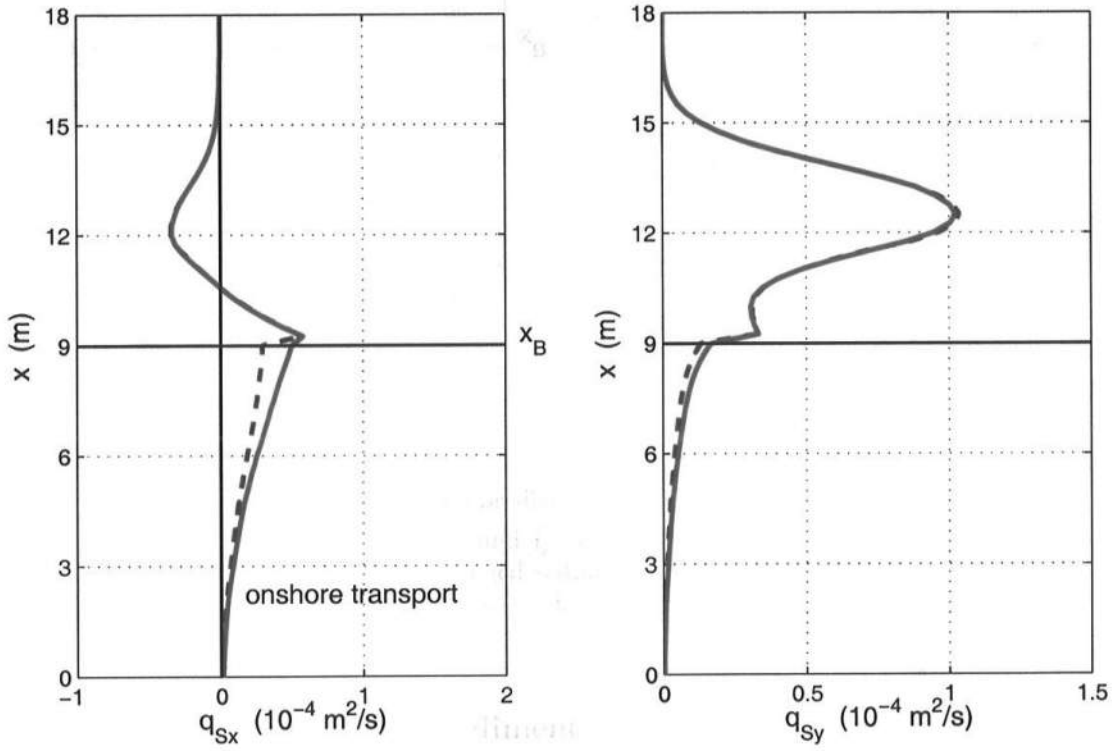

Figure 6.8: Comparison of the wave-averaged suspended load transport rates per unit width predicted by the diffusion model (−−) and by the diffusion-convection model (—).

Figure 6.8 presents the cross-shore variations of the net suspended sediment transport rates per unit width predicted by the diffusion model compared with those by the diffusion-convection model. The cnoidal-bore wave model was used as the wave driver and flow conditions are the same in two tests. The bottom reference concentration boundary condition was applied so that the sediment concentrations

at the bottom are the same in two tests. Therefore, the difference in the predicted results of suspended sediment transport is solely caused by the fact whether the effect of the vertical flow velocity is included or not. The comparison reveals that the net sediment transport rate predicted by the diffusion model is slightly smaller than that predicted by the diffusion-convection model for the region outside the surfzone. However, for the surfzone the difference is indistinguishable. In other words, a limited effect of the vertical flow velocity on the net suspended sediment transport rate primarily occurs outside the sufzone but is negligible inside the surfzone.

Figure 6.9 demonstrates the vertical distributions of the wave-averaged sediment concentrations at $x = 6\,m$ ($3\,m$ before breaking) and at $x = 12\,m$ ($3\,m$ after breaking) predicted by the diffusion model and by the diffusion-convection model, respectively. A more uniform vertical distribution of sediment concentration is predicted by the diffusion-convection model than by the diffusion model for the region outside the surfzone, whereas the vertical profiles predicted by two models show indiscernible difference inside the surfozne. In addition, the difference in the vertical profiles at $x = 6\,m$ is more eminent for the upper water column and is limited for the near-bottom. However, as showed in Figure 6.9, the absolute value of sediment concentration at the upper water column is much smaller than that at the near-bottom (as e.g., less than 10^{-5} for $4\,cm$ above the bottom). Hence, the absolute difference of sediment concentrations predicted by the diffusion-convection model and by the diffusion model appears to be negligible in practice.

Figure 6.10 shows the phase variations of suspended sediment concentrations at different vertical locations at (a) $x = 6\,m$ (with still water depth of $0.4\,m$) and at (b) $x = 12\,m$ (with still water depth of $0.2\,m$), respectively. The wave period is $2.5\,s$. It is seen that while the bottom sediment concentration (at $z = -0.40\,m$ for $x = 6\,m$) are the same, the sediment concentration (at $z = -0.38\,m$, i.e., $2cm$ above the bottom) predicted by the diffusion-convection model not only has a larger

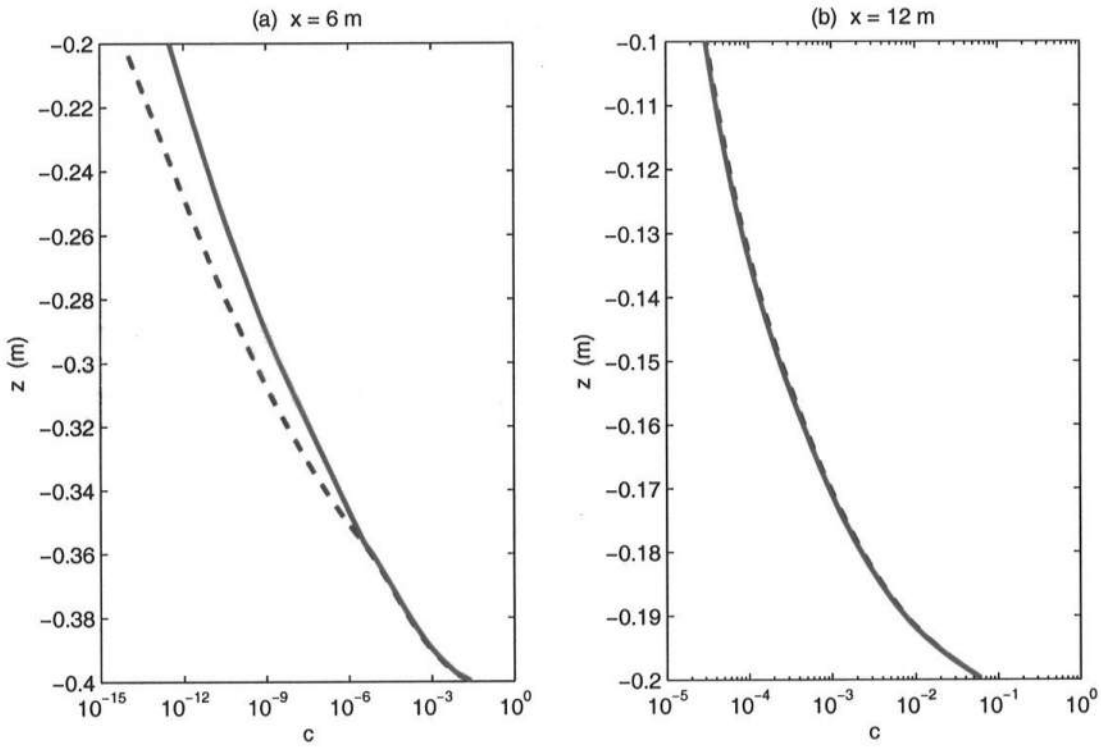

Figure 6.9: Comparison of vertical profiles of the wave-averaged sediment concentrations at (a) $x = 6\,m$ and at (b) $x = 12\,m$ predicted by the diffusion model (−−) and the diffusion-convection model (—)

wave-averaged value but also has a more significant temporal variation and asymmetry, and this difference is expected to be more distinguishable further above the bottom. However, at $x = 12\,m$ (inside the surfzone) the phase variations of sediment concentrations predicted by two models reveal negligible difference

The comparisons illustrated in Figures 6.8, 6.9 and 6.10 suggest that the vertical flow velocity in combined wave and current flows tends to intensify sediment suspension, and results in a more significant temporal variation and a more uniform vertical distribution of suspended sediment concentrations and thus a larger transport rate given the same bottom boundary condition. This effect of the vertical flow velocity would increase the sediment "diffusion" coefficient if the sediment diffusion

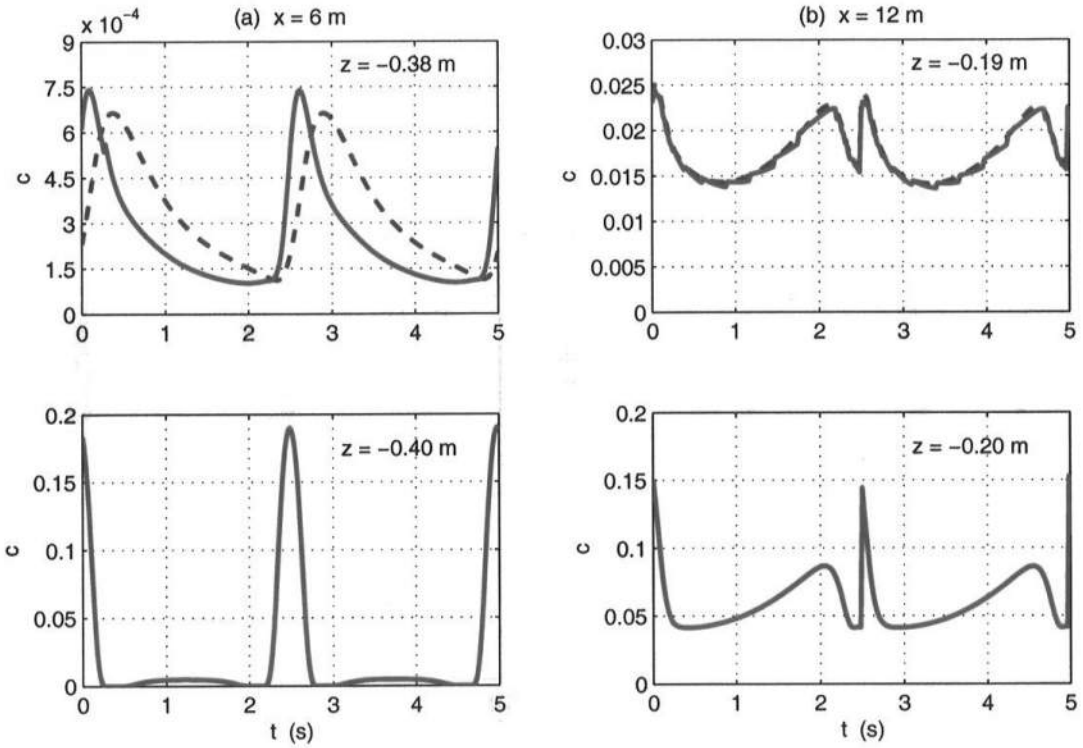

Figure 6.10: Comparison of the time series of sediment concentrations at (a) $x = 6m$ and at (b) $x = 12\,m$ predicted by the diffusion model (−−) and the diffusion-convection model (—)

model is used.

The turbulent intensity of the flow and thus the sediment diffusion coefficient are small in the current boundary layer for the region outside the surfzone where currents are weak. Therefore, the effect of the vertical flow velocity on sediment suspension becomes more noticeable. This effect is expected to be more distinguishable for purely oscillatory flows in which no current exist, as shown by the experimental data (Nielsen, 1992). The vertical flow velocity is negligible near the bottom and increases vertically, and so does its effect on sediment suspension. However, as the result of the stronger currents and particularly the significant turbulent intensity

caused by wave breaking, the turbulent intensity and the sediment diffusion coefficient in the current boundary layer becomes more significant inside the surfzone, resulting in a negligible effect of the vertical flow velocity on sediment suspension. Hence, no discernible difference appears in the predicted sediment concentrations and transport rates between the diffusion-convection model and the diffusion model for the region inside the surfzone.

The absolute differences of the predicted suspended sediment concentrations and transport rates between the diffusion-convection model and the diffusion model are rather small. Suspended sediment typical concentrates near the bottom and the concentration decay very fast with water depth. However, the vertical flow velocity increases vertically and is negligible near the bottom. Hence, the sediment convection due to the vertical flow velocity primarily occurs in the upper water column where the sediment concentration is negligible and thus the effect of the vertical flow velocity on suspended sediment transport rate is fairly limited.

6.5 Effect of Bottom Boundary Conditions

The bottom boundary condition is a primary factor in determining sediment suspension in the water column. As discussed in Chapter 5, two approaches are typically applied for the bottom boundary condition, one is to specify the bottom reference concentration and the other to specify the vertical gradient of sediment concentration at the bottom (pick-up function). Figure 6.11 shows the net suspended sediment transport rates predicted by the diffusion-convection model applying the bottom reference concentration as boundary condition (5.130) and the other applying the pick-up function as boundary condition (5.135). The cnoidal-bore wave model was used as the wave driver and flow conditions are the same in the two tests. Thus the differences in the predicted suspended sediment concentrations and transport rates between the two tests are caused entirely by the different bottom

boundary conditions applied. It is seen from that the predicted net suspended sediment transport rates are surprisingly close in the two tests.

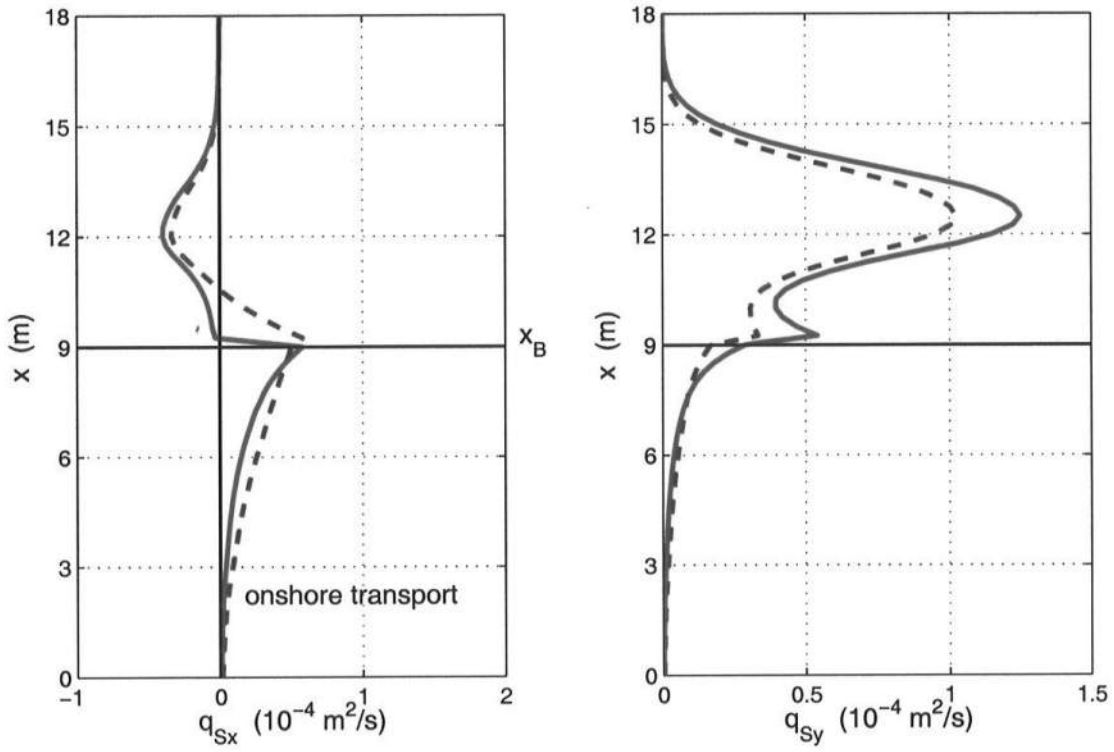

Figure 6.11: Comparison of wave-averaged suspended sediment transport rates per unit width predicted by the diffusion-convection model applying the bottom reference concentration boundary condition (−−) and applying the pick-up function boundary condition (—)

Figure 6.12 shows the equivalent vertical profiles of the wave-averaged suspended sediment concentrations at $x = 6\,m$ and at $x = 12\,m$ predicted in two tests. It is interesting to notice that the model applying the bottom reference concentration boundary condition (5.130) predicts a larger wave-averaged bottom sediment concentration but at the same time a faster vertical decay of the concentration near the bottom, resulting in a slightly smaller net transport rate, than the model applying the pick-up function (5.135). As the sediment diffusion coefficients are the

same in the two tests, the slopes of the vertical profiles of (logarithmic) sediment concentrations are close for most of the water column except near the bottom where the vertical gradient of sediment concentration is specified by (5.135) when applying the pick-up function bottom boundary condition.

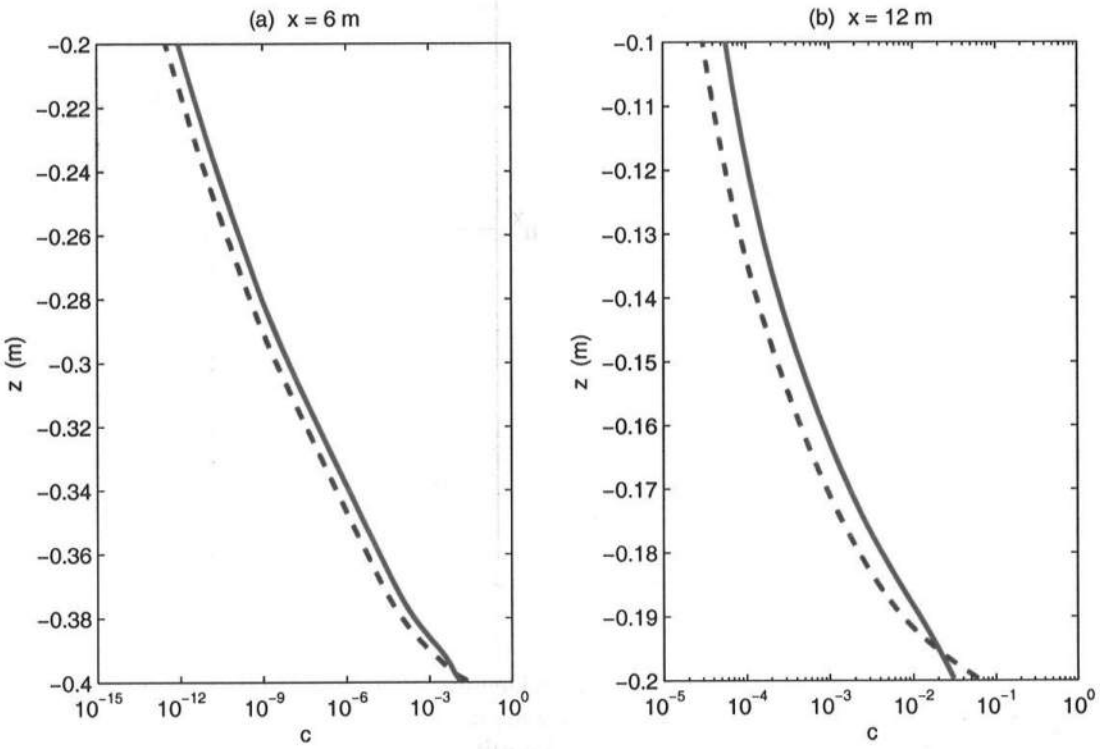

Figure 6.12: Comparison of vertical profiles of the wave-averaged sediment concentrations at (a) $x = 6\,m$ and at (b) $x = 12\,m$ predicted by the diffusion-convection model applying the bottom reference concentration boundary condition (−−) and applying the pick-up function boundary condition (—)

Figure 6.13 presents the temporal variations of the instantaneous sediment concentrations in the two tests at different vertical positions at $x = 6\,m$ and at $x = 12\,m$, respectively. The bottom sediment concentrations (at $z = -0.40\,m$ for $x = 6\,m$ and at $z = -0.20\,m$ for $x = 12\,m$) predicted by the model using the bottom

reference concentration as boundary condition appear to have not only larger wave-averaged values but also much larger temporal variations. Tt $x = 6\,m$ the bottom sediment concentration varies from 0 to 0.190 within one wave period with a wave-averaged value of 0.024 and at $x = 12\,m$ from 0.041 to 0.153 with an average value of 0.060 if specifying the bottom reference concentration with (5.130). However, if specifying the pick-up function with (5.135), at $x = 6\,m$ it only varies from 0.002 to 0.047 with an average value of 0.013 and at $x = 12\,m$ from 0.026 to 0.038 with an average value of 0.031.

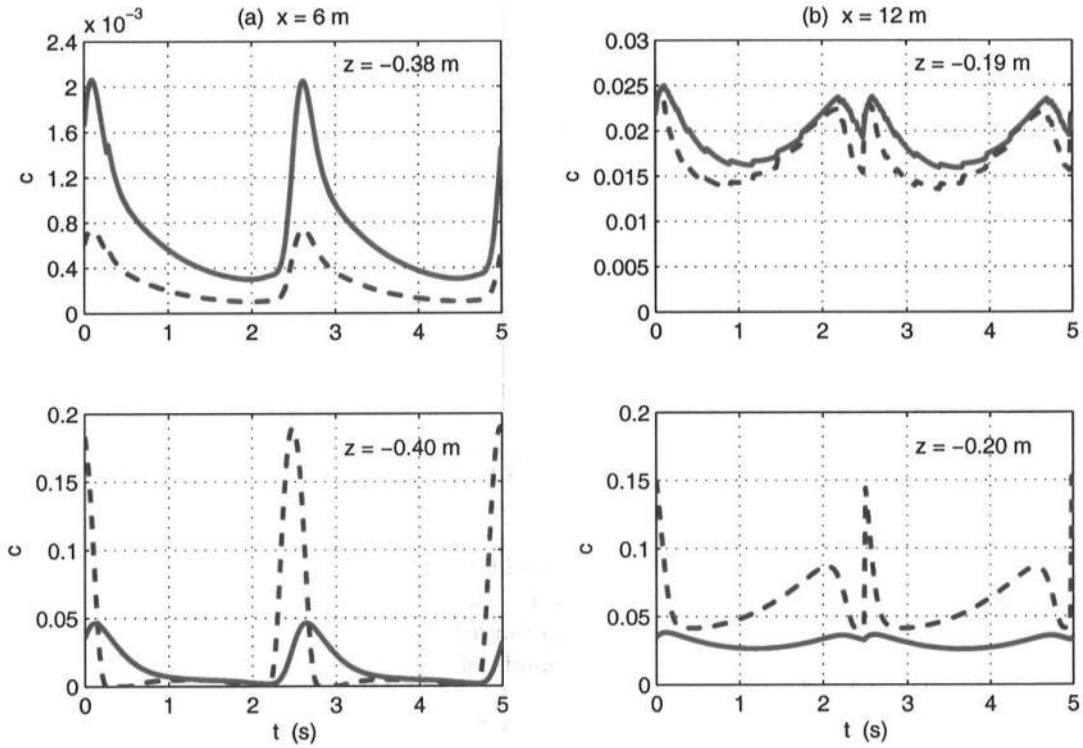

Figure 6.13: Comparison of the time series of sediment concentrations at (a) $x = 6\,m$ and at (b) $x = 12\,m$ predicted by the diffusion-convection model applying the bottom reference concentration boundary condition (−−) and applying the pick-up function boundary condition(—)

If the bottom reference concentration boundary condition is used, it is implied

that an instantaneous equilibrium exists between the bottom shear stress and the suspended sediment concentration. According to (5.130) the instantaneous bottom sediment concentration is proportional to the instant effective bottom shear stress. Therefore, the concentration is zero when the shear stress is zero and reaches the maximum value when the shear stress is maximal, as shown in Figure 6.13. However, this instantaneous equilibrium may not exist for oscillatory flows. If dense clouds of sediment are settling from above the concentration at the bottom may well be larger when the shear stress is zero. If the pick-up function is used as the bottom boundary condition, the vertical gradient of the sediment concentration at the bottom instead of the concentration itself is a power function of the effective bottom shear stress based on (5.135). Thus, when the shear stress is zero the vertical gradient of sediment concentration at the bottom is zero but the bottom concentration is not zero, as shown in Figure 6.13.

6.6 3D Sediment Transport

Figure 6.14 presents the cross-shore variations of the vertical profiles of wave-averaged sediment concentrations predicted by the diffusion-convection model using the pickup function boundary condition. The cnoidal-bore model was used as the wave driver. This figure illustrates the distinguishable variations of sediment suspension in the cross-shore direction. For the offshore-most region, the bottom sediment concentration is small and sediment suspension is only limited in a very thin layer close to the bottom as a result of the small bottom shear stress and small sediment diffusion coefficient. The flow velocity, consisting of the wave velocity and the current velocity, becomes larger as breaking is approached, resulting in a larger bottom shear stress and sediment diffusion coefficient, and thus a larger bottom sediment concentration and a thicker sediment suspension layer. An intense sediment suspension is found in a much thicker layer in the outer and middle surfzone, as a result of

the larger bottom shear stress and the wave breaking process which intensifies the flow turbulence and thus the sediment diffusion coefficient.

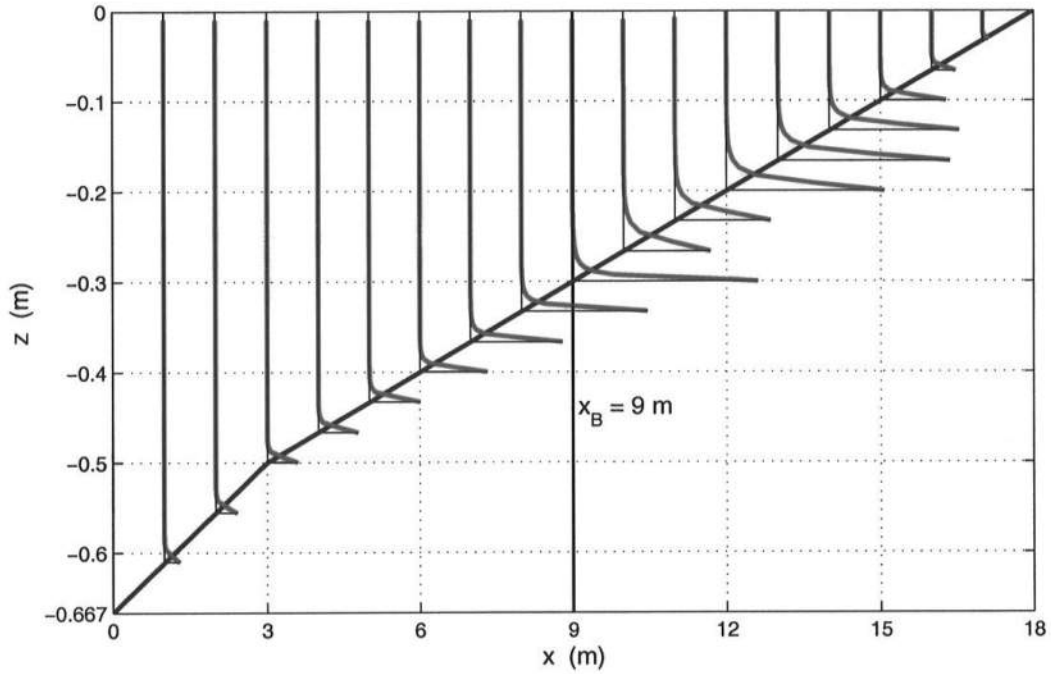

Figure 6.14: Predicted cross-shore variations of the vertical profiles of wave-averaged sediment concentrations

The vertical profiles of suspended sediment motions are summarized in Figure 6.15 which shows a 3-D plot of the predicted vectors of $\vec{u}c$ for the transect of $y = 17.7\,m$. This figure demonstrates that the net suspended sediment transport varies with depth rapidly in magnitudes and slightly in directions. This figure also illustrates a significant cross-shore variations, not only in magnitudes but also in directions, of net suspended sediment transport. While the net suspended sediment is negligible in the offshore-most region, intense net sediment transport is found towards the shoreward direction immediately outside the breaking and towards the longshore direction in the outer and middle surfzone. Because of the effect of the wave asymmetry, the directions of suspended sediment transport differ from those

of wave-induced currents (see Figure 4.13), particularly for the region outside the surfzone.

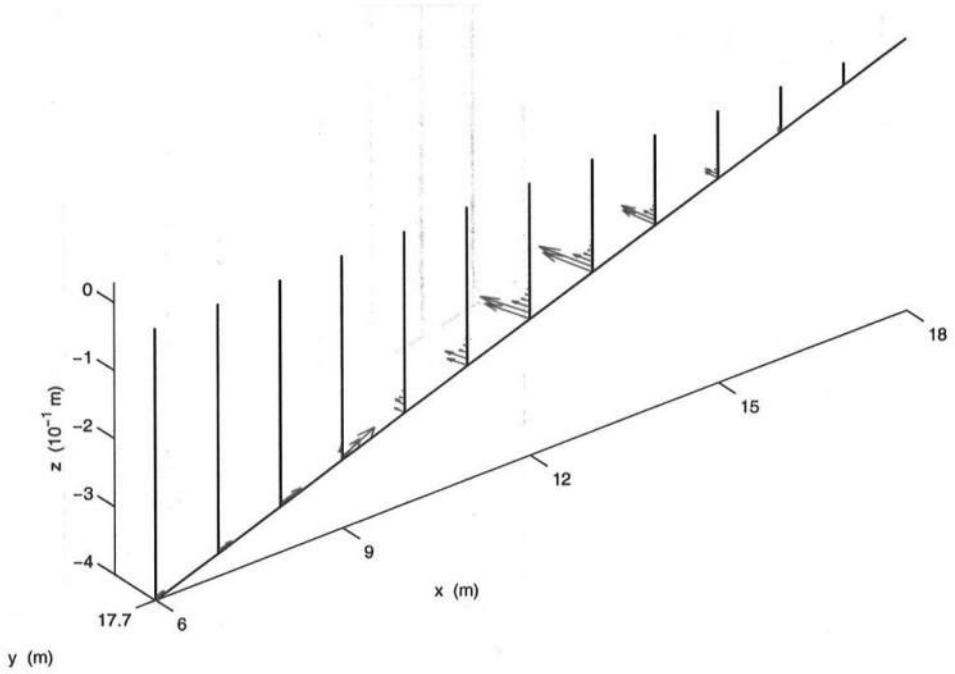

Figure 6.15: Predicted cross-shore variations of the vertical profiles of wave-averaged sediment fluxes.

The 2-D plot of the total sediment transport rate vectors, consisting of the bedload and the suspended load, predicted by the diffusion-convection model is presented in Figure 6.16. This figure again shows that the directions of the net sediment transport rates are different from those of wave-induced currents (Figure 4.10). Net sediment transport occurs primarily in the shoreward direction for the region outside the surfzone but primarily in the longshore direction for the surfzone. It is expected from the cross-shore variations of sediment transport rates that a bar would be formed around the breaking line and erosion would generally occurs in the inner and middle surfzone for this test case.

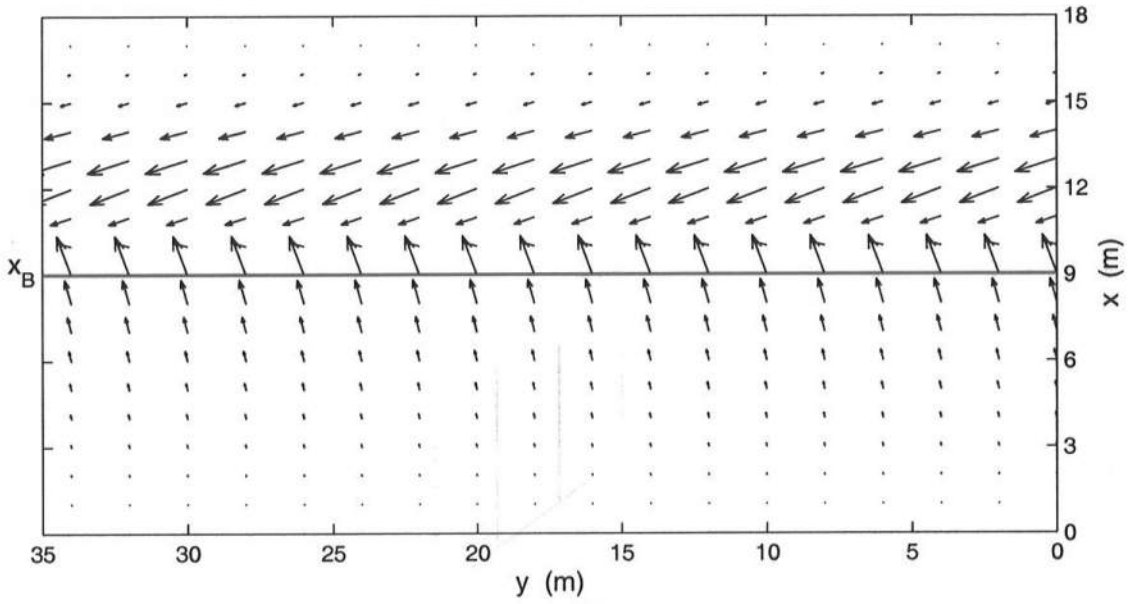

Figure 6.16: Predicted total sediment transport rate vectors per unit width in the LSTF.

6.7 Predicted Evolutions of Beach Profile

Beach profile in the field can vary considerably depending on wave conditions and resulting wave-induced currents and sediment transport. The cross-shore sediment transport plays a primary role in the beach profile evolution for a straight parallel beach, for which Eq. (5.198) reduces to

$$\frac{\partial h_0}{\partial t} = \frac{1}{1-n_p}\frac{\partial \bar{q}_{sx}}{\partial x} \tag{6.4}$$

This equation illustrates that beach accretion occurs ($\partial h_0/\partial t < 0$) where $\partial \bar{q}_{sx}/\partial x < 0$, and beach erosion occurs ($\partial h_0/\partial t > 0$) where $\partial \bar{q}_{sx}/\partial x > 0$.

Figure 6.17 shows the evolutions of the beach profile from an initial plane beach to a beach with a breaker bar within one hour predicted by the sediment diffusion-convection model. The resulting evolutions of the beach profile when using the cnoidal-wave model and the sinusoidal wave model are presented in this figure. It is seen that a sand bar is formed around the breaking and erosion generally occurs

in the mid and inner surfzone no matter whether the cnoidal-bore or the sinusoidal wave model is used.

The differences in the predicted evolutions of beach profile for different wave models being used lie in the location and the size of the breaker bar, slight beach evolution outside the surfzone and the width of the erosion area inside the surfzone. As for sinusoidal waves a net seaward cross-shore sediment transport is predicted for the whole nearshore region and the maximum seaward transport rate occurs slightly inside the surfzone (see Figs 6.3 and 6.4), a higher but narrower sand bar is predicted close to breaking. A slight beach accretion is predicted seaward of the bar but a considerable beach erosion is found shoreward of the bar which covers most of the surfzone ($x > 10\,m$), as shown in Figure 6.17 (b).

However, if the cnoidal-bore wave model is used, a net shoreward sediment transport is predicted outside the surfzone and it changes into seaward-directed transport, as shown in Figs 6.3 and 6.4. This results in an significant beach accretion from approximately $1\,m$ outside breaking to $3\,m$ inside breaking and a wider but lower sand bar formed in this region, with a considerable beach erosion seaward to the bar which covers the middle and inner surfzone ($x > 12\,m$) and a slight erosion seaward to the bar as well, as illustrated in Figure 6.17 (a).

It is worth to point out again that the comparisons presented in this chapter are meant as illustrations of the complex mechanisms that govern sediment motion and beach development. They are limited to the sediment transport on a plane beach under regular wave conditions. As illustrated several places in the discussion above, the results and conclusions may not be the same for different situations and will be different for sediment transport on a non-plane beach under irregular wave environments. It is expected that the cross-shore distributions of net sediment transport rates can be more uniform and the locations of the wider and lower

breaker sand bar may migrate because of temporal variations of wave conditions and particularly spatial variations of wave breaking locations for irregular waves. In addition, the evolutions of beach profile may also be different depending on the initial beach profile. Some of the characteristics of nearshore sediment transport on an "equilibrium" beach will be illustrated in the following chapter through the comparisons with Test 1H in the LSTF.

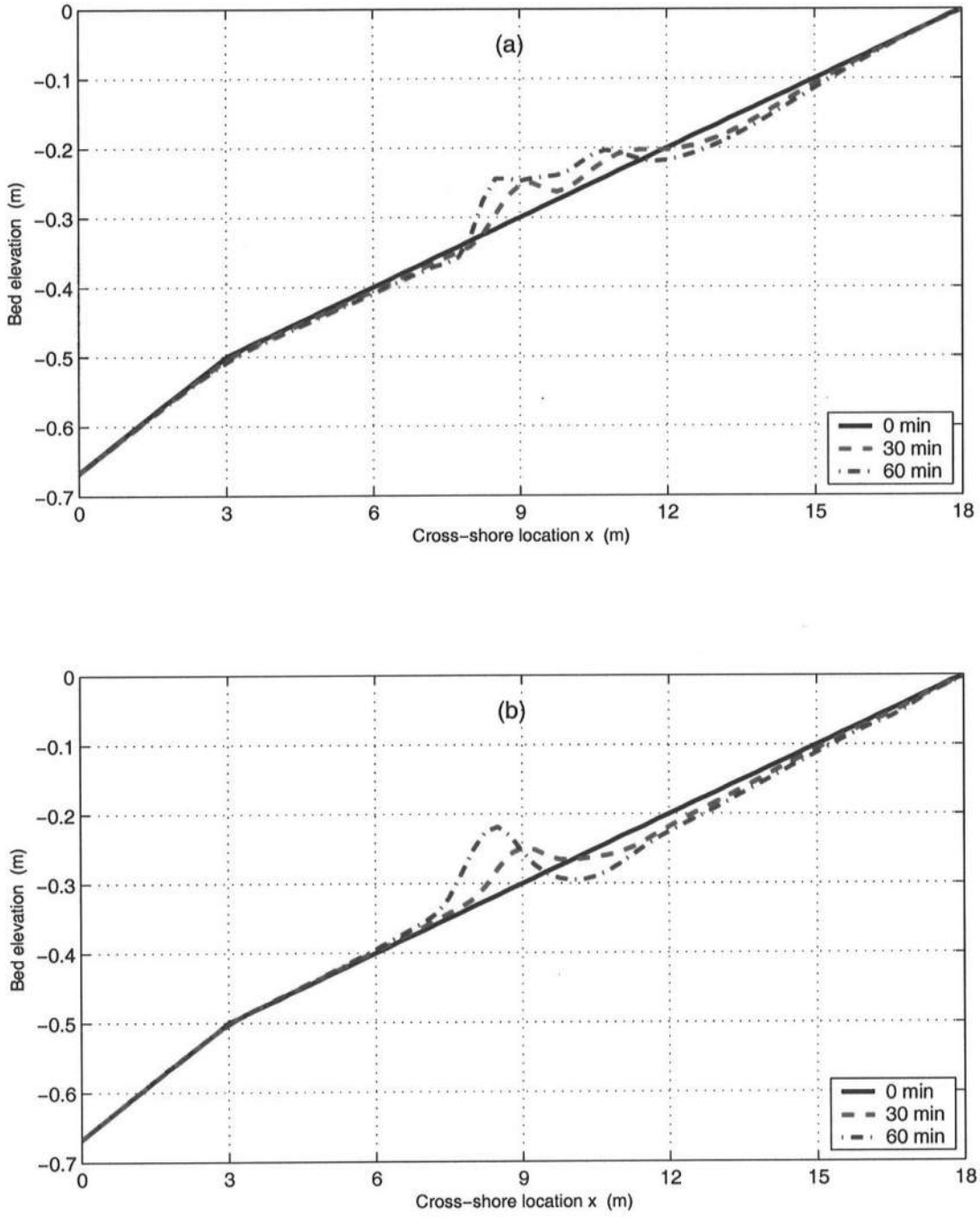

Figure 6.17: Evolutions of beach profile predicted by the diffusion-convection model: (a) using the cnoidal-bore wave model and (b) using the sinusoidal wave model

Chapter 7

COMPARISON OF SEDIMENT TRANSPORT BETWEEN THE MODEL AND THE MEASUREMENTS

This chapter is presenting the comparisons of nearshore sediment transport between the measurements in Test 1H in the LSTF and the simulated results using the present sediment diffusion-convection model combined with the SHORECIRC and the irregular wave model.

As described in Chapter 2, Test 1H in the LSTF was carried out on an initial "equilibrium" sand beach with the median grain size of 0.15 mm. Irregular waves were generated with an incident significant wave height of $0.25m$, a peak spectral wave period of 1.5 seconds and an angle of 10 degrees. In addition to the hydrodynamic measurements, the movable bed was surveyed on a regular basis, the vertical profiles of sediment concentrations were measured using the Fiber-Optic Backscatter Sensors, and the cross-shore distribution of longshore sediment transport rates was measured using the downstream sediment trapping system.

The smoothed results of the time series of wave heights and wave periods measured at $2.4\,m$ in front of the wave generator, as shown in Figure 7.1, was used as the inputs for the wave model. The beach profiles surveyed prior to the experiment were used as the initial beach bathymetry in the model.

7.1 Comparisons of Hydrodynamics

The emphasis of this chapter is to compare the predicted and measured sediment transports. Hence, only a few comparisons of hydrodynamics are presented

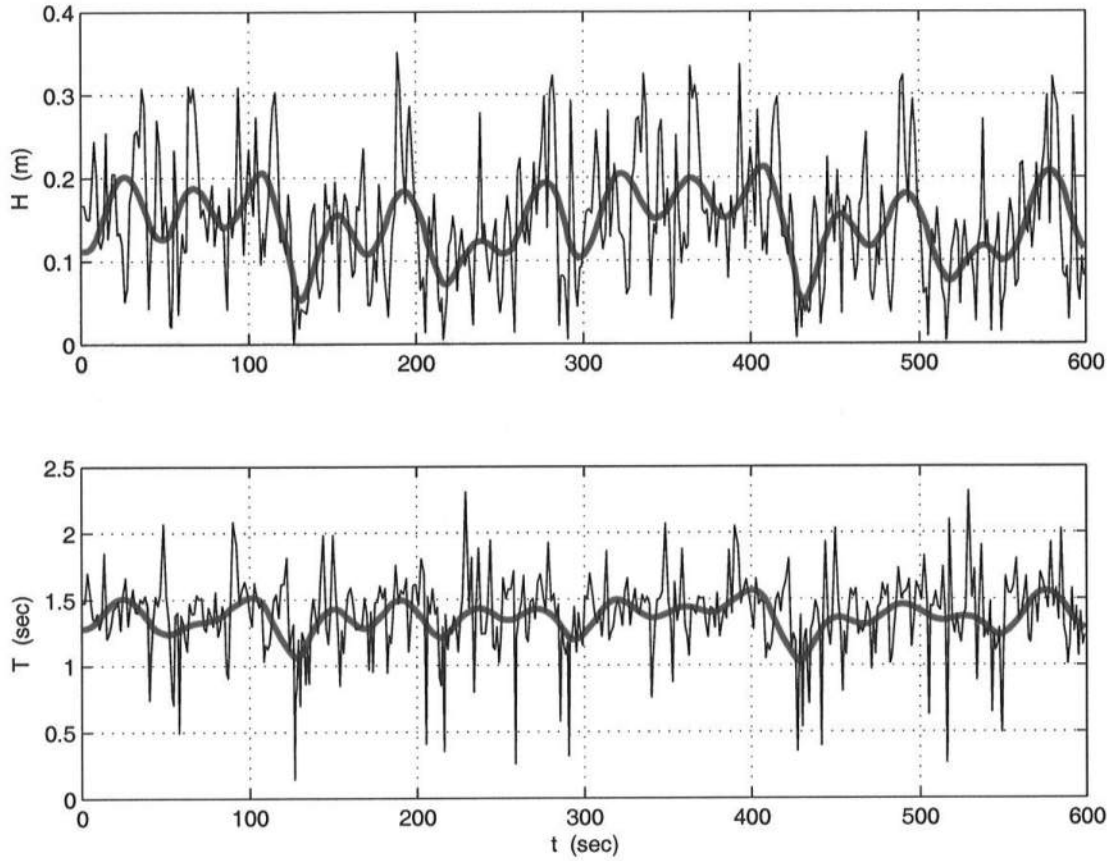

Figure 7.1: Derived temporal variations of wave heights and wave periods at $x = 2.4m$ in Test 1H (Hamilton *et al.*, 2001). The thin solid lines are the results using the zero up-crossing method, and the thick dash lines are the smoothed results which were also used as the incident wave conditions in the modeling.

herein. Figure 7.2 presents the initial beach profile as well as the comparisons of the cross-shore variations of the time-averaged wave heights, mean water levels and currents at the middle transect of the sand beach between the experiment data and model prediction. Because of the difference in the beach profiles, the cross-shore variations of the wave heights and currents in Test 1H appears to be less than those in Test 8E. It shows again the hydrodynamic model's capability of generally well predicting wave properties and circulation under irregular wave environments, as

detailed in Chapter 4. The exception is the longshore current velocity close to the shoreline. The significant longshore current measured at $x = 16.9\,m$ is considerably under-estimated by the model.

The accurate predictions of flow conditions provide a solid basis for modeling sediment transport and beach morphology change resulting from the combined wave and current flow motions.

7.2 Comparison of Longshore Sediment Transport Rates

Figure 7.3 shows the comparison for the cross-shore distribution of time-averaged longshore sediment transport rates. As both the experimental data and model prediction indicate, much stronger longshore sediment transport is found inside the surfzone as compared to the region outside the surfzone. The cross-shore distribution of the longshore sediment transport rates is much more uniform inside the surfzone under irregular wave environments as compared to those under regular environments as illustrated in Chapter 6. This is because the temporal variations of wave conditions and spatial movements of the breaking location tend to smooth out the time-averaged quantities including wave properties, wave-induced currents and the resulting sediment transport rates. In addition, the "equilibrium" beach profile also helps generate a more uniform cross-shore distribution of sediment transport rates.

The comparison shows that the present sediment model combined with the SHORECIC and the irregular wave model is capable of generally predicting the longshore sediment transport rate quite well for most of the nearshore region. An exception is for the region close to the shoreline in which the model apparently under-estimates the sediment transport rate measured in the experiment. Considering the complexity of the sediment transport under the combined wave and current flows and the typical poor accuracy shown by other sediment transport models, the relative

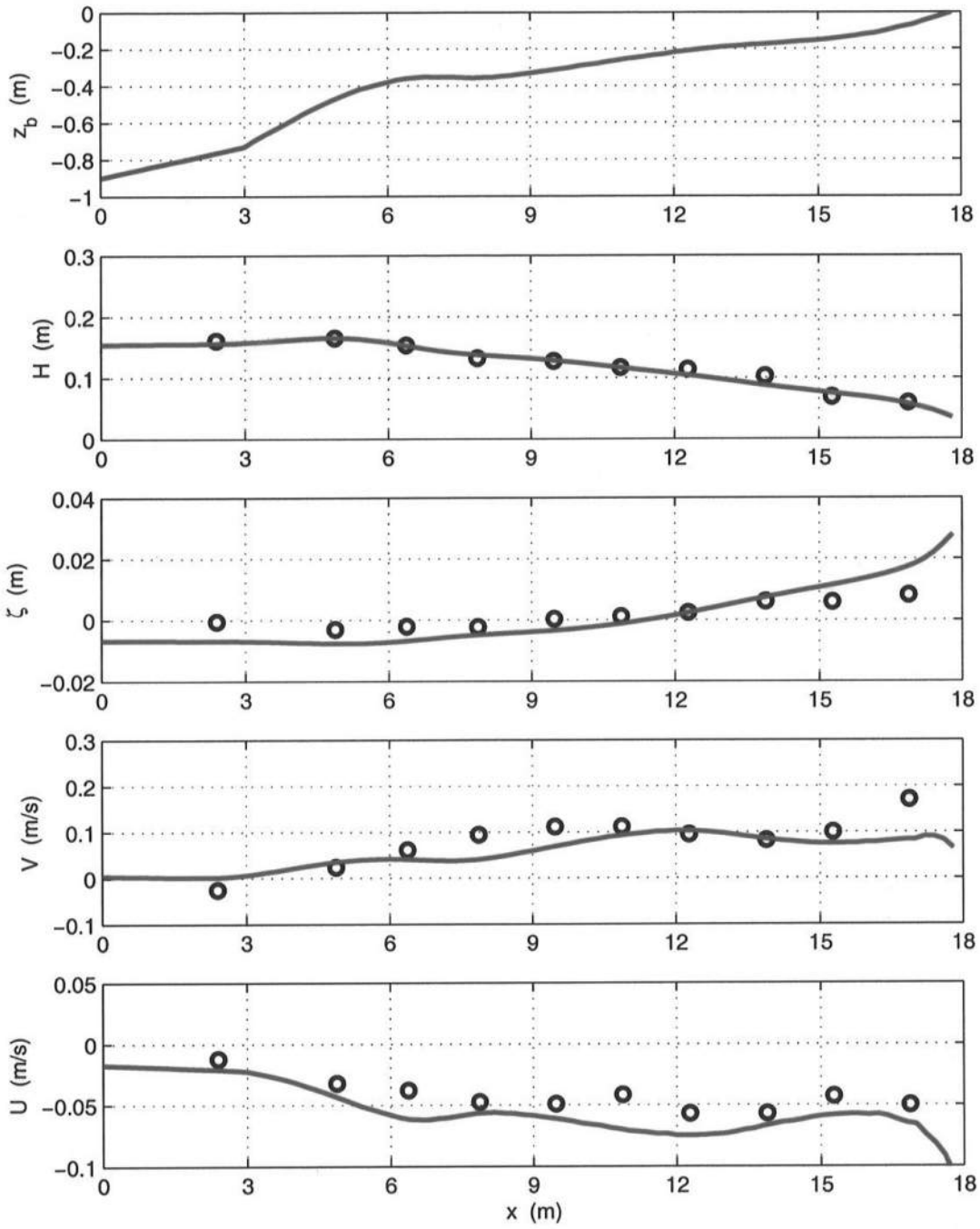

Figure 7.2: Initial beach profile (z_b) and the comparisons of the cross-shore variations of the time-averaged wave heights H, MWLs $\bar{\zeta}$ and currents $\bar{V}$ and $\bar{U}$ at y = 22.7 m between the experimental data (○) in Test 1H (Hamilton *et al.*, 2001) and model prediction (—). The still water shoreline is at $x = 17.8\,m$.

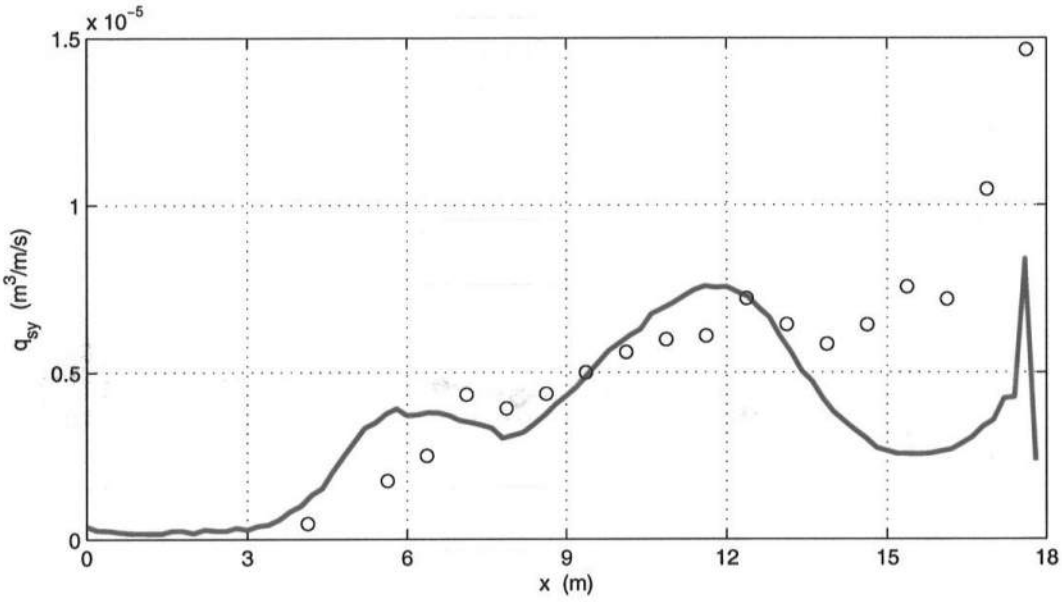

Figure 7.3: Comparison of the cross-shore distribution of time-averaged longshore sediment transport rate between the experimental data (○) in Test 1H (Hamilton and Ebersole, 2001) and model prediction (—)

good agreement between the present model and the experimental data is rather exciting.

The under-prediction of both the longshore currents and sediment transport rates close to the shoreline represents a limitation of the present wave-current-sediment transport model. Although the model prediction does show an increase in the longshore sediment transport rate close to the shoreline, the model may not be capable of accurately characterizing the extreme flow conditions and resulting intense sediment transport in inner surfzone.

7.3 Comparisons of the Vertical Profiles of Sediment Concentrations and Sediment Fluxes

Figures 7.4 to 7.10 present the comparisons of the vertical profiles of time-averaged sediment concentration $\bar{c}$ and of the product of $\bar{c}$ and longshore current velocity $\bar{V}$ for seven cross-shore locations between the experimental data and model prediction. The real longshore sediment flux $\overline{cv}$ cannot be derived from the experimental data because the time series of the sediment concentrations and of the flow velocities have not been simultaneously measured at the same location. However, as illustrated in Chapter 6, the time-averaged sediment flux $\overline{cv}$ in the longshore direction can be approximated by the value of $\bar{c}\bar{V}$ for small wave angles as the case in Test 1H.

The comparisons show that the vertical profiles of the time-averaged sediment concentrations and fluxes under irregular wave environments change more slowly in the cross-shore than those under regular waves as illustrated in Chapter 6. The model predictions generally agree with the measured vertical profiles quite well both in the concentration results and in sediment flux for most of the nearshore region.

It is also interesting to notice that the under-prediction by the model of the net longshore sediment transport rate for the inner surfzone (as e.g., at $x = 15.9\,m$ in Figure 7.3) is somewhat in contradiction with the accurate prediction of the vertical profiles of the sediment flux at the same region (as e.g., at $x = 15.3\,m$ in Figure 7.10), as the net transport rate is equivalent to the integral of the vertical profile of the time-averaged sediment flux over the water depth. This contradiction emphasizes the uncertainty and difficulty in collecting accurate sediment transport data even in laboratory experiments.

7.4 Comparisons of Cross-shore Beach Profiles

As a result of the initial "equilibrium" beach profile, the beach morphology change is limited in the experiment. As shown in Figure 7.11, only a limited accretion occurred for the region between $x = 6\,m$ and $x = 9\,m$ and a very slight erosion occurred in the inner surfzone after 3.5 hours of experiment operation. The model prediction also indicates a negligible beach profile change, as demonstrated in Figure 7.11 as well.

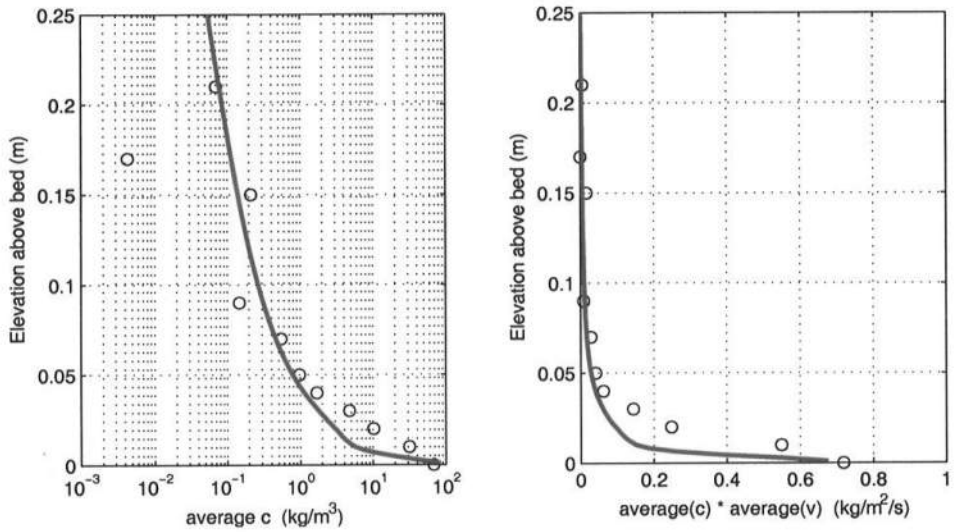

Figure 7.4: Comparisons of the vertical profiles of (a) the time-averaged sediment concentration $\bar{c}$ and (b) $\bar{c}V$ at $x = 6.4\,m$ between the experimental data ($\circ$) in Test 1H (Hamilton and Ebersole, 2001) and model prediction (—)

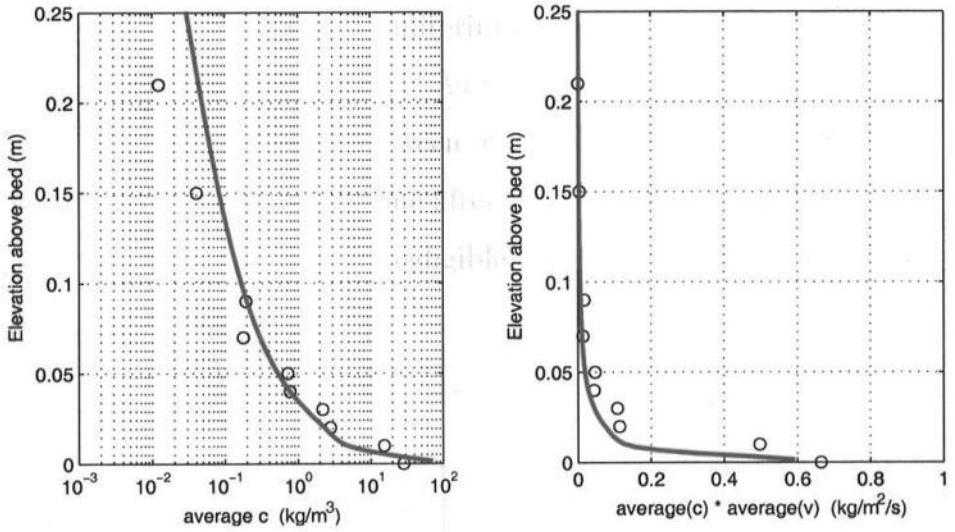

Figure 7.5: Comparisons of the vertical profiles of (a) the time-averaged concentration $\bar{c}$ and (b) $\bar{c}V$ at $x = 7.9\,m$ between the experimental data ($\circ$) in Test 1H (Hamilton and Ebersole, 2001) and model prediction (—)

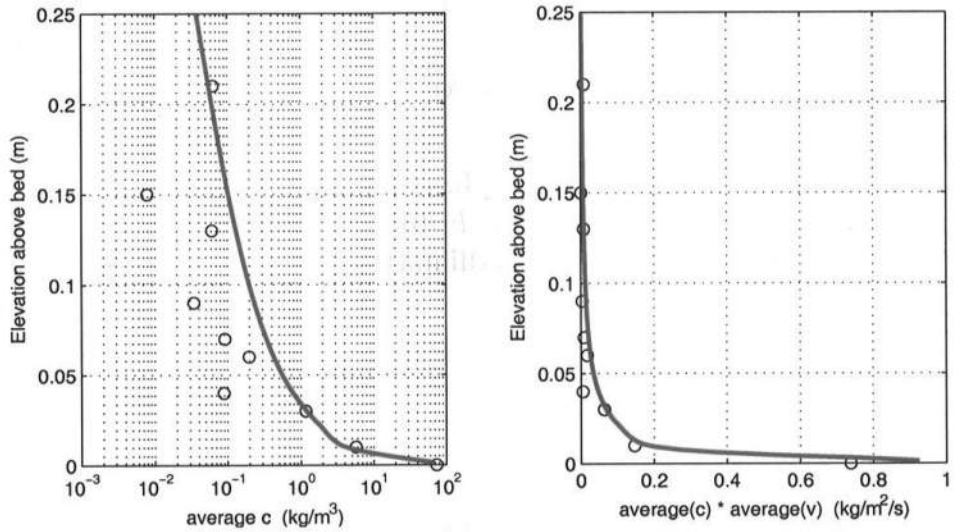

Figure 7.6: Comparisons of the vertical profiles of (a) the time-averaged concentration $\bar{c}$ and (b) $\bar{c}V$ at $x = 9.5\,m$ between the experimental data ($\circ$) in Test 1H (Hamilton and Ebersole, 2001) and model prediction (—)

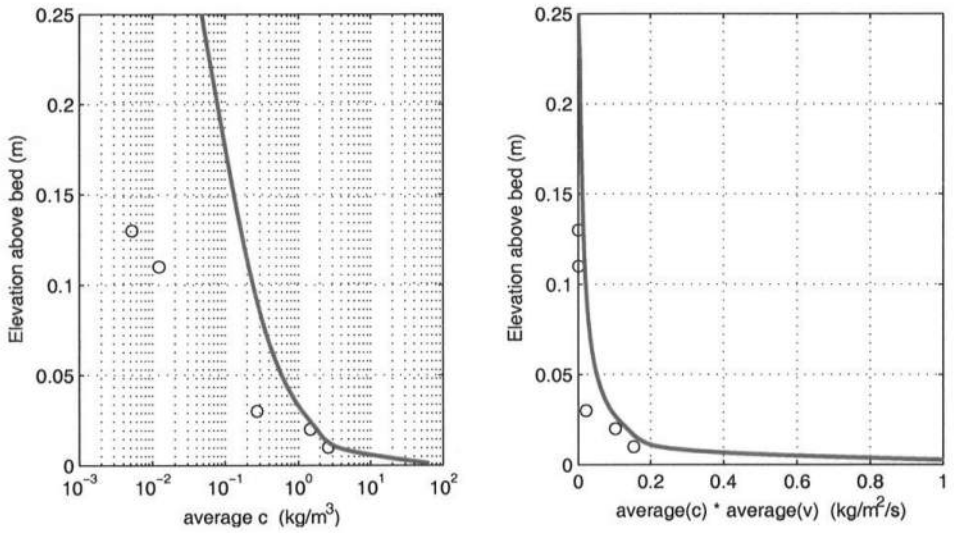

Figure 7.7: Comparisons of the vertical profiles of (a) the time-averaged concentration $\bar{c}$ and (b) $\bar{c}V$ at $x = 10.9\,m$ between the experimental data ($\circ$) in Test 1H (Hamilton and Ebersole, 2001) and model prediction (—)

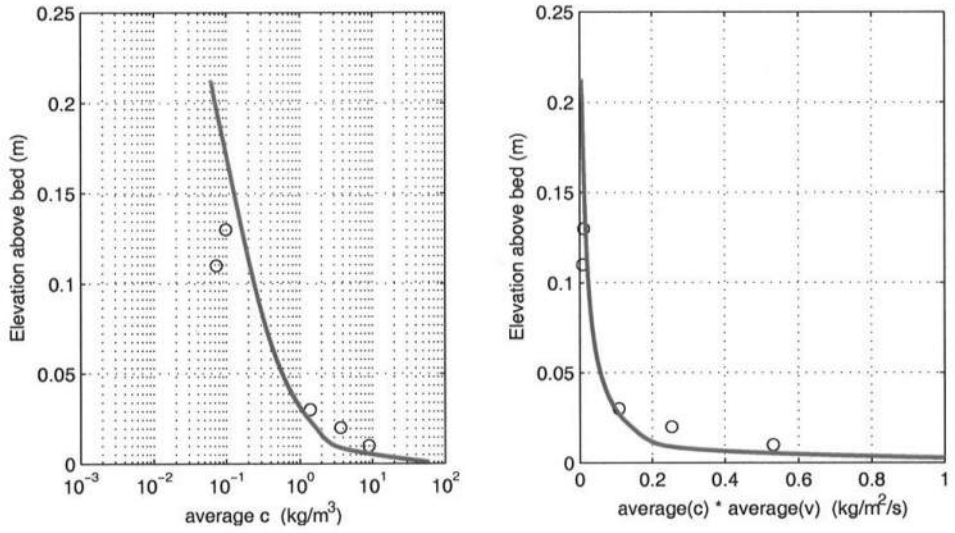

Figure 7.8: Comparisons of the vertical profiles of (a) the time-averaged concentration $\bar{c}$ and (b) $\bar{c}V$ at $x = 12.3\,m$ between the experimental data ($\circ$) in Test 1H (Hamilton and Ebersole, 2001) and model prediction (—)

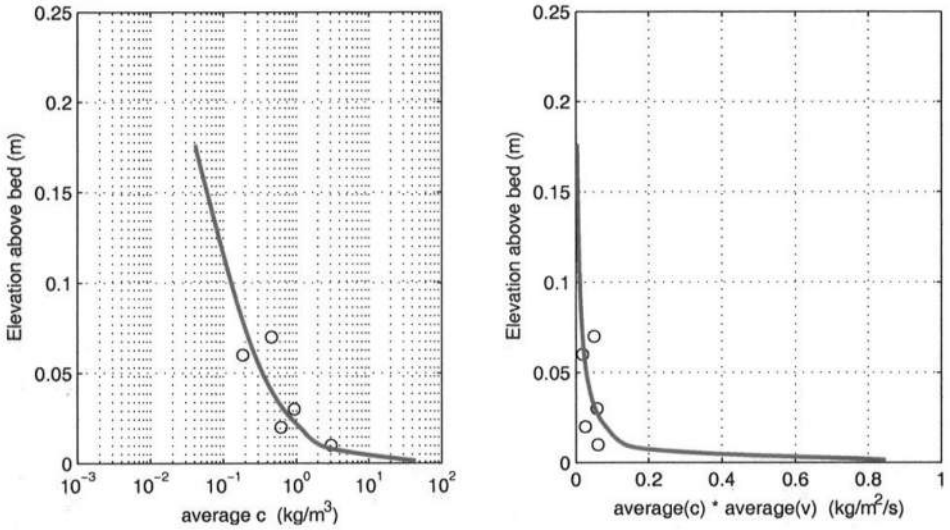

Figure 7.9: Comparisons of the vertical profiles of (a) the time-averaged concentration $\bar{c}$ and (b) $\bar{c}V$ at $x = 13.9\,m$ between the experimental data ($\circ$) in Test 1H (Hamilton and Ebersole, 2001) and model prediction (—)

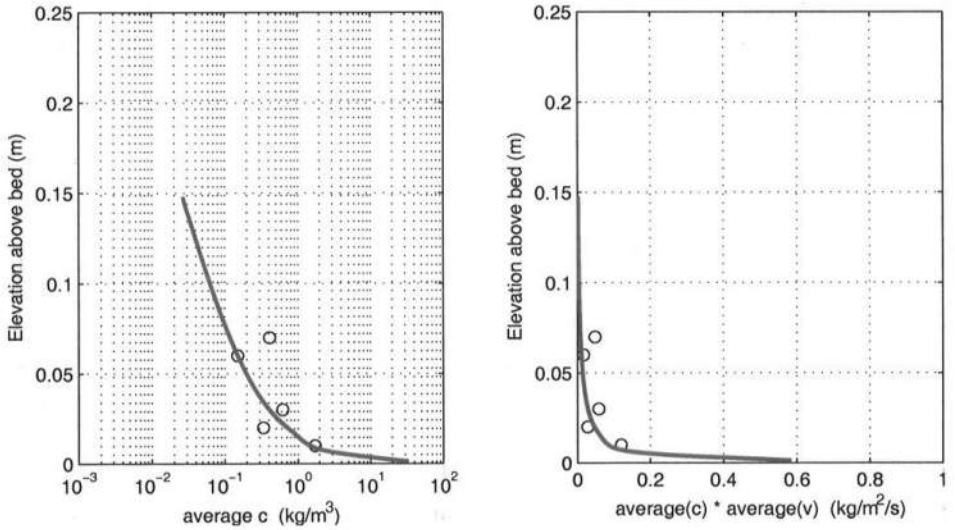

Figure 7.10: Comparisons of the vertical profiles of (a) the time-averaged concentration $\bar{c}$ and (b) $\bar{c}V$ at $x = 15.3\,m$ between the experimental data ($\circ$) in Test 1H (Hamilton and Ebersole, 2001) and model prediction (—)

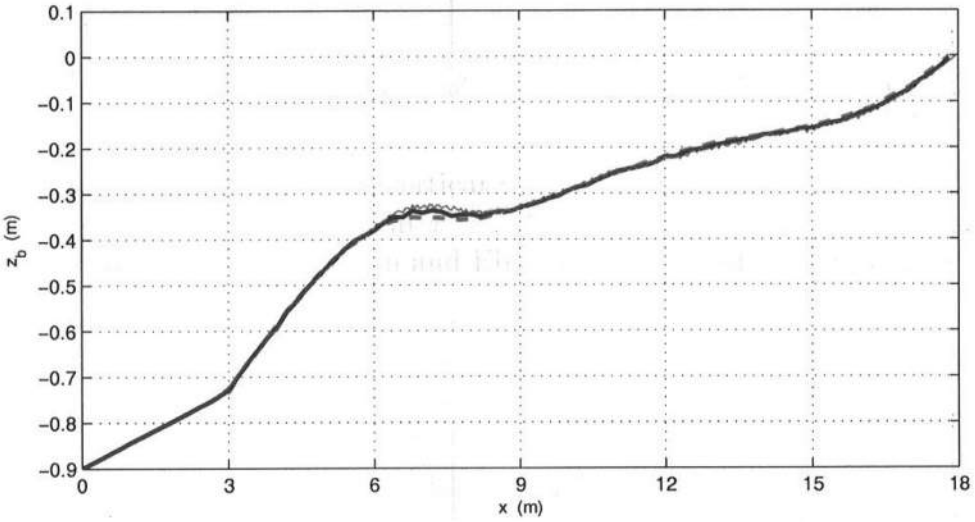

Figure 7.11: Comparison between the initial beach profile (−−) and the beach profile after 3.5 hours surveyed in Test 1H (thin —) in the LSTF (Hamilton and Ebersole, 2001) and predicted by the model (thick —)

Chapter 8

CONCLUSIONS

A nearshore sediment transport model has been developed for the bedload mode and the suspended load mode as well as the nearshore morphology changes, and kinematic wave models have been developed for the transformations of both (sinusoidal and non-sinusoidal) regular and irregular waves. By incorporating the sediment transport model and wave models in the SHORECIRC, a realistic coupled wave-current-sediment transport model is developed for nearshore processes involving wave transformations, wave-driven circulation, and resulting sediment transport and beach evolution. This model was tested primarily through the comparisons against the comprehensive experimental measurements carried out in the LSTF at CHL. Characteristics of nearshore hydrodynamics and sediment transport under regular and irregular wave environments and the effects of wave models on the computed wave-induced circulation and sediment transport were also investigated by analyzing the model predictions and comparisons.

8.1 Modeling Wave Characteristics and Nearshore Hydrodynamics

The wave models developed for both regular and irregular waves are based on the kinematic ("energetic") approach. One regular-wave model uses sinusoidal waves for the phase motion and the other uses non-sinusoidal waves (i.e., cnoidal waves outside the surfzone and empirical relations inside the surfzone). The irregular wave model uses either sinusoidal or non-sinusoidal waves depending on the local wave condition (as e.g., the Ursell Number). The SHORECIRC using these models

as wave drivers is capable of predicting nearshore hydrodynamics induced by regular or irregular, sinusoidal or non-sinusoidal waves.

The comparisons of the wave-current model includes the entire range of nearshore parameters from wave heights, phase speeds, wave peakedness, wave-averaged forcing for circulation, mean water levels, to depth-averaged quantities and depth variations of both longshore and cross-shore currents. The predicted temporal variations of wave-averaged wave heights, mean water levels and currents compared with the irregular wave experiments are also presented.

The extensive comparisons against the regular wave experiments make it possible to address two essential questions: (1) how well does a simple sinusoidal-wave based model perform in comparison to a model that better represents the actual shape of the wave motion? And (2) how important are the inaccuracies of a wave model for reproducing the 3-D current patterns in the nearshore. The main conclusions may be summarized as follows:

- As expected the sinusoidal wave model grossly underestimates the wave height increase towards breaking and consequently predicts a weaker decay of wave height inside the surfzone. It is also incapable of predicting the increases of c^2/gh and wave peakedness (as e.g., η_c/H) towards breaking and decays inside the surfzone. However, the nonlinear cnoidal-bore wave model picks up the cross-shore variations of wave height, c^2/gh and wave peakedness remarkably well.

- In spite of these deficiencies, however, the two wave models incorporated in the SC predict almost equally well the cross-shore variations of mean water levels and longshore currents with only a limited advantage to the cnoidal-bore wave driver. The explanation for this is that near breaking the sine waves are more "bulky" in shape than real waves. The accurate predictions of the setup and longshore currents imply that the variations of radiation stresses are well

represented by both models. This clearly has important consequences for the capability of the models to function as forcing mechanisms for the generation of nearshore currents.

- The cross-shore undertow currents are primarily determined by the wave volume flux for which the phase velocity plays an important role. The comparisons show the deficiency in the sinusoidal wave model, which over-predicts the wave volume flux and cross-shore currents before and after breaking as a result of the failure to predict the substantial increase in phase speed around breaking. The SC using the cnoidal-bore wave driver, however, predicts the wave volume fluxes and most of the undertow profiles quite well.

- In all it appears that while the sinusoidal wave model performs surprisingly well for the mean water levels and longshore currents its weakness lies in the prediction of cross-shore motion, while the cnoidal-bore based model shows a more uniformly reliable performance.

- Measures of the overall model skills have been shown for some of the variables in the form of cross-shore averaged rms-values of the errors. Such measures can give convenient one-number indications of the deviations from the measured values. However, comparison with the figures showing the details of the variations over the cross-shore reveals that such simple numbers for the skills can both be unduly influenced by large local scatter of the measurements and hide positive details of model performance.

The comparisons with the irregular wave experiments illustrate two issues: (1) the differences of wave characteristics and wave-induced currents between regular and irregular waves, and (2) the capability of the kinematic wave model to represent the actual hydrodynamics induced by irregular waves. The primary conclusions are summarized as follows:

- Because of the temporal variations of the properties of irregular waves and the resulting spatial movements of the breaking location, the cross-shore variations of the wave parameters (as e.g., wave height) and wave-induced currents (averaged over the wave-group cycle) for irregular waves are less significant than those for regular waves, as shown in the experimental data and in the model predictions as well.

- The present irregular wave model incorporated with the SC is capable of well predicting the wave-group averaged wave height, mean water level, depth-averaged quantities and depth variations of wave-induced currents under irregular wave environments.

- The coupled wave-current model is also capable of predicting the temporal variations of the wave height as well as the mean water level and wave-induced currents. However, because of the slowly varying wave assumption of the kinematic approach, the irregular incident wave conditions need to be smoothed before being used as the input for the wave model and thus the model predicts less significant temporal variations than the measurements indicate.

8.2 Modeling Nearshore Sediment Transport and Beach Evolution

A sediment transport model has been developed to incorporate with the wave models and the SC. The sediment transport model calculates transport rates of bedload and suspended load in both the cross-shore and longshore directions as well as the resulting beach morphology change, which would feed back to the wave and current models.

After a review of the theoretical background of the two-phase flow theory, a formula is derived for bedload transport rate starting from the two-phase flow theory. This formula appears to be the improved version for both the Bailard and Inman (1981a) formula and Engelund and Fredsøe (1976) formula. Two approaches

has been developed in this study for suspend sediment transport. The simpler one is to modify the Bailard (1981b) formula to include the effect of wave breaking on suspended sediment transport rate, and the other is to develop a detailed physics-based phase-resolving diffusion-convection model for sediment suspension.

A presumed simple case, which is sediment transport on a plane beach under combined regular-wave and current flows, was simulated using the developed wave-current-sediment transport model system and extensive prediction results were presented and analyzed. The purpose is to test the behavior of the present models, analyze the effects of the primary factors on sediment transport, and illustrate some characteristics of nearshore sediment transport which are difficult to detect in experiments. Some major conclusions can be described as follows:

- Because both the Bailard and Inman (1981a) formula and the Engelund and Fredsøe (1976) formula for bedload transport rate can be derived from the two-phase flow theory and the major difference is the value of the bedload efficiency coefficient, both formulas predict similar shapes but somewhat different magnitudes of the cross-shore distributions of bedload transport rates. The present bedload formula theoretically improves the Bailard and Inman (1981a) formula by including the effect of the critical bottom shear stress and the Bailard and Inman (1981a) formula by correctly addressing the effect of the bottom slope, though it only predicts a slightly different bedload transport rates as compared to the two formulas.

- The suspended sediment transport rate predicted by the physics-based diffusion-convection model shows significant difference both in variation and in magnitude of the transport rate from those obtained by the original or modified version of the Bailard (1981b) formula that is based on a simple energetic approach. In addition, after including the effect of wave breaking the modified

version of the Bailard (1981b) formula predicts a much more intense suspended sediment transport inside the surfzone than the original formula does.

- The wave asymmetry about the horizontal axis plays an important role in inducing net nearshore sediment transport in the direction of wave propagation, i.e., the shoreward and downstream direction. Depending on the balance between the wave asymmetry and cross-shore currents, the net cross-shore sediment transport can be shoreward outside the surfzone where undertow currents are weak, and turns to seaward inside the surfzone as waves become less peaked and undertow becomes stronger. The present sediment transport model appears to be capable of well representing this effect of wave asymmetry if incorporated with the cnoidal-bore wave model but fails if using the sinusoidal wave model.

- Wave motions contribute to sediment transport not only by inducing net transport in the wave direction because of the wave asymmetry but also by intensifying sediment entrainment from the bed and suspension in the water column and thus providing more sediment for wave-induced currents to transport. It is also found that for small wave angles the net longshore sediment transport flux can be approximated by the product of the time-averaged concentration and longshore current velocity because of the small contribution from the longshore component of the oscillatory wave velocity and wave asymmetry.

- The wave breaking process intensifies the flow turbulence and thus sediment suspension inside the surfzone. Due to the combined effects of wave breaking and significantly increased wave-induced currents, the vertical distribution of suspended sediment is more uniform and a larger transport rate is predicted in the mid surfzone.

- The sediment convection caused by the vertical flow velocity in oscillatory flows is included in the diffusion-convection model. The model shows that the vertical flow velocity in combined wave and current flows tends to intensify sediment suspension and this effect appears to be more eminent for the upper water column outside the surfzone where the vertical flow velocity is relatively large but the flow turbulence and thus sediment diffusion are weak. The comparisons reveal that a more significant temporal variation and a more uniform vertical (logarithmic) distribution of sediment concentrations are predicted by the diffusion-convection model for the region outside the surfzone. However, because of the rapid decay of sediment concentration in the vertical direction, only a slight or even indistinguishable difference is found in the predicted net transport rates between the diffusion model and the diffusion-convection model.

- The effects of two bottom boundary conditions on predicted sediment suspension were examined. The instantaneous bottom sediment concentration appears to have a much more significant temporal variation when specifying the bottom reference concentration than when the pickup function is specified. The comparisons reveal that the model applying the bottom reference concentration boundary condition predicts a larger wave-averaged sediment concentration at the bottom but at the same time a faster vertical decay in the near-bottom and thus predicts a net suspended sediment transport rate surprisingly close to that obtained by the model applying the pickup function for the test case.

- As a result of the significant vertical and cross-shore variations of sediment concentrations and wave-induced currents, the predicted wave-averaged sediment flux per unit area (i.e., $\bar{c}\vec{u}$) shows even more significant variations vertically and in the cross-shore direction, not only in magnitudes but also in directions.

- Spatial variations of net sediment transport rates induce beach morphology change, and the cross-shore sediment transport plays a primary role in beach profile evolutions for a straight parallel beach. As model prediction shows, an initial plane beach would gradually evolve to a beach with a sand bar formed around the breaking and with a general erosion in the middle and inner surfzone as a result of the cross-shore variation of the net cross-shore sediment transport rates. The beach profiles predicted by the sediment transport model using different wave models also show some differences in the location and size of the breaker bar, slight beach evolution outside the surfzone and the width of the erosion area inside the surfzone.

The wave-current-sediment transport model was tested against an experiment (Test 1H) of sediment transport on an "equilibrium" beach under irregular wave environments in the LSTF. From the comparisons some conclusions may be summarized as follows:

- As compared to sediment transport on a plane beach under regular wave environments, less significant cross-shore variations of wave-induced currents and longshore sediment transport rates are found in the experiment of sediment transport on an "equilibrium" beach under irregular waves. This is predicted by the model as well. The less cross-shore variations result from the "equilibrium" beach profile, temporal variations of (irregular) wave conditions and spatial variations of the wave breaking location.

- The Comparisons between the experiment data and model prediction reveal that the phase resolving sediment diffusion-convection model and irregular wave model incorporated with the SHORECIRC is capable of predicting reasonably well the nearshore circulation, longshore sediment transport rates and vertical profiles of sediment concentration and fluxes under irregular wave environments.

- As a result of the initial "equilibrium" beach profile in the experiment the beach morphology change is negligible. The model also predicts a negligible beach evolution. This somehow illustrates the capability of present model of predicting cross-shore sediment transport and beach morphology change.

- However, the significant longshore sediment transport rate measured in the experiment in the inner surfzone is apparently under-estimated by the model. This could be because sediment transport is under sheet flow condition close to the shoreline that is out of the capability of the current model.

8.3 Limitations of This Study

There are a number of limitations in this study that should be addressed as a means for improvement or potential strategies for further study. Some of the limitations are due to the formulation and methodology we used in this study, but most of them are due to the status of the present (limited) understanding of the coastal hydrodynamics and sediment transport. The main limitations of this study include:

- The wave models developed in this study are limited to a straight beach with parallel contour, and cannot be applied to a beach with a significant bathymetry variation in the longshore direction.

- The criterion for wave breaking still remains quite uncertain for both regular and irregular waves. The location of wave breaking for regular waves was determined by comparing the predicted wave height with experimental data. The simple breaking criterion we used for an individual wave within an irregular wave group seems not to work well for all the individual waves.

- There is no wave theory that is appropriate for describing surfzone waves, and thus the phase variation of surfzone waves was represented by some empirical formulations in this study.

- While the wave and circulation models were tested using extensive experimental data, the sediment transport model was only tested with one experiment (Test 1H) in the LSTF. Because of the complexity of nearshore sediment transport, it is crucial to compare the model with more experimental measurements.

- The wave-current-sediment transport model seems to be incapable of well predicting the significant longshore current and sediment transport rate that were measured close to the shoreline in Test 1H (sediment transport under irregular waves) in the LSTF.

- The effects of coastal bedforms such as ripples on hydraulic roughness and sediment transport are not directly addressed in the model. A larger bottom friction coefficient (caused by the ripples) was used for the sandy beach test (Test 1H) in order to match the reduced current as compared to that for the concrete beach tests (Test 6N and Test 8E). However, the effect of ripples on sediment suspension, which is believed to be sometimes important, is not included in the model.

Bibliography

Ahilan, R. V. and Sleath, J. F. A. (1987). Sediment transport in oscillatory flow over flat bed. *J. Hydraulic Eng.*, **113**(3), 308–322.

Andersen, K. H. (1999). The dynamics of ripples beneath surface waves and topics in shell models of turbulence. Technical Report Ph.D Thesis, Inst. Hydrodyn. Hydraul. Eng. (ISVA), Tech. Univ. Denmark, Lyngby.

Asano, T. (1990). Two phase flow model on oscillatory sheet-flow. In *Proc. 22nd Coastal Engineering Conference*, pages 2372–2384. ASCE.

Bagnold, R. A. (1954). Experiments on a gravity-free dispersion of large solid spheres in a newtonian fluid under shear. *Proc. Roy. Soc. Lond.*, **A225**, 49–63.

Bagnold, R. A. (1956). The flow of cohesionless grains in fluids. *Roy. Soc. Lond. Philos. Trans.*, **249**(964), 235–297.

Bagnold, R. A. (1963). Mechanics of marine sedimentation. In *The sea: ideas and observations*, New York. Vol. 3, Interscience.

Bagnold, R. A. (1966). An approach to the sediment transport problem from general physics. Technical Report Prof. Pap. 422-1, U.S. Geol. Sur., Washington D.C.

Bailard, J. A. (1981b). An energetics total load sediment transport model for a plane sloping beach. *J. Geophys. Res.*, **86**(c11), 10938–10954.

Bailard, J. A. and Inman, D. L. (1981a). An energetics bedload model for a plane sloping beach: local transport. *J. Geophys. Res.*, **86**(c3), 2035–2043.

Battjes, J. A. (1975). Modelling of turbulence in the surfzone. paper presented at symposium on modelling techniques. In *Symposiums on Modelling Techniques*, San Francisco, California. ASCE.

Battjes, J. A. (1988). Surf zone dynamics. *Annual Reviews Fluid Mechanics*, **20**, 257–293.

Bowen, A. J. (1980). Simple models of nearshore sedimentation: Beach profiles and longshore bars. In *The coastline of Canada*, pages 1–11, Geological Survey of Canada, Ottawa.

Brevik, I. (1981). Oscillatory rough turbulent boundary layers. *J. of Wtrwyy., Port, Coast. and Oc. Engng.*, **107**(WW3), 175–188.

Christoffersen, J. B. and Jonsson, I. G. (1985). Bed friction and dissipation in a combined current and wave motion. *J. Coastal Engineering*, **12**(5), 387–423.

Coffey, P. C. and Nielsen, P. (1984). Aspects of wave current boundary layer flows. In *Proc. 19th Coastal Engineering Conference*, pages 2232–2245. ASCE.

Cox, D. T. and Kobayashi, N. (1997). Kinematic undertow model with logarithmic boundary layer. *J. of Wtrwyy., Port, Coast. and Oc. Engng.*, **123**(6), 354–360.

Cox, D. T., Kobayashi, N., and Okayasu, A. (1995). Experimental and numerical modeling of surfzone hydrodynamics. Technical Report CACR-95-07, University of Delaware.

Davies, A. G., Ribberink, J. S., Temperville, A., and Zyserman, J. A. (1997). Comparisons between sediment transport models and observations made in wave and current flows above plane beds. *J. Coastal Engineering*, **31**, 163–198.

De Vriend, H. J. and Stive, M. J. F. (1987). Quasi-3d modelling of nearshore currents. *J. Coastal Engineering*, **11**, 565–601.

Dean, R. G. (1977). Equilibrium beach profiles: U.s.atlantic and gulf coasts. Technical Report CACR-77-12, Center for Applied Coastal Research, Univ. of Delaware.

Dong, P. and Zhang, K. (1999). Two-phase flow modelling of sediment motions in oscillatory sheet flow. *J. Coastal Engineering*, **36**, 87–109.

Dongeren, A. R. V., Sancho, F. E., Svendsen, I. A., and Putreva, U. (1994). Shorecirc: A quasi 3-d nearshore model. In *24th Coastal Engineering Conference*, pages 2741–2754, Kobe. ASCE.

Drew, D. A. (1983). Mathematical modeling of two-phase flow. *Annual Reviews Fluid Mechanics*, **15**, 261–291.

Engelund, F. and Fredsøe, J. (1976). A sediment transport model for straight alluvial channels. *Nordic Hydraology*, (7), 293–306.

Engelund, F. and Fredsøe, J. (1982). Hydraulic theory of alluvial rivers. *Adv. Hydrosci*, (13), 187–215.

Fredsøe, J. and Deigaard, R. (1992). *Mechanics of Coastal Sediment Transport*. World Scientific Publishing.

Fredsøe, J., Andersen, O. H., and Silberg, S. D. (1985). Distribution of suspended sediment in large waves. *J. of Wtrwyy., Port, Coast. and Oc. Engng.*, **111**(6), 1041–1059.

Garcez-Faria, A. F., Thornton, E. B., Stanton, T. P., Soares, C. V., and Lippmann, T. C. (1998). Vertical profiles of longshore currents and related bed shear stress and bottom roughness. *J. Geophys. Res.*, **103**, 3217–3232.

Garcez-Faria, A. F., Thornton, E. B., Lippmann, T. C., and Stanton, T. P. (2000). Undertow over a barred beach. *J. Geophys. Res.*, **105**, 16999–17010.

Glenn, S. M. (1983). A continental shelf bottom boundary layer model: The effects of waves, currents, and a moveable bed. Technical Report Sc.D. thesis, Mass. Inst. of Technol., Cambridge.

Glenn, S. M. and Grant, W. D. (1987). A suspended sediment stratification correction for combined wave and current flows. *J. Geophys. Res.*, **92**(c8), 8244–8264.

Grant, W. D. and Madsen, O. S. (1979). Combined wave and current interaction with a rough bottom. *J. Geophys. Res.*, **84**(c4), 1979–1808.

Grant, W. D. and Madsen, O. S. (1986). The continental shelf bottom boundary layer. *Annual Reviews Fluid Mechanics*, **18**, 265–305.

Haas, K. A. and Svendsen, I. A. (2000). Three-dimensional modelling of rip current systems. Technical Report CACR-00-06, Center for Applied Coastal Research, Univ. of Delaware.

Haas, K. A., Svendsen, I. A., and Zhao, Q. (2000). 3D modeling of rip currents. In *Proc. 27th Coastal Engineering Conference*, volume 2, pages 1113–1126, Sydney. ASCE.

Hamilton, D. G. and Ebersole, B. A. (2001). Establishing uniform longshore currents in a large-scale sediment transport facility. *J. Coastal Engineering*, **42**(3), 199–218.

Hamilton, D. G., Ebersole, B. A., Smith, E. R., and Wang, P. (2001). Development of a large-scale laboratory facility for sediment transport research. Technical Report ERDC/CHL TR-01-22, U.S. Army Engineer Research and Development Center.

Hanes, D. M. and Inman, D. L. (1985). A dynamic yield criterion for granular-fluid flows. *J. Geophys. Res.*, **90**(b5), 3670–3674.

Hansen, J. B. (1990). Periodic waves in the surfzone: analysis of experimental data. *J. Coastal Engineering*, **14**, 19–41.

Hansen, J. B. and Svendsen, I. A. (1979). Regular waves in shoaling water experimental data. Technical Report Ser. Pap., 21, Inst. Hydrodyn. Hydraul. Eng. (ISVA), Tech. Univ. Denmark, Lyngby.

Hattori, M. and Aono, T. (1985). Experimental study on turbulence structures under spilling breakers. In *The Ocean Surface*, pages 419–424, D. Reidel, Hingham, Mass. edited by Y. Toba and H. Mitsuyasu.

Hsu, T.-J., Jenkins, J. T., and Liu, P. L.-F. (2003). On two-phase sediment transport: Dilute flow. *J. Geophys. Res.*, **108**(c3), 3057–3070.

Jonsson, I. G. (1963). Measurements in the turbulent wave boundary layer. In *10th Congr. Int. Ass. Hydr. Res.*, pages Vol 1, 85–92, London.

Jonsson, I. G. (1967). Wave boundary layers and friction factors. In *10th Coastal Engineering Conference*, pages Vol 1, 127–148, Tokyo. ASCE.

Jonsson, I. G. and Carlsen, N. A. (1976). Experimental and theoretical investigations in oscillatory turbulent boundary layer. *J. Hydraulic Eng.*, **14**(1), 45–60.

Kajiura, K. (1968). A model of the bottom boundary layer in water waves. Technical Report 46, 75-123, Bull. Earthquake Res. Inst.

Kirby, J. T. and Dalrymple, R. A. (1994). Combined refraction/diffraction model ref/dif1, version 2.5. Technical Report CACR-92-22, University of Delaware.

Kobayashi, N. and Johnson, B. D. (2001). Sand suspension, storage, advection, and settling in surf and swash zones. *J. Geophys. Res.*, **106**(c5), 9363–9376.

Kobayashi, N. and Seo, N. S. (1985). Fluid and sediment interaction over a plane bed. *J. Hydraulic Eng.*, **111**(6), 903–921.

Li, L. and Sawamoto, M. (1995). Multi-phase model on sediment transport in sheet-flow regime under oscillatory flow. *J. Coastal Engineering Jpn.*, **38**(2), 157–178.

Li, Z. and Davis, A. G. (1996). Towards predicting sediment transport in combined wave-current flow. *J. of Wtrwyy., Port, Coast. and Oc. Engng.*, **122**(4), 157–164.

Nadaoka, P. A. and Kondoh, T. (1982). Laboratory measurements of velocity field structure in the surf zone by ldv. *J. Coastal Engineering Jpn.*, **25**, 125–146.

Nielsen, P. (1992). *Coastal Bottom Boundary Layers and Sediment Transport*. World Scientific Publishing.

Nielsen, P., Svendsen, I. A., and Staub, C. (1978). Onshore-offshore sediment movement on a beach. In *16th Coastal Engineering Conference*, pages 1475–1492, Hamburg. ASCE.

Okayasu, A., Shibayama, T., and Horikawa, K. (1980). Velocity and pressure field in spilling breakers. In *17th Coastal Engineering Conference*, pages 547–566, Sydney. ASCE.

Okayasu, A., Shibayama, T., and Horikawa, K. (1988). Vertical variation of undertow in the surfzone. In *21st Coastal Engineering Conference*, pages 478–491. ASCE.

Ono, M., Deguchi, I., and Sawaragi, T. (1996). Numerical modelling of sediment transport for various mode. In *25th Coastal Engineering Conference*, pages 3888–3900, Orlando. ASCE.

Özkan-Haller, H. T. and Kirby, J. T. (1999). Nonlinear evolution of shear instabilities of the longshore current: A comparison of observations and computations. *J. Geophys. Res.*, **104**(c11), 25953–25984.

Peyret, R. and Taylor, T. D. (1982). *Computational Methods for Fluid Flow*. Springer-Verlag, New York.

Phillips, O. M. (1969). *The Dynamics of the Upper Ocean*. Cambridge University Press.

Press, W. H., Vetterling, W. T., Teukolsky, S. A., and Flannery, B. P. (1986). *Numerical recipes*. Cambridge University Press.

Putrevu, U. and Svendsen, I. A. (1993). Vertical structure of the undertow outside the surf zone. *J. Geophys. Res.*, **98**(c12), 22707–22716.

Putrevu, U. and Svendsen, I. A. (1994). Nearshore mixing and dispersion. *J. Geophys. Res.*, **A445**, 561–576.

Rakha, K. A., Deigaard, R., and Brøker, I. (1997). A phase-resolving cross shore sediment transport model for beach profile evolution. *J. Coastal Engineering*, **31**, 231–261.

Reniers, A. J. H. M., Thornton, E. B., and Lippman, T. C. (1995). Longshore currents over barred beaches. In *Coastal Dynamics'95*, pages 413–424, Gdansk. ASCE.

Ribberink, J. S. and Al-Salem, A. A. (1995). Sheet flow and suspension of sand in oscillatory boundary layers. *J. Coastal Engineering*, **25**, 205–225.

Rijn, L. C. V. (1984). Sediment pickup function. *J. Hydraulic Eng.*, **110**(10), 1494–1502.

Roelvink, J. A. and Stive, M. J. F. (1989). Bar-generating cross-shore flow mechanisms on beach. *J. Geophys. Res.*, **94**(c4), 4785–4800.

Sanchez-Arcilla, A. F., Collado, A. F., and Rodriguez, A. (1992). Vertically varying velocity field in q-3d nearshore circulation. In *23rd Coastal Engineering Conference*, pages 2811–2834, Venice. ASCE.

Sancho, F. and Svendsen, I. A. (1997). Unsteady nearshore currents on longshore varying topographies. (Ph. D. Dissertation), Res. Report CACR-97-10, Center for Applied Coastal Research, Univ. of Delaware.

Savage, S. B. and McKeown, S. (1983). Shear stresses developed during rapid shear of concentrated suspension of large spherical particles between concentric cylinders. *J. Fluid Mech.*, **127**, 453–472.

Schäffer, H. A., Madsen, P. A., and Deigaard, R. (1993). A boussinesq model for waves breaking in shallow water. *J. Coastal Engineering*, **20**, 185–202.

Skovgaard, O. and Petersen, M. H. (1977). Refraction of cnoidal waves. *J. Coastal Engineering*, **1**, 43–61.

Staub, C., Jonsson, I. G., and Svendsen, I. A. (1996). Sediment suspension in oscillatory flow: measurements of instantaneous concentration at high shear. *J. Coastal Engineering*, **27**, 69–76.

Stive, M. J. F. and Wind, H. G. (1982). A study of radiation stress and set-up in the nearshore region. *J. Coastal Engineering*, **6**, 1–25.

Svendsen, I. A. (1974). Cnoidal waves over a gently sloping bottom. Technical Report Ser. Pap., 6, Inst. Hydrodyn. Hydraul. Eng. (ISVA), Tech. Univ. Denmark, Lyngby.

Svendsen, I. A. (1984). Wave heights and set-up in a surf zone. *J. Coastal Engineering*, **8**, 303–329.

Svendsen, I. A. (1987). Analysis of surf zone turbulence. *J. Geophys. Res.*, **92**(c5), 5115–5124.

Svendsen, I. A. and Brink-Kjær, O. (1972). Shoaling of cnoidal waves. In *13th Coastal Engineering Conference*, pages 365–383, Vancouver. ASCE.

Svendsen, I. A. and Veeramony, J. (2001). Wave breaking in wave groups. *J. of Wtrwyy., Port, Coast. and Oc. Engng.*, **127**(4), 200–212.

Svendsen, I. A., Madsen, P. A., and Hansen, J. B. (1978). Wave characteristics in the surfzone. In *16th Coastal Engineering Conference*, pages 520–539, Hamburg. ASCE.

Svendsen, I. A., Schaffer, H. A., and Hansen, J. B. (1987). The interaction between the undertow and the boundary layer flow on a beach. *J. Geophys. Res.*, **92**(c11), 11845–11856.

Svendsen, I. A., Sancho, F. E., Oltman, J., and Thornton, E. B. (1997). Modelling nearshore circulation under field conditions. In *Waves' 97*, pages 765–776, Virginia Beach. ASCE.

Svendsen, I. A., Haas, K., and Zhao, Q. (2002). Quasi-3d nearshore circulation model shorecirc version 2.0. Technical report, Center for Applied Coastal Research, Univ. of Delaware.

Svendsen, I. A., Qin, W., and Ebersole, B. (2003). Modeling waves and currents at the lstf and other laboratory facilities. *J. Coastal Engineering*, **accepted**.

Ting, F. C. K. and Kirby, J. T. (1994). Observation of undertow and turbulence in a laboratory surf zone. *J. Coastal Engineering*, **24**, 51–80.

Trowbridge, J. and Madsen, O. S. (1987). Turbulent wave boundary layers, 1, model formulation and first-order solution. *J. Geophys. Res.*, **89**(c5), 7989–7997.

USACE (1984). Shore protection manual. Technical report, Washington.

Van Dongeren, A. R. and Svendsen, I. A. (2000). Nonlinear and 3-d effects in leaky infragravity waves. *J. Coastal Engineering*, **41**(4), 467–496.

Visser, P. J. (1984). A mathematical model of uniform longshore currents and comparison with laboratory data. Technical Report Communications on Hydraulics. Report 84-2, Department of Civil Engineering, Delft University of Technology.

You, Z.-J. (1994). A simple model for current velocity profiles in combined wave-current flows. *J. Coastal Engineering*, **23**, 289–304.

Zyserman, J. A. and Fredsøe, J. (1994). Data analysis of bed concentration of suspended sediment. *J. Hydraulic Eng.*, **120**(9), 1021–1042.